
Electron Pair Emission from NiO and Metal Surfaces

DISSERTATION

zur Erlangung des akademischen Grades
doctor rerum naturalium (Dr. rer. nat.)

MARTIN-LUTHER UNIVERSITÄT HALLE-WITTENBERG
NATURWISSENSCHAFTLICHEN FAKULTÄT II

angefertigt am

MAX-PLANCK-INSTITUT FÜR MIKROSTRUKTURPHYSIK

vorgelegt von

Frau Dipl.-Phys. Lucie BEHNKE

geb. am 12.02.1984 in Berlin

Gutachter:

1. Prof. Dr. Jürgen KIRSCHNER (Max-Planck-Institut für Mikrostruktur Physik)
2. Prof. Dr. Wolf WIDDRA (Martin-Luther-Universität Halle-Wittenberg)
3. Prof. Dr. Markus DONATH (Westfälische Wilhelms-Universität Münster)

Halle (Saale), 21.08.2014 (Tag der Verteidigung)

Contents

1	Introduction	7
2	Theoretical Background	11
2.1	Electron Scattering	11
2.1.1	Rutherford Scattering	11
2.1.2	Scattering from a Finite Square Well	13
2.1.3	Scattering from a Finite Radial Potential	14
2.1.4	Diffraction	17
2.1.5	Penetration into the Surface	19
2.2	Double Ionization of He	21
2.3	Manifestation of Electron Correlation	23
2.3.1	Exchange Hole	23
2.3.2	Screening	25
2.4	Description of Electron Correlation	27
2.4.1	Weakly Correlated System - Ag	27
2.4.2	Highly Correlated System - NiO	28
2.5	Double Photoemission ($\gamma, 2e$)	32
2.5.1	Double Photoemission (DPE) without Correlation	32
2.5.2	Double Photoemission (DPE) with Correlation	33
2.6	Double Electron Emission ($e, 2e$)	35
3	Experimental Background	39
3.1	Coincidence Demands	39
3.2	Experimental Set-up	44
3.3	Sample Preparation	48
4	Experimental Results	51
4.1	($e, 2e$) on Ag(100)	51
4.1.1	Energy Spectra	51
4.1.2	Absolute Pair Emission	58
4.1.3	Diffraction Effects	61
4.2	($e, 2e$) on NiO/Ag(100)	67
4.2.1	Energy Dependence	69
4.2.2	Thickness Dependence	74

4.2.3	Temperature Dependence	76
4.3	(e,2e) on Transition Metals	79
4.4	Pair vs. Single Electron Emission	83
5	Conclusions and Outlook	85
	Appendix	87
	Bibliography	91
	Publications	99

List of Abbreviations

(e,2e)	double electron emission
BZ	Brillouin zone
DFT	density functional theory
DOS	density of states
DPE	double photoemission
HDA	hemispherical deflection analyzer
IMPF	inelastic mean free path
LDA	local density approximation
LEED	low energy electron diffraction
MBE	molecular beam epitaxy
MCP	micro channel plate
MEED	medium energy electron diffraction
ML	mono layer
SNR	signal-to-noise-ratio
TMO	transition metal oxides
TOF	time-of-flight
UHV	ultra high vacuum
XC	exchange-correlation

1 Introduction

A solid crystal of one cubic centimeter contains more than 10^{23} atoms and therefore an immense number of electrons. The system has to be treated as a many particle problem, because the electrons interact. The interaction is divided mainly in two parts, Coulomb repulsion and exchange interaction, due to the Pauli principle. The interaction strength is labeled U .

So-called weak interacting systems can be described in an effective single particle picture. The value of U is approximately 0. This model is valid for many metals, for example Ag. Ag has a fully filled d shell and one valence s electron, making it a prototype metal. Ag is well studied.

However, this simple model fails, when the interaction of electrons become important due to localization of the electrons. This is the case for transition metal oxide (TMO). Due to the strong interaction of the electrons they are called highly correlated materials. A prototype for this class is the insulator NiO with partly filled d bands. NiO is studied extensively experimentally [1, 2, 3, 4, 5, 6, 7] and theoretically [8, 9, 10, 11, 12], but the electronic structure is still not fully understood. The simple effective potential approximation is not valid. The reason is the strong interaction between the electrons, which makes the calculation challenging and results in $U = 8 \text{ eV}$. The strong coupling of the electrons in NiO is also reflected in the anti-ferromagnetic ordering.

A direct way to probe the correlation is to measure the excitation of two electrons at the same time (in coincidence). A recent theoretical work from Napitu and Berakdar [13] predicts a direct relation between coincidence count rate and correlation strength U of the materials. Based on this work, a higher coincidence signal of NiO compared to Ag is expected.

Correlation spectroscopy, also known as coincidence spectroscopy, has a long tradition going back to 1924 when the first coincidence experiment was performed by Bothe and Geiger [14]. They bombarded X-ray photons in a hydrogen atmosphere and measured the backscattered Compton photon and the excited electron at the same time. They showed with this technique that energy and momentum conservation is valid for every single scattering process and not just for the statistical average of this process, as stated by Bohr, Kramers and Slater in the same year [15]. The experiment was a strong support for the wave-particle dualisms of light. The importance of the experiment is recognized by Bothe's Nobel prize. He concluded in his Nobel prize lecture that the coincidence technique will be an essential tool for modern nuclear physics.

Fifty years later the application of coincidence method is extended to atomic [16, 17, 18, 19], nuclear experiments [20, 21] and condensed matter physics [22, 23, 24, 25, 26, 27]. The studied systems are excited by photons, ions, positrons or electrons. This evolution was due to the experimental progress of the excitation sources and for surface science the progress in the ultra-high-vacuum (UHV) technique was important.

In 1992, Kirschner *et al.* [28] reported the first successful coincidence experiment on solids in backscattering geometry for primary electrons in the range between 18 and 100 eV to study the properties of the valence electrons. Coincidence events were detected from a W(100) surface with two channeltrons. The experiment could not resolve the energy of the incoming electron pairs.

The challenge in coincidence in general is that true and random coincidences are observed simultaneously. True coincidences are the result of one scattering process and random coincidences originate from different impact events. To increase the ratio between true and random coincidences the experiment requires low primary flux, which increases on the other hand the data acquisition time.

Later on, the experimental apparatus was improved by combining coincidence experiment with time-of-flight (TOF) technique to measure the energy and momentum of the electron pair emitted from W(100) surface [29]. The advantage of this set-up is its large acceptance angle. Energetically all electrons are detected, including energetically low secondary electrons. A drawback of this instrument is the energy dependent energy resolution, which is 1.5 eV for 20 eV electrons [30].

To achieve an energy resolution independent from the primary energy, the experimental set-up is equipped with a pair of energy dispersive elements (hemispherical analyzers). The energy resolution is for all energies 0.7 eV [31]. Hence, the primary electron energy can be varied over a wide range of energies. Another advantage of this set-up is, that the energy window of interests can be selected and low energy secondary electrons are suppressed [31, 32]. The hemispherical set-up allows to measure the integral coincidence events and also the energy distribution of the electron pairs.

In this thesis the hemispherical set-up is applied to measure and compare the correlation strength of different materials as NiO, Ag and Fe, Co, Ni, Pd. An important component of the experimental set-up is a primary electron flux meter to study the pair emission per incoming electron quantitatively.

This subject of the thesis is approached in the following steps:

- First, to understand the basic principles of the experiment, Ag as a simple system is investigated. The electron pair distribution in the dependence of the primary electron energy is studied systematically and compared with theoretical band structure calculations. Furthermore, the coincidence signal is connected to the crystal structure. Diffraction of electrons is considered. Low energy electron diffraction (LEED) is a well established technique to investigate crystal surfaces. In our experiment single electrons hit the surface, but electron pairs are detected instead of the elastically scattered electrons. Nonetheless, the electron pairs undergo diffraction. This was published in the case of Cu(100) crystal [31] and observed also for Ag(100), presented here.
- In the next section the results of NiO thin film are presented (evaporated on a Ag crystal). It is discovered, that the coincidence signal of NiO is around one order of magnitude enhanced compared to Ag. That is also true for CoO as another TMO example. The in-

creased signal yields to a reduced data acquisition time and enables to study systematically the correlation of NiO with respect to the primary energy, film thickness and temperature. The electron pair distribution is studied for a 15 ML thin film ($E_p = 22.6 - 68.6$ eV). To rule out, that the longer mean free path length of electrons in NiO compared to electrons in metals is responsible for the enhanced signal, the integral coincidence for film thicknesses from 2.4 to 15 ML is studied. Furthermore, the antiferromagnetic character of NiO is considered and the coincidence signal is investigated below and above Néel temperature for different film thicknesses.

- Besides Ag, the coincidence signal for other transition metals as Fe, Co, Cu and Pd were studied and the relation between coincidence intensity and electron screening is discussed.
- In the end, coincidence probability is compared to single emission probability taking into account all measured data.

This work is organized as following. Chapter 2 deals with the theoretical background. First, a short introduction to electron scattering is given. Then the interaction of electrons is approached by describing the double ionization of He. The manifestation of electron correlation is discussed shortly. As examples, the exchange hole and the electron screening are discussed. Electron correlation is described for so-called weakly correlated systems, like Ag and so-called highly correlated systems, like NiO. Shortly, the theory of double photoemission ($\gamma, 2e$) and double electron emission are introduced. In Chapter 3 the experimental background is presented, including the demands on a coincidence set-up, the experimental set-up and the sample preparation. The main results obtained during this work are summarized in Chapter 4. In Chapter 5 the conclusions and outlook are given.

2 Theoretical Background

2.1 Electron Scattering

2.1.1 Rutherford Scattering

This experiment is based on electrons backscattered from a solid surface. In view of the importance of scattering in this work, in the following section the principles of scattering in a microscopic picture is discussed.

An important contribution to the scattering theory was due to Rutherford and coworkers in 1911 [33]. They bombarded a thin gold foil with α particles (He^{2+}) to study the scattering cross section between α particles and atoms quantitatively. They expected, that all particles would homogeneously be scattered through the foil. The result was very surprising, because a few α particles were backscattered. Quantitatively, this could be explained by Rutherford's atomic model. To observe this remarkable deflection, the atoms must have a nuclei in the center with much heavier mass than the α particle. The nucleus has a positive charge Z_2e (Z is the atomic number).

The repulsive Coulomb force $|\mathbf{F}|$ acts around the positively charged nucleus and for the whole scattering path of the α particle (with charge Z_1e) it is

$$|\mathbf{F}| = \frac{1}{4\pi\epsilon_0} \frac{Z_1eZ_2e}{r^2}, \quad (2.1)$$

ϵ_0 is the vacuum permittivity and r is the distance between the two charge centers. The dependence of the scattering cross section on the scattering angle is calculated in two steps. Firstly, the deflection angle Θ of the scattered single α particle in dependence on the impact parameter b is determined. Secondly, because it is very difficult to follow the scattering path of one particle, it is averaged over all possible impact parameters. Multiple scattering events are not considered. Detailed steps are found in Ref. [34, 35].

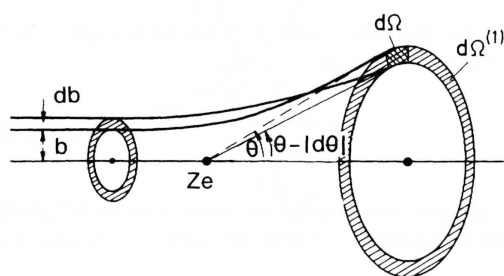


Figure 2.1 Incident particles with impact parameters in the range b to $b + db$ are deflected into the range of angles Θ to $\Theta - |d\Theta|$. The solid angle is Ω . Taken from Ref. [35].

The scattering path, the impact parameter b and the solid angle Ω are depicted in Fig. 2.1. This results in the classical Rutherford scattering formula to calculate the differential scattering cross section $\frac{d\sigma}{d\Omega}$ in dependence of the scattering angle ϕ

$$\frac{d\sigma}{d\Omega} = \left(\frac{1}{4\pi\epsilon_0} \frac{Z_1 Z_2 e^2}{4E_0} \right)^2 \frac{1}{\sin^4(\phi/2)}, \quad (2.2)$$

E_0 is the energy of the incident particle. Replacing the α particle by an electron results in the same scattering formula. In a classical picture it cannot be explained why a negative charged particle is backscattered from a positive charged nucleus. We have to leave the classical picture behind and discuss the electron as a wave in the quantum mechanic view.

The incoming electron wave traveling in z -direction is represented as a plane wave $\exp(ikz)$. The wave scatters with the (screened) Coulomb potential of the nucleus and the outgoing wave is described asymptotically as a spherical wave

$$\psi = f(\phi) \exp(ikr/r) + \exp(ikz). \quad (2.3)$$

The scattering angle is ϕ and $f(\phi)$ is the scattering amplitude. The traveling path of the electron particle and wave are schematically depicted in Fig. 2.2.

Solving the time independent Schrödinger equation with Coulomb potential

$$\mathcal{H}\psi(\mathbf{r}) = \left(\frac{-\hbar^2}{2m} \nabla^2 - \frac{1}{4\pi\epsilon_0} \frac{e^2}{r} \right) \psi(\mathbf{r}). \quad (2.4)$$

yields as well to the Rutherford scattering formula, Eq. (2.2). Due to the wave character of the electron, interference effects have to be taken into account.

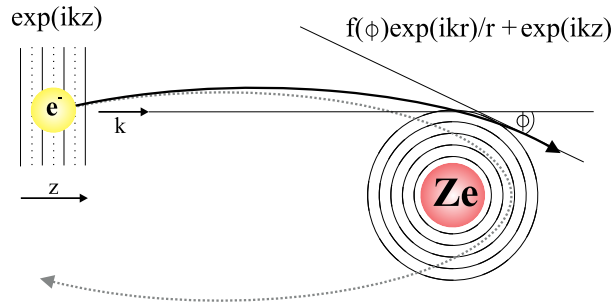


Figure 2.2 Sketch of an electron plane wave scattered at the (screened) Coulomb potential of the positive charged nucleus. The incoming wave is described as a plane wave and the scattered wave as a spherical wave.

Electrons are backscattered from the potential. To reveal this issue we introduce the scattering of a electron plane wave from a finite 1D square well.

2.1.2 Scattering from a Finite Square Well

The incoming electron plane wave is scattered from a potential $V_0 < 0$. The barriers of the potential $V(x)$ are defined as

$$V(x) = \begin{cases} V_0 & \text{for } |x| < a \\ 0 & \text{for } |x| > a, \end{cases} \quad (2.5)$$

Assuming the plane wave comes from the left, the solutions of the Schrödinger equation is described in the following form in the three regions

$$\Psi(x) = \begin{cases} I \exp(ikx) + R \exp(-ikx) & \text{for } x < -a \\ G \exp(iqx) + H \exp(-iqx) & \text{for } -a < x < +a \\ T \exp(ikx) & \text{for } +a < x, \end{cases} \quad (2.6)$$

where

$$k = \sqrt{\frac{2mE}{\hbar^2}} \quad \text{and} \quad q = \sqrt{\frac{2m(E + V_0)}{\hbar^2}}. \quad (2.7)$$

The incident wave $I \exp(ikx)$ is reflected $R \exp(-ikx)$ at the boundary of the potential $-a$. Inside the well ($-a < x < +a$) the waves travel with amplitude G and H . The part $T \exp(ikx)$ of the incoming wave is transmitted through the potential.

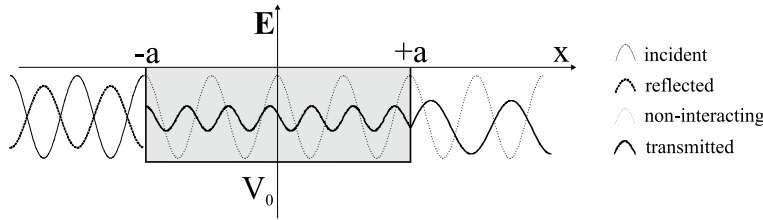


Figure 2.3 Sketch of a potential square well and plane wave solutions of the real part. The incident, reflected and transmitted wave are depicted. For comparison the non-interacting wave is shown as well.

The reflected amplitude matters in our experiment. The plane wave solutions are shown in Fig. 2.3. For comparison a non-interacting wave is shown as well. We see that the reflected wave undergoes a phase shift at the boundary. Furthermore, the electrons inside the potential is accelerated, as classically also expected. The wavelength is shorter and the amplitude is smaller. The Schrödinger equation is solved with the continuity conditions of the waves at the boundary and transmission $|T|^2$ and reflection $|R|^2$ probability are described as follows

$$|T|^2 = I^2 \frac{(q^2 - k^2)^2}{4k^2q^2 + \sin^2(2qa)(k^4 + q^4 - 2q^2k^2)} \quad (2.8)$$

$$|R|^2 = I^2 \frac{(q^2 - k^2)^2}{4k^2q^2 \cot^2(2qa) + (k^2 + q^2)^2}. \quad (2.9)$$

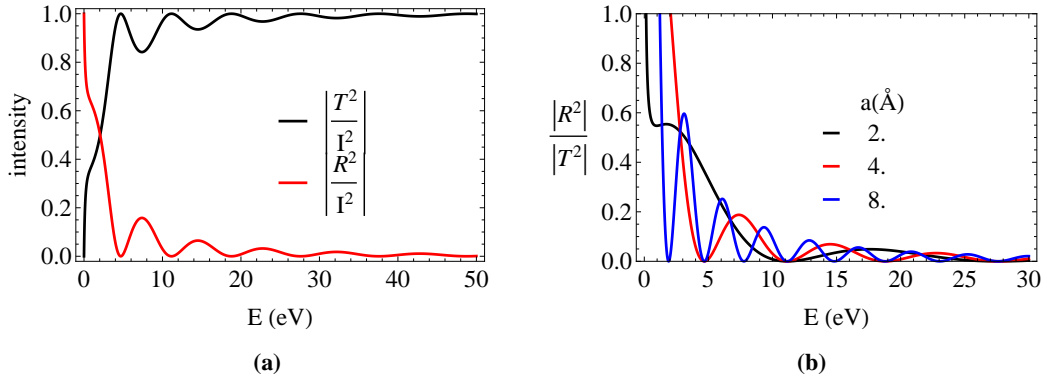


Figure 2.4 (a) Transmission probability $|T^2|/|I^2|$ (red) and the reflection probability $|R^2|/|I^2|$ (black) for lattice constant $a = 4 \text{ \AA}$ and inner potential $V_0 = -10 \text{ eV}$. (b) Ratio between reflection and transmission probability for different lattice constants $a = 2, 4, 8 \text{ \AA}$, coloured in black, red and blue, respectively.

Both quantities are normalized and plotted for the lattice constant $a = 4 \text{ \AA}$ of Ag in Fig. 2.4a. The probabilities oscillate due to constructive and destructive superposition of the waves. For energies below 2 eV the reflectance is higher than the transmission. For increasing energy the transmission dominates the reflectance. At the energy of 50 eV a high proportion of 90 % belongs to transmission and 10 % to reflectance.

To illustrate the dominance of reflection and transmission for each energy, we take the ratio

$$\frac{|R^2|}{|T^2|} = \left(\frac{(q^2 - k^2) \sin(2qa)}{2kq} \right)^2. \quad (2.10)$$

In Fig. 2.4b the ratio $|R^2|/|T^2|$ is plotted for different lattice constants $a = 2, 4, 8 \text{ \AA}$. The inner potential V_0 is kept at -10 eV . For all lattice constants the reflectivity is enhanced compared to the transmission up to 5 eV in this simple model. At low energies the ratio goes to infinity. As a result more electrons are backscattered for lower energies and the number of reflected electrons decreases with increasing energy. Based on this fact we have to operate our experiment at low primary energies. The number of oscillations are indirectly proportional to the lattice constant.

2.1.3 Scattering from a Finite Radial Potential

A more realistic situation to the scattering from a 1D square well is the scattering from a spherical potential with radius a . The boundaries of the considered potential are similar to the introduced one in Eq. (2.5).

Outside the potential, the free-space Schrödinger equation has to be solved in spherical coordinates without potential

$$-\frac{\hbar^2}{2m} \left(\frac{d^2 R(r)}{dr^2} + \frac{2}{r} \frac{dR(r)}{dr} \right) + \frac{l(l+1)}{2mr^2} R(r) = ER(r). \quad (2.11)$$

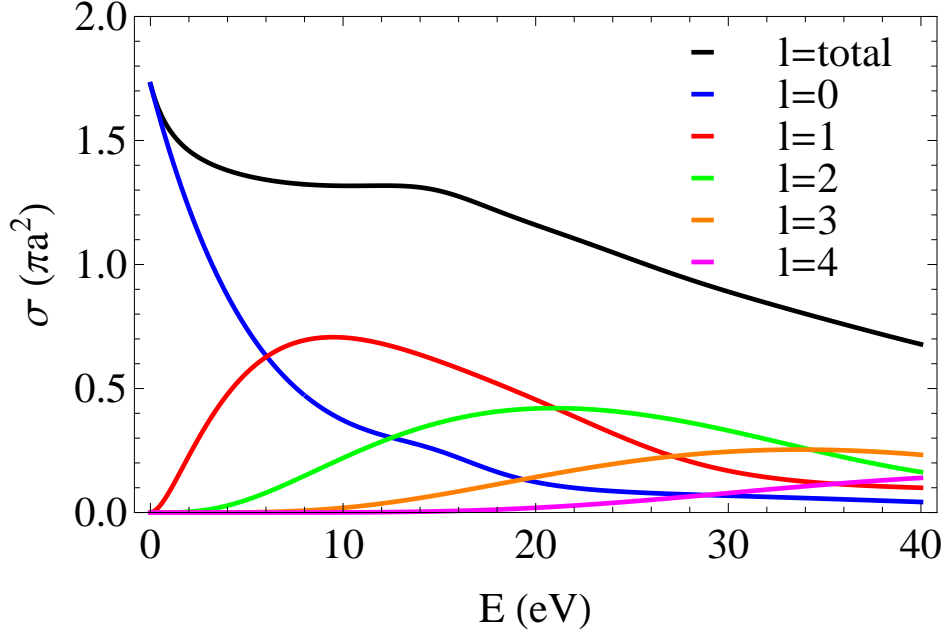


Figure 2.5 Scattering cross section σ as function of the primary energy E_p for a repulsive potential divided for the different partial waves from $l = 0$ to $l = 4$. The black line presents the total sum. The value of V_0 is 8 eV and the potential radius is $a = 2 \text{ \AA}$.

The radial solution $R_l(r)$ is a linear combination of Hankel functions $h_l^{(1)}$ and $h_l^{(2)}$ at distance r for which $V(r) = 0$.

$R_l(r)$ behaves as

$$R_l(r) = B_l \left(h_l^{(2)}(kr) + S_l(E) h_l^{(1)}(kr) \right). \quad (2.12)$$

The wave vector k is defined in Eq. (2.7). B_l and S_l are parameters. The Hankel functions are a combination of the Bessel function $j_l(kr)$ and Neumann function $n_l(kr)$, which do not represent the incoming and outgoing wave separately.

For this reason spherical Hankel functions are introduced

$$h_l^{(1)} = j_l(kr) + in_l(kr) \quad \rightarrow \frac{\exp(ikr)}{r}, \quad (2.13)$$

$$h_l^{(2)} = j_l(kr) - in_l(kr) \quad \rightarrow \frac{\exp(-ikr)}{r}. \quad (2.14)$$

The incoming plane wave is written in spherical harmonics with the Bessel function $j_l(kr)$ and the Legendre polynomial $P_l(\cos \theta)$. We assume the wave propagates in z - direction

$$\exp(i\mathbf{k} \cdot \mathbf{z}) = \frac{1}{kr} \sum_{l=0}^{\infty} i^l (2l+1) j_l(kr) P_l(\cos \theta). \quad (2.15)$$

The scattered spherical wave (Eq. (2.3)) outside the potential is written in asymptotic form as $j_l(kr) \rightarrow \sin(kr - l\pi/2)$

$$\psi_{\mathbf{k}}(\mathbf{x}) \rightarrow \frac{1}{kr} \sum_{l=0}^{\infty} i^l (2l+1) \exp(i\delta_l) \sin\left(kr - \frac{l\pi}{2} + \delta_l\right) P_l(\cos\theta). \quad (2.16)$$

The difference between the incident and scattered wave is expressed in the phase shift δ_l . Combining the standard scattering solution (Eq. (2.3)) with the incoming wave (Eq. (2.15)) and the scattered one (Eq. (2.16)) gives an equation for the scattering amplitude

$$f_k(\theta) = \frac{1}{k} \sum_{l=0}^{\infty} (2l+1) \exp(i\delta_l) \sin\delta_l P_l(\cos\theta). \quad (2.17)$$

The cross section σ is obtained by integrating over the whole solid angle Ω

$$\sigma = \int d\Omega \frac{d\sigma}{d\Omega} = \int d\Omega |f(\theta)|^2 = \sum_{l=0}^{\infty} \sigma_l \quad \text{with} \quad \sigma_l = \frac{4\pi}{k^2} (2l+1) \sin^2 \delta_l. \quad (2.18)$$

The scattering cross section σ depends on the phase shift δ_l , which depends on the scattering potential.

The phase shift δ_l for the repulsive potential V_0 has to be calculated. In our experiment the primary energy E_p is below 100 eV. Detailed calculations are found in Ref. [36, 37, 38]. In principle, the same strategy as for the 1D case (Sec. 2.1.2) is applied.

The phase shift δ_l is calculated

$$\tan(\delta_l) = \frac{kj'_l(ka)j_l(k_0a) - k_0j'_l(k_0a)j_l(ka)}{kn'_l(ka)j_l(k_0a) - k_0j'_l(k_0a)n_l(ka)}, \quad (2.19)$$

with

$$k = \sqrt{\frac{2mE_p}{\hbar^2}} \quad \text{and} \quad k_0 = \sqrt{\frac{2mV_0}{\hbar^2}}. \quad (2.20)$$

The scattering cross section σ for is calculated as function of E_p with fixed potential radius of $a = 2 \text{ \AA}$ and potential of $V_0 = 8 \text{ eV}$. The results for σ_l up to $l = 4$ are presented in Fig. 2.5. We see that higher orders of l can not be neglected and contribute to the σ_{total} .

In Fig. 2.6 the scattering cross section σ as function of the potential V_0 is shown. A measure for stronger electron-electron interaction is an increased potential hill. The elastic scattering process is a two body problem, so we transform the energy in center of mass coordinates. We assume that the scattering center is in rest, the scattering angle is 45° and both masses are equal. The energy of the incoming electron is 30 eV. This results in a reduced primary energy of $E_p = 15 \text{ eV}$. The radius has again a value of $a = 2 \text{ \AA}$.

The scattering cross section increases with increasing potential hill. The curve increases steeply up to the value when $E_p = V_0$ and then a constant value is reached.

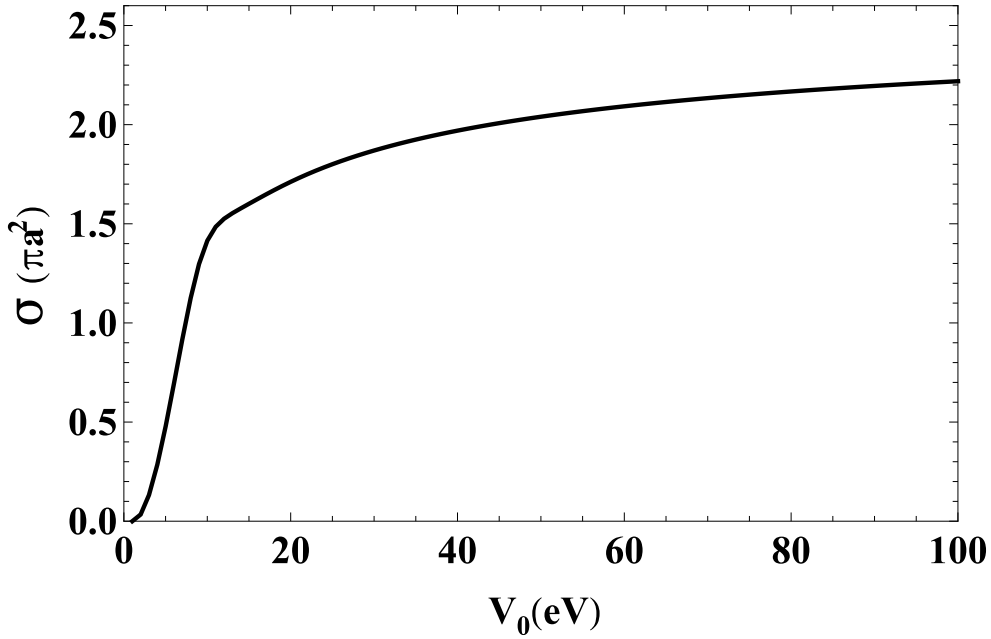


Figure 2.6 Scattering cross section σ as function of the primary energy V_0 for a repulsive potential. The value of E_p is 8 eV and the potential radius is $a = 2 \text{ \AA}$.

This simple model shows, that increasing electron-electron interaction (visualized by the increased potential hill V_0) results in higher scattering cross section.

As a result for two electron-electron scattering experiment, we conclude that higher intensity for stronger electron-electron interaction is expected.

2.1.4 Diffraction

In the experiment the incoming electron is not only scattered at one ion core, but at infinite periodic potentials in the crystal. In particular, low energetic electrons interact strongly with matter, described in detail in Ref. [39, 40, 41, 42].

The electrons are diffracted at the layers. This property is used in the low energy electron diffraction (LEED) experiment. Diffraction is sensitive to the exchange and correlation part of the electron potential. The intensity of the LEED beam is influenced by inelastic scattering with other electrons in the interior of the solid. Diffuse scattering is caused by the lattice motion and by surface roughness. To describe the scattering, two models are employed. First is the kinematic model, which assumes that the electrons are just once excited by the primary electron, furthermore the electrons move independently from each other. Second model is the so-called dynamical model, which is more sophisticated, because multiple scattering events are considered. Our focus is on the former model.

The kinematic model deals with single scattering, which means the electron is once elastically scattered by a surface atom without releasing energy to the system. The cross section of energetic low electrons is high, which results in a small penetration length and in multiple scattering events. The latter is ignored in this kinematic model. The momentum is transferred from the incoming electron k_p^{\parallel} to the scattered one.

Incoming wave Ψ_i is described by a plane wave

$$\Psi_i = \Psi_0 \exp(i\mathbf{k}_p \mathbf{r}). \quad (2.21)$$

The incoming wave penetrates inside the solid and is mostly scattered at the periodic ion cores of the lattice. This is the origin of the well known Bragg reflections. The periodicity of the diffracted lattice is parallel to the surface. The condition for interference is, that the difference of the incoming electron wave vector and the outgoing wave vector is a multiple of the reciprocal lattice vector ($\mathbf{k}_{\text{out} \parallel} - \mathbf{k}_0 \parallel = \mathbf{g}$).

Bragg's law is written also as

$$n\lambda = 2d \sin \Theta, \quad (2.22)$$

and is illustrated in Fig. 2.7.

In the kinematic theory the Bragg peaks are represented by a δ -function. With high temperatures the peaks are broaden due to interaction with phonons. The electrons are quasi-elastic scattered. Temperature influence on the diffraction will not be discussed.

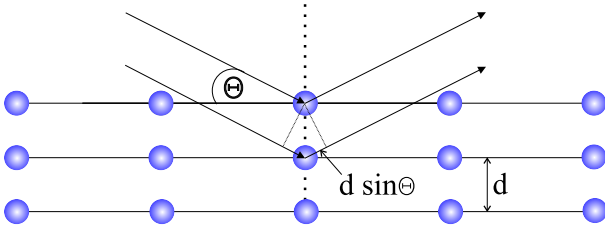


Figure 2.7 Schematic Bragg diffraction of the electron wave at the lattice planes.

Another effect is that the primary electrons gain energy by the inner potential V_0 and they are accelerated inside the solid. The inner potential is the energy from the vacuum level to the conduction band, the energy is around 10 eV. Whereas the work function is the energy from the valence level to the vacuum, which is for metals about 4 – 5 eV. The concept of the inner potential was first introduced by Bethe in 1928 [43] to dissolve the mismatch between theoretical and experimental LEED data. The inner potential is a kind of spatial average over the actual potential felt by the LEED electrons, including the region inside the atoms.

Absorption of electrons is very important in the LEED- IV measurement. When the electrons would not be absorbed, the Bragg-peak intensity would be infinite.

The LEED- IV curve is perfectly reproduced by the kinematic theory, if the unit cell is very large, hence the scattering at the ion core is weak. That is the case for crystals of inert gases.

To understand the scattering in three dimensions the band structure has to be considered. When two bands with the same \mathbf{k} -vector come close together in energy they interact strongly. Two states labeled Φ_1 and Φ_2 with the same \mathbf{k} -vector. They are coupled together by a matrix element $\langle \Phi_1 | V | \Phi_2 \rangle$ and they mix with amplitude

$$I \propto \frac{\langle \Phi_1 | V | \Phi_2 \rangle}{E_1 - E_2}. \quad (2.23)$$

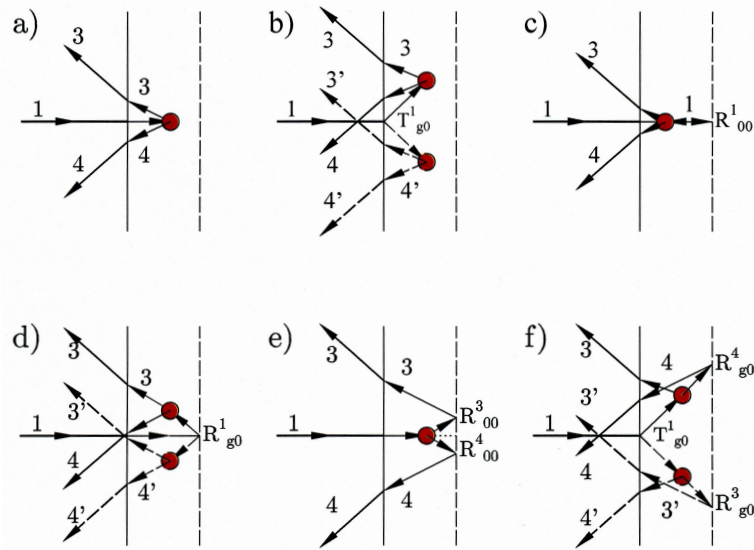


Figure 2.8 Possible scattering path for (e,2e) emission. The solid line represents the surface and the dashed line the first lattice plane. The filled circle symbolizes the collision with the valence electron. Taken from Ref. [44]. ©IOP Publishing. Reproduced by permission of IOP Publishing. All rights reserved.

and if E_1 is close to E_2 , strong mixing occurs. Strong reflectance is expected where the energies of the two Bloch waves are the same and they have similar k-vector, or they have the same k-vector and the energy values come close together. The band structure and the LEED intensities are related to each other. By comparing LEED-IV curve of the specular beam and the band structure (as done in Ref. [41] for Cu(100)), the peaks of the LEED-IV curve is identified with the critical points of the free electron like band structure (Γ -X direction). The incoming wave is totally reflected, when the energy corresponds to the band gap of the material.

Moreover, the final state of the photoemission process is described via the time reversed LEED-state. The final state is a superposition of the incoming electron and the reflected one.

Various possible scattering paths are possible when dealing with electron pairs. The paths of the primary electron interacting with the valence electron have to be considered and further the scattering paths of the outgoing pair. In Fig. 2.8 six pathways are shown. The incoming beam enters the surface (black thin line) perpendicular and interacts with the valence electron (filled circle). The pair can be directly reflected from the interaction center, the primary electron can be reflected at the lattice plane (dashed line) before interacting with the valence electron or the pair is reflected at the lattice plane. The (e,2e) experiment gives a hint, which path is more prominent, so that the calculations can be simplified.

2.1.5 Penetration into the Surface

An important quantity to consider in the scattering process is how long is the electron penetrate depth inside the solid and how long is the escape depth. This characterizes the surface sensitivity of the experiment. This subject is well explained in the literature Penn [45], Powell

[46], Powell and Jablonski [47], Werner [48]. The most common measure is the inelastic mean free path (IMFP), which is defined as the average distance that an electron with a given energy travels between successive inelastic collisions. Knowing this quantity is very important for the interpretation of the experimental data. The electrons are scattered inelastically by all charges in their path; nuclei and localized core electrons, valence electrons and conduction electrons. This yields to a decreased mean free path. The mean free path depends on the material and the primary energy of the incoming electron. However, an universal connection could be found by experiment between the primary electron energy and the IMFP. Summarized for different materials are the data points in the so-called “universal curve” (see Fig. 2.9).

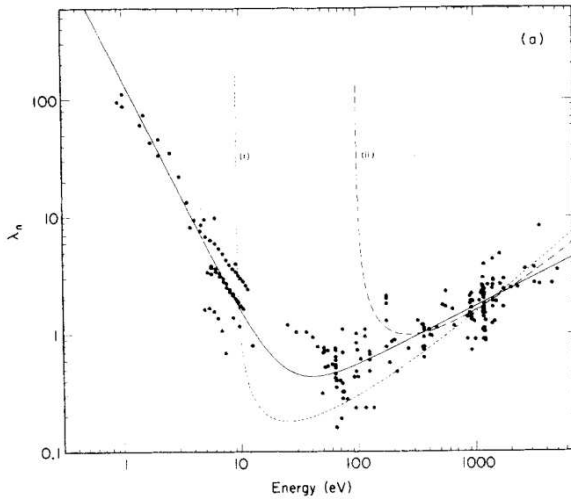


Figure 2.9 Inelastic mean free path (IMFP) measurements in nm for different primary energies and materials. The curve is called “universal curve”. Taken from Ref. [49].

In the energy range of the experiment (10 to 100 eV), the IMFP is in the minimum of the curve and around 1 nm. Meaning, the experiment is very surface sensitive. At lower energies the electron-electron scattering strongly decreases, which results in a longer mean free path. Large variations are seen, but it is good for estimating the IMFP. The IMFP is obtained with the overlayer method.

For increasing thickness d the substrate signal intensity I_0^S decreases as follows in dependence of the attenuation length Λ

$$I^S = I_0^S \exp(-d/\Lambda). \quad (2.24)$$

Similar the intensity of the overlayer I_L is given

$$I^L = I_0^L \exp(-d/\Lambda). \quad (2.25)$$

Exact knowledge of the film thickness and uniform layers on a flat substrate are required to obtain reliable data. Furthermore, one has to take into account that the IMFP varies with the underlying substrate [50]. It is difficult to compare several experimental results.

2.2 Double Ionization of He

The simplest two electron system is the He atom. By double ionization of the system two electrons are released [51, 52]. A closer look at the ionization energies gives an idea about the key role of the interaction of the two electrons.

To calculate the ionization energies, first we write down the Hamiltonian describing the system

$$\mathcal{H} = \mathcal{H}_1 + \mathcal{H}_2 + V_{e-e} \quad (2.26)$$

$$\mathcal{H}_{1,2} = \frac{\mathbf{p}_{1,2}^2}{2m} + \frac{Ze \cdot (-e)}{4\pi\epsilon_0 \cdot |\mathbf{r}_{1,2} - \mathbf{R}|} \quad (2.27)$$

$$V_{e-e} = \frac{(-e) \cdot (-e)}{4\pi\epsilon_0 \cdot |\mathbf{r}_1 - \mathbf{r}_2|}. \quad (2.28)$$

The terms $\mathcal{H}_{1,2}$ define the motion of a single electron with charge $(-e)$ around the nucleus of charge Ze localized at \mathbf{R} . The charge of the He nucleus is $Z = 2$. The coordinates of the electrons are given by $\mathbf{r}_{1,2}$. The electron-electron interaction is described by V_{e-e} . In the first approximation we neglect this term to calculate the ionization. The ionization energy of the H atom is $E_n = 13.6 \text{ eV} \cdot \frac{Z^2}{n^2}$, where n is an integer number. To double ionize He two electrons are released. Consequently, an energy of 108.8 eV would be needed to excite both electrons. Experimentally this value could not be confirmed, because we neglected the electron-electron interaction. Instead, a value of 79 eV was measured [53], which is a large discrepancy to 108.8 eV. Additionally ignoring the electron-electron interaction and setting $V_{e-e} = 0$ could not explain how one photon could cause the emission of an electron pair, when they are considered as independent of each other. A finite electron-electron interaction has to be taken into account. Rewriting V_{e-e} gives

$$V_{e-e} = \frac{e^2}{4\pi\epsilon_0 \cdot |\mathbf{r}_1 - \mathbf{r}_2|} = \frac{1}{2} \cdot \frac{e^2}{4\pi\epsilon_0 \cdot |\mathbf{r}_1 - \mathbf{r}_2|} + \frac{1}{2} \cdot \frac{e^2}{4\pi\epsilon_0 \cdot |\mathbf{r}_2 - \mathbf{r}_1|}. \quad (2.29)$$

This equation is approximated by the fact, that the 1s electron is located in the vicinity of the nucleus. When we look at electron 1, electron 2 appears to be at the nucleus and the other way round. That is why we can rewrite the distance between the electrons as follows: $|\mathbf{r}_1 - \mathbf{r}_2| \approx |\mathbf{r}_1 - \mathbf{R}|$ and $|\mathbf{r}_2 - \mathbf{r}_1| \approx |\mathbf{r}_2 - \mathbf{R}|$. Inserting the approximation in Eq. (2.29) results in

$$V_{e-e} = \frac{1}{2} \cdot \frac{e^2}{4\pi\epsilon_0 \cdot |\mathbf{r}_1 - \mathbf{R}|} + \frac{1}{2} \cdot \frac{e^2}{4\pi\epsilon_0 \cdot |\mathbf{r}_2 - \mathbf{R}|}. \quad (2.30)$$

Comparing now the coordinate dependences of $\mathcal{H}_{1,2}$ in Eq. (2.28) with the last equation, we recognize the same dependence as the nucleus-electron interaction. Hence the Hamiltonian is changed to

$$\begin{aligned} \mathcal{H} &\approx \widehat{\mathcal{H}}_1 + \widehat{\mathcal{H}}_2, \\ \widehat{\mathcal{H}}_{1,2} &= \frac{\mathbf{p}_{1,2}^2}{2m} + \frac{(-e^2) \cdot (Z - 1/2)}{4\pi\epsilon_0 \cdot |\mathbf{r}_{1,2} - \mathbf{R}|}. \end{aligned}$$

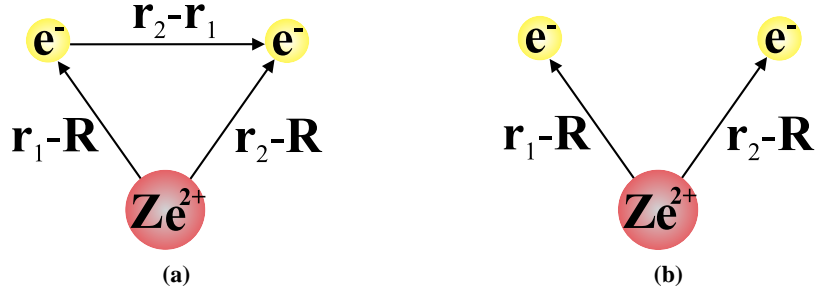


Figure 2.10 (a) He atom with attractive Coulomb interaction between nucleus - electrons and repulsive Coulomb interaction between electron-electron $V_{e,e}$. (b) Approximative picture. The charge of the nucleus is reduced and the interaction between the electrons is canceled. Taken from Ref. [52].

The Hamiltonian $\widehat{\mathcal{H}}_{1,2}$ describes an electronic system where the two electrons feel a reduced charge of the nucleus $(Z - 1/2)e = \widehat{Z}e$. Furthermore, the electrons do not interact directly with each other, instead the interaction V_{e-e} is incorporated in the approximation. The geometric configurations are shown in Fig. 2.10; (a) without approximation and (b) with approximation. The reduced charge of the nucleus is interpreted as screening. The charge $\widehat{Z}e$ is handled as a parameter $\widehat{Z} = Z - S$ with the screening parameter S which is varied. The ionization is treated in two steps. First the single ionization, where the screening has to be considered and second the release of the remaining electron without screening. This can be written as $\widehat{E}_n = 13.6 \text{ eV} \cdot \left(\frac{(Z-S)^2}{n^2} + \frac{Z^2}{n^2} \right)$. To obtain the experimental value of around 79 eV the best fit is a screening parameter $S = 0.656$. Also for the single ionization the basic approximation of the electron-electron interaction gives a reasonable result; experiment measures a value of around 24.6 eV and our theory predicts a similar one.

This simple example reveals the importance of considering the interaction between the electrons. This is the basis of the correlation experiments. The first electron pairs from He in coincidence in a so-called double photoemission (DPE) experiment were observed by Schwarzkopf *et al.* [54].

2.3 Manifestation of Electron Correlation

The electron interaction is divided into an exchange and a correlation part. Exchange interaction for fermions is also called Pauli principle. Electrons with the same spin orientation avoid to be at the same position.

2.3.1 Exchange Hole

A consequence of Coulomb interaction and Pauli-exclusion principle is that each electron creates a depletion, or hole, of electron density around itself as a direct consequence of exchange-correlation effects. The so-called exchange-correlation (XC) hole is formed. Described by Wigner and Seitz [55] and Slater [56] in the 1930s. In this section the distribution of the hole considering only the exchange part is calculated.

The antisymmetric electron pair wave function for free electrons is written as

$$\Psi_{ij} = \frac{1}{\sqrt{2}V} (\exp(i\mathbf{k}_i\mathbf{r}_i) \exp(i\mathbf{k}_j\mathbf{r}_j) - \exp(i\mathbf{k}_i\mathbf{r}_j) \exp(i\mathbf{k}_j\mathbf{r}_i)) . \quad (2.31)$$

The wave function has to be multiplied by its conjugate complex to calculate the probability density. The probability to find one electron at \mathbf{r}_i while the other is at $d\mathbf{r}_j$ is

$$\begin{aligned} |\Psi_{ij}|^2 d\mathbf{r}_i d\mathbf{r}_j &= \frac{1}{2V^2} (2 - (\exp(i(\mathbf{k}_i - \mathbf{k}_j)(\mathbf{r}_i - \mathbf{r}_j)) + \exp((-i(\mathbf{k}_i - \mathbf{k}_j)(\mathbf{r}_i - \mathbf{r}_j)))) d\mathbf{r}_i d\mathbf{r}_j \\ &= \frac{1}{V^2} (1 - \cos(\mathbf{k}_i - \mathbf{k}_j)(\mathbf{r}_i - \mathbf{r}_j)) d\mathbf{r}_i d\mathbf{r}_j . \end{aligned} \quad (2.32)$$

The probability to find two identical electrons at the same place ($\mathbf{r}_i = \mathbf{r}_j$) is zero with arbitrary $\mathbf{k}_i, \mathbf{k}_j$, which is in accordance to the Pauli principle. The electron density ρ is calculated around a fixed electron i where $\mathbf{r}_i = 0$. The electron concentration n is reduced by a factor of 2 because of the two spin orientations.

The average electron density as a result of exchange around the Fermi sphere is

$$\rho_{ex}(\mathbf{r}) = \frac{en}{2} \overline{(1 - \cos((\mathbf{k}_i - \mathbf{k}_j) \cdot \mathbf{r}))}, \quad \text{with } n_{\uparrow} = n/2. \quad (2.33)$$

The next step is to integrate $\rho_{ex}(\mathbf{r})$ over the hole Fermi sphere from the Fermi vector k_F to 0

$$\rho_{ex}(\mathbf{r}) = \frac{en}{2} \left(1 - \frac{1}{\left(\frac{4\pi k_F^3}{3}\right)^2} \int_0^{k_F} \exp(i\mathbf{k}_i\mathbf{r}) d\mathbf{k}_i \int_0^{k_F} \exp(i\mathbf{k}_j\mathbf{r}) d\mathbf{k}_j \right) . \quad (2.34)$$

The equation is integrated in spherical coordinates, so $d\mathbf{k}_i = 4\pi k^2$. Transforming the vector product $\mathbf{k}_i \cdot \mathbf{r} = kr \cos(\vartheta)$ and integrating the exponential function over $\cos(\vartheta)$.

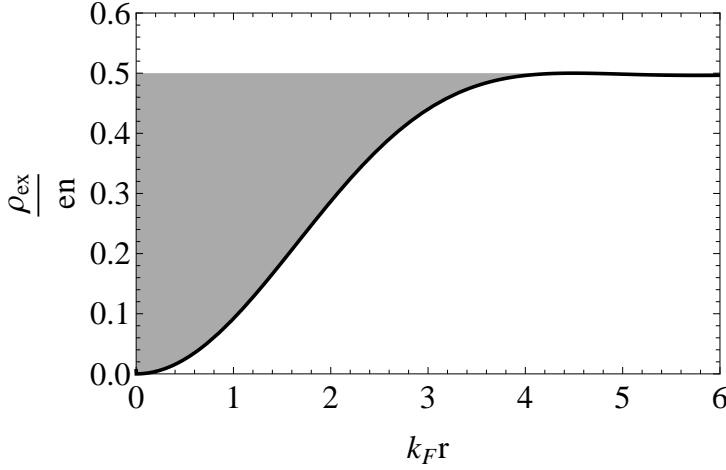


Figure 2.11 The calculated exchange hole is symbolised by the grey area. The normalized density ρ_{ex}/ne is shown in dependence of $k_F r$.

Equation (2.34) is converted into

$$\begin{aligned} \rho_{ex}(\mathbf{r}) &= \frac{en}{2} \left(1 - \frac{1}{\left(\frac{4\pi k_F^3}{3}\right)^2} \left(\int_0^{k_F} k^2 \frac{\sin(kr)}{kr} dk \right)^2 \right) \\ &= \frac{en}{2} \left(1 - 9 \frac{(\sin k_F r - k_F r \cos k_F r)^2}{(k_F r)^6} \right). \end{aligned} \quad (2.35)$$

In Fig. 2.11 is plotted Eq. (2.35). The grey area symbolizes reduced density. This area is interpreted as the exchange hole. The product of $k_F r$ is constant, so the radius of the exchange hole gets smaller by increasing the electron concentration n .

The number of charges q inside the exchange hole is calculated by integrating Eq. (2.35) over the whole space in spherical coordinates ($4\pi r^2 dr = dr$). We replace the electron density by $n = \frac{k_F^3}{3\pi^2}$ and substitute $k_F r = x$ in Eq. (2.35)

$$\begin{aligned} q &= \int_0^\infty \rho(\mathbf{r}) = \frac{6e}{\pi} \int_0^\infty \frac{(\sin x - x \cos x)^2}{x^4} dx \\ &= \frac{6e}{\pi} \left(\underbrace{\frac{(1+x^2)\cos(2x)}{6x^3}}_{\lim_{x \rightarrow \infty} = 0} + \underbrace{\frac{\sin(2x)}{3x^2}}_{\lim_{x \rightarrow \infty} = 0} + \underbrace{\frac{-1 - 3x^2 + 2x^3 \text{SinIntegral}(2x)}{6x^3}}_{\lim_{x \rightarrow \infty} = \frac{\pi}{6}} \right) \\ &= 1. \end{aligned} \quad (2.36)$$

We can conclude that the exchange hole contains one elementary charge.

For the sake of completeness the Coulomb interaction has to be considered as well. Resulting in the exchange correlation (XC) hole. For the first time the XC hole was observed experimentally for LiF(100) by using TOF coincidence set-up [57]. In Fig. 2.12 the intensity is plotted versus the surface momentum components k_x and k_y . One can observe a reduced intensity around the central coordinates. The black circle in the middle represents the detector.

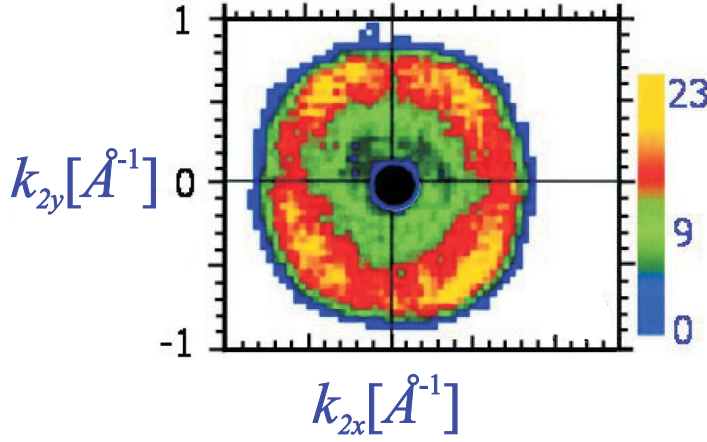


Figure 2.12 Measured exchange correlation hole for LiF(100) with time-of-flight coincidence set-up ($E_p = 30.7$ eV). Intensity is in arbitrary units. The black circle represents the detector position. Taken from Ref. [57]. Copyright (2005) by the American Physical Society.

2.3.2 Screening

Another way of describing the interaction of the electron cloud with an external field is screening. The electrons in the electron gas interact with each other because of the Coulomb potential. This potential screens the electrons in a short-range and creates a hole around each electron. In metals this phenomena is especially pronounced. The screening is described with an exponential screened Coulomb potential. The screening length is approximated with the Thomas-Fermi model for a free electron gas. The Thomas-Fermi-screening length is labeled as λ_{TF} and the screening strength as q_{TF} [58].

They are related as follows

$$\lambda_{TF} = \frac{1}{q_{TF}} = \left(\frac{\epsilon_0}{e^2 D(E_F)} \right)^{1/2}. \quad (2.37)$$

For an electron gas with isotropic distribution the density of states $D(E_F)$ at the Fermi energy is

$$D(E_F) = \frac{3}{2} \frac{n}{E_F} = \frac{3}{2} \frac{n \cdot 2m}{\hbar^2 k_F^2}. \quad (2.38)$$

When we combine Eq. (2.37) and Eq. (2.38) and set the Fermi wave vector to $k_F = (3\pi^2 n)^{1/3}$, we find the screening length as

$$\lambda_{TF}^2 = \frac{a_0 \pi}{4k_F}, \quad (2.39)$$

One way to include the interaction of the electrons is given by the Thomas-Fermi theory, which derives the electron-electron interaction as follows

$$U(r_{12}) = \frac{Ze}{4\pi\epsilon_0} \frac{\exp(-r_{12}/\lambda_{TF})}{r_{12}}. \quad (2.40)$$

The theory includes the screening length λ_{TF} or the screening strength $1/q_{TF}$. The Thomas-Fermi potential (Eq. (2.40)) is plotted for screening strength $q_{TF} = 0 - 10 \text{ \AA}^{-1}$ in Fig. 2.13.

The unscreened potential is the Coulomb potential. In the case $q_{\text{TF}} = 10 \text{ \AA}^{-1}$, the electron potential is extended only to a distance up to 0.5 \AA . In contrast, the unscreened potential ($q_{\text{TF}} = 0$) approaches very slowly the energy 0 eV . Only at a distance of 20 \AA the influence of the potential is negligible. In other words, the Coulomb correlation is maximal for the unscreened Coulomb interaction and decreases with increasing screening.

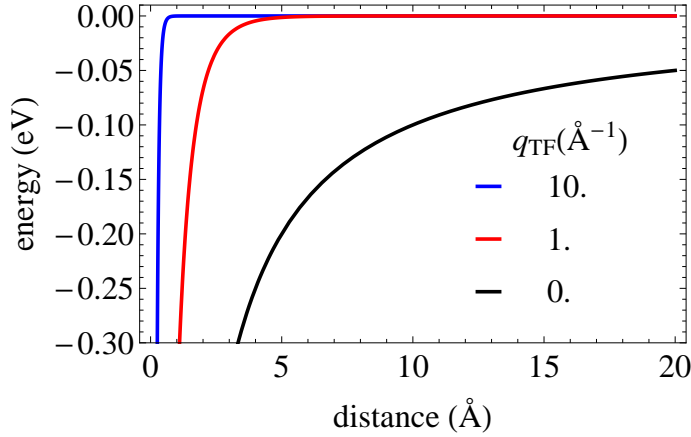


Figure 2.13 Screened potentials for screening strength q_{TF} from 0 to 10 \AA^{-1} .

A scalar ‘‘Coulomb correlation factor’’ f^C is defined by Gollisch *et al.* [59] to describe the two electron potential interaction. In the absence of the Coulomb correlation, f^C is a constant (equal to 1). In [60] the coincidence intensity in dependence of the screening parameter q_{TF} is calculated and presented in Fig. 2.14. We see, that with decreasing screening length the coincidence signal increases. Additionally, the dependence of the total ionization cross-section on the primary energy E_p for different screening length was studied by [61] for a metal cluster. They found a decisive effect of the screening length λ_{TF} of the electron-electron interaction and that the ionization cross section increases monotonically for lower energies.

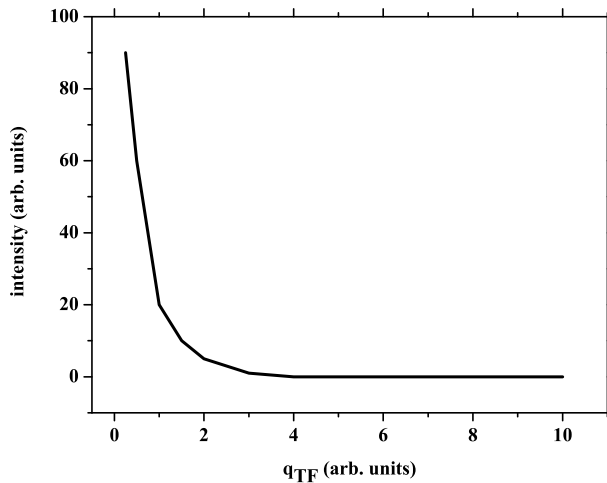


Figure 2.14 Coincidence intensity in dependence of the screening strength q . Smaller screening strength gives larger coincidence signal. Smaller screening strength is a result of stronger electron-electron interaction. Taken from Ref. [60].

2.4 Description of Electron Correlation

2.4.1 Weakly Correlated System - Ag

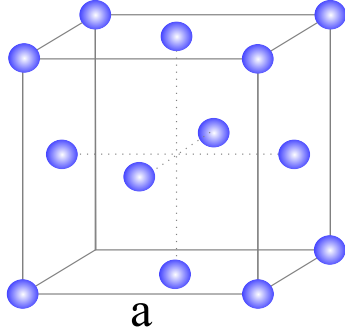


Figure 2.15 Spherical model of a Ag crystal. Ag forms a face center cubic crystal with lattice constant of $a = 4.09 \text{ \AA}$.

First electronic systems with weak electron interaction are discussed. A weakly correlated system can be described within the local density approximation (LDA). The approximation uses an exchange-correlation functional in density functional theory (DFT), introduced by Kohn and Sham [62]. The basic idea of Kohn-Sham DFT is to replace the calculation of the full many-body wave function with non-interacting electrons moving in an effective potential. LDA depends only on the electronic density of each point in space. The electron interaction is described within an effective potential, so that the system is reduced to a single particle problem. LDA gives extremely good results for homogeneous electron gas. One approach is the Thomas-Fermi model with the Thomas-Fermi density of states $D(E)$ (Eq. (2.38)). In LDA the XC energy in each spatial point serves as XC energy per particle $\epsilon_{XC}^{\text{hom}}(\rho(\mathbf{r}))$ from a uniform electron gas with density $\rho(\mathbf{r})$.

The exchange correlation energy E_{XC}^{LDA} contains all information about the many-body problem and is written in LDA as

$$E_{XC}^{\text{LDA}}(\rho(\mathbf{r})) = \int \rho(\mathbf{r}) \epsilon_{XC}^{\text{hom}}(\rho(\mathbf{r})) d(\mathbf{r}). \quad (2.41)$$

Properties of metals, like Ag with s^1 valence electron can be described surprisingly well with LDA. The validity of the approximation is tested by calculating physical properties and comparing them with experimental results.

One property is for example the lattice constant a . Ag crystallizes in a face center cubic lattice (Fig. 2.15). LDA calculations gives $a_{\text{LDA}} = 4.12 \text{ \AA}$ [63], which is in good agreement with the experimental value $a_{\text{exp}} = 4.09 \text{ \AA}$ [64]. The nature is quiet well resembled. In addition, the band structure is reproduced within LDA. These results reveal that Ag electrons interact weakly.

Table 2.1 Theoretical and experimental lattice constants a of Ag and NiO.

	LDA	LDA + U $U = 8 \text{ eV}$	Exp.
$a_{\text{Ag}} (\text{\AA})$	4.12 [63]		4.09 [64]
$a_{\text{NiO}} (\text{\AA})$	4.08 [12]	4.19 [10]	4.17 [64]

Table 2.2 Theoretical and experimental band gap E_{gap} and magnetic moment μ_B of NiO [65].

	LDA	LDA + U $U = 8 \text{ eV}$	Exp.
$E_{\text{gap}} (\text{eV})$	0.1	4.1	4.3 [9]
μ_B	0.95	1.73	1.9 [66]

2.4.2 Highly Correlated System - NiO

LDA is not applicable for strong interacting systems with localized electrons like the TMO NiO. Experimentally, a lattice constant of $a_{\text{NiO}}^{\text{exp}} = 4.17 \text{ \AA}$ [64] is measured for the rock salt structured NiO, but LDA underestimates the lattice constant as $a_{\text{NiO}}^{\text{LDA}} = 4.08 \text{ \AA}$ [12]. The discrepancy between experiment and LDA calculations for NiO is large, compared to Ag (Tab. 2.1). Apparently, correlation cannot be neglected for NiO. The lattice constant a is reproduced only by adding a correlation parameter U . The meaning of the U is discussed.

An important property of such materials is the band gap E_{gap} . LDA predicted TMO's like NiO to be metals within LDA. The d bands are partly filled, hence NiO is expected to be a metal in the classically picture. However, insulating behavior is observed experimentally. In Tab. 2.2 the experimental [9] and calculated values ($U = 0, 8 \text{ eV}$) for E_{gap} [65] are presented. Increasing correlation parameter U splits up the band. The first time in 1937 it was shown by Mott and Peierls [67] that the interaction of the electrons has to be taken into account to describe the insulating behavior.

The strong interaction of electrons in NiO results also in antiferromagnetic ordering. The planes alternate in (111) plane; indicated by yellow and blue planes in Fig. 2.16a. The Neél temperature T_N of bulk NiO is 523 K. It is interesting to calculate the magnetic moment μ_B within LDA and compare it with the experiment. The calculated value $\mu_B^{\text{LDA}} = 0.9$ [65] is half of the experimentally obtained one $\mu_B^{\text{exp}} = 1.9$ [66]. Here again a correlation parameter U must be included to be consistent with the experiment. The values are found in Tab. 2.2.

To describe highly correlated systems theoretically, the simplest model is the Hubbard Hamiltonian

$$\hat{H} = \sum_{ij,\sigma} t_{ij} c_{i\sigma} c_{j\sigma}^\dagger + U \sum_i n_{i\uparrow} n_{i\downarrow}. \quad (2.42)$$

Electrons with spin σ up and down move between adjacent lattice sites i, j . The electrons interact when they are at the same lattice site due to the Pauli principle, which requires that they have opposite spin. The first term describes the kinetic energy of the electrons to hop from one lattice site to the other by the matrix element t_{ij} . The creation of an electron on site i with spin σ is defined by $c_{i\sigma}^\dagger$ and the annihilation of an electron represents by $c_{i\sigma}$. The second term presents the energy penalty the electrons have to pay when they occupy the same lattice site. U is the local Coulomb repulsion and $n_{i\sigma} = c_{i\sigma}^\dagger c_{i\sigma}$ is the number operator. Figure 2.17 illustrates the

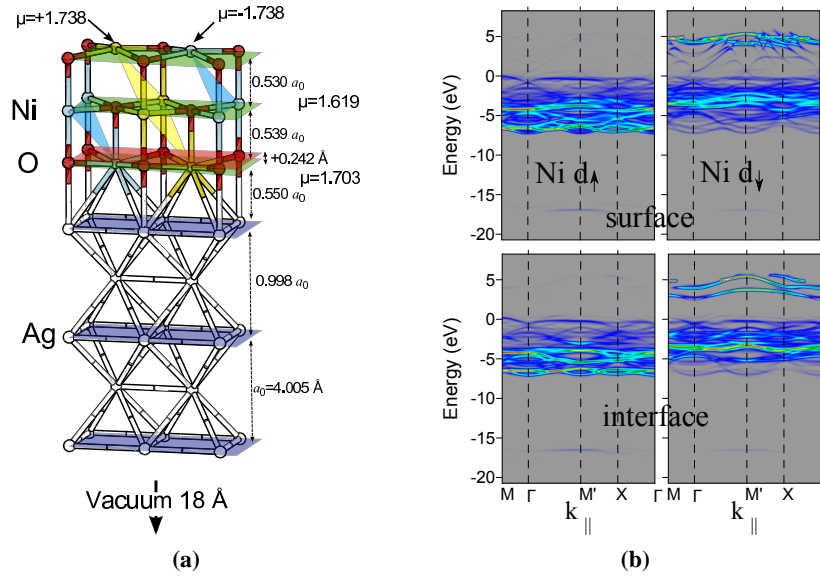


Figure 2.16 (a) Results of the structural optimization and magnetic properties for the anti-ferromagnetic configuration of 3 ML NiO on Ag(100). (b) Spin-resolved band structure projected onto the d-states of surface and interface Ni atoms. The parameter used are $U = 8 \text{ eV}$ and $J = 0.95 \text{ eV}$. Taken from Ref. [68].

lattice and the electron movement.

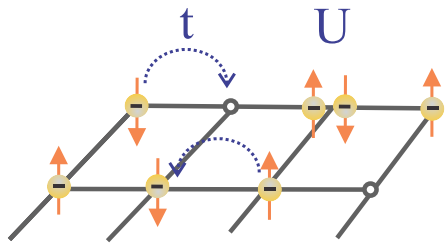


Figure 2.17 Sketch of the Hubbard model. The t indicates the hopping and the U the energy the electron has to pay to change the lattice site.

The two parameters t and U compete with each other. The kinetic part t tends the electrons to move freely from one site to an other and the Coulomb repulsion U , is minimal when the electrons are located on their lattice sites. The competition is expressed in the ratio U/W . W is called bandwidth and is a parameter for the hopping t . For small ratio, the Coulomb repulsion is weak and the electrons can move easily. If the ratio is big, the Coulomb repulsion is strong and the electrons are captured on one lattice site.

The behavior of the DOS by changing the ratio U/W from 0 to 2 is schematically shown in Fig. 2.18. In the case $U = 0$ the DOS forms a hill around the Fermi energy E_F (Fig. 2.18a). By increasing $U/W = 0.5$ the width of the hill gets smaller and foothills are formed (Fig. 2.18b). By further increasing U/W to 1.2 the width of the main hill gets smaller and two side hills appear (Fig. 2.18c). They are still connected to the peak at E_F . Further increase of the ratio results in disappearance of the peak at E_F and the side hills gets separated by U . An insulator is formed. The bands are called the lower and upper Hubbard band (LHB and UHB), respectively. One example of this insulator are transition metal oxides (TMO) like NiO or CoO.

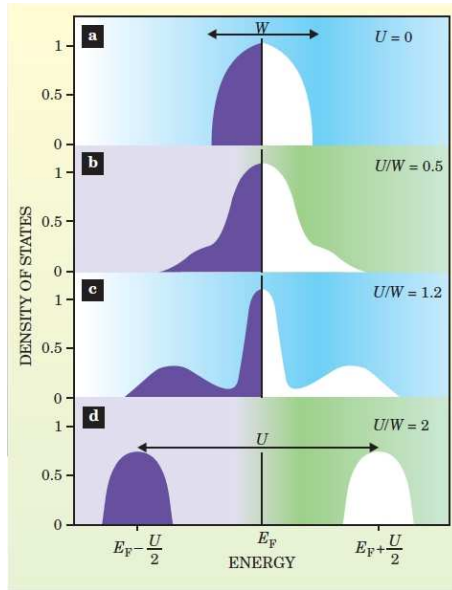


Figure 2.18 Illustration of the density of states (DOS) for different U/W ratios. In (a) ($U = 0$) the DOS forms a hill around the Fermi energy E_F . In (b) the ratio is $U/W = 0.5$ and the width of the hill gets smaller, in exchange foothills are formed. With increasing U/W ratio to 1.2 (c) the width of the main hill gets smaller and two side hills appear. They are still connected to the main one. Further increase of the ratio U/W to 2 (d) results in disappearance of the main peak and in separation of the side hills by U . Taken with permission from [69]. Copyright (2004), AIP Publishing LLC.

Two classes of this insulators are distinguished: Charge-transfer-insulator and Mott-Hubbard-insulator, sketched in Fig. 2.19a. In the first case the electrons move between atoms within the unit cell. In NiO the electrons would be transferred from one Ni atom to the other through O needing charge-transfer energy Δ . This energy is smaller than the Coulomb energy U , separating LHB and UHB. For Mott-Hubbard-insulator the situation is the other way round; the Coulomb energy U is larger than the transfer energy Δ .

Zaanen, Sawatzky, and Allen [70] classified various transition-metal compounds in a $U - \Delta$ diagram (Fig. 2.20). They classified NiO as charge-transfer insulator with $U \approx 8$ eV and $\Delta \approx 4$ eV. Scanning tunneling microscope (STM) experiment supports the description of NiO as charge transfer insulator [71].

However, in the literature NiO is also considered as a Mott-Hubbard-insulator [8]. In reality the electronic structure is a mixture of both characters. It was long time a challenge to calculate the band structure of NiO, because besides correlation effects, also the hybridization between the transition metal d states and the O p states need to be considered.

Recently, the band structure was calculated with combination of an *ab initio* band structure method and the dynamical mean-field theory [72]. Before the band structure was calculated with LDA+ U theory by Anisimov *et al.* [73]. With this method it was possible to reproduce the splitting between the d band. But the drawback was that most d electrons were found in the lower d band. Which is against the experimental observation in the photoemission data [3]. A step further in theoretical understanding of NiO was based on exact diagonalization studies. It gave strong evidence that dynamical correlation has to be included, done by Fujimori *et al.* [74]. This approach is based on so-called atomic multiplet theory and the Coulomb interaction in the 3d shell surrounded by the oxygen nearest neighbors (octahedral clusters) is calculated exactly. The band structure for the LDA+ U calculations is presented in Fig. 2.16b; values of the Hubbard parameters $U = 8$ eV and $J = 0.95$ eV are used as suggested by Anisimov and Aryasetiawan

[75]. J is the exchange parameter. This is not a unique choice. A number of recent works address the problem of *ab initio* determination of these parameters. A detailed discussion on the relevant physical properties of transition metal oxides as a function of these parameters are found in a recent work [76].

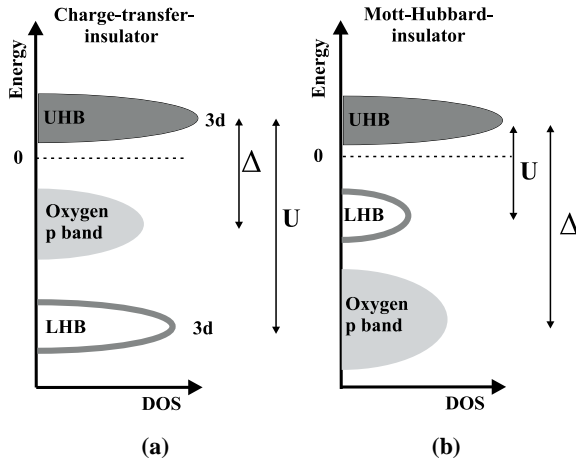


Figure 2.19 Schematic density of states (DOS) of (a) charge-transfer-insulator ($U > \Delta$) and (b) Mott-Hubbard-insulator ($U < \Delta$). LHB and UHB means lower and upper Hubbard band, respectively. U is the Coulomb energy and Δ is the charge-transfer energy.

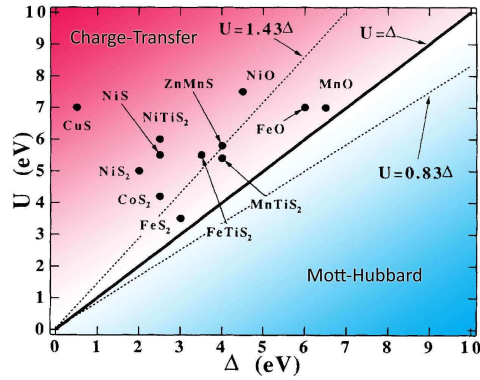


Figure 2.20 Zaanen-Sawatsky-Allen diagram to classify charge-transfer and Mott-Hubbard insulators. Taken from Ref. [70].

We conclude that electron interaction is an important part to calculate the electronic structure of NiO. Since NiO is a strongly correlated system, one cannot reproduce experimental results based on simple approximation.

2.5 Double Photoemission ($\gamma, 2e$)

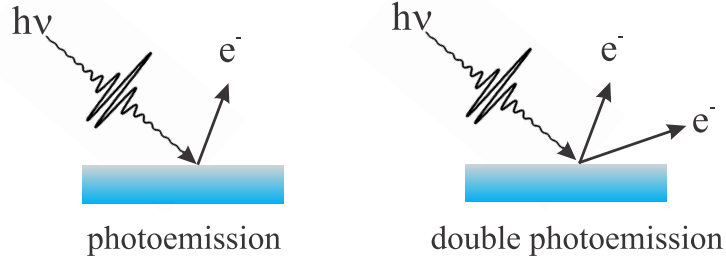


Figure 2.21 Interaction of a photon with a surface; on the left side one electron is emitted, on the right side the possibility of two emitted electrons is depicted.

2.5.1 Double Photoemission (DPE) without Correlation

To probe the correlation and interaction of the electrons the system needs to be excited by photons, electrons, ions or positrons. In this thesis, the excitation is via electrons and the emitted pair is measured in a reflective mode. However, to understand the basic principle of electron pair emission, it is more intuitive to study the interaction with a photon and the emission of an electron pair. One photon hits the surface, as illustrated in Fig. 2.21. It is absorbed by one electron with binding energy E_{vb} . When the incident energy is high enough to overcome the potential barrier of the surface ϕ , it can result in the emission of one electron with kinetic energy E_{kin} (Fig. 2.21 left). The kinetic energy of the electron is $E_{kin} = \hbar\nu - \phi - E_{vb}$. There is also a probability that an electron pair is emitted (Fig. 2.21 right). The first DPE experiment was observed by Gazier and Prescott [77] on Potassium.

The kinetic energy of the pair is $E_{kin} = \hbar\nu - 2\phi - E_{vb}^1 - E_{vb}^2$. For the double ionization of He it was pointed out that without interaction of the electrons it would not be possible to eject two electrons with one photon. This argument holds for any system containing two or more electrons. Mathematically, it is shown that no pair emission occurs in the absence of electron correlation.

The Hamiltonian \mathcal{H} for one electron interacting with an electromagnetic wave with vector potential \mathbf{A} is

$$\begin{aligned}
 \mathcal{H} &= \frac{1}{2m} \left(\mathbf{p} - \frac{e}{c} \mathbf{A} \right)^2 + V(\mathbf{r}) \\
 &= \frac{1}{2m} \left(\mathbf{p}^2 - \frac{e}{c} (\mathbf{p} \cdot \mathbf{A} + \mathbf{A} \cdot \mathbf{p}) + \underbrace{\left(\frac{e}{c} \mathbf{A} \right)^2}_{\rightarrow 0} \right) + V(\mathbf{r}) \\
 &= \underbrace{\frac{1}{2m} \mathbf{p}^2 + V(\mathbf{r})}_{\mathcal{H}_0} - \underbrace{\frac{e}{2mc} (\mathbf{p} \cdot \mathbf{A} + \mathbf{A} \cdot \mathbf{p})}_{\mathcal{H}_{ww}} .
 \end{aligned} \tag{2.43}$$

The Hamiltonian \mathcal{H} is the sum of the unperturbed part \mathcal{H}_0 and the perturbed part \mathcal{H}_{ww} . The quadratic term of the vector potential $(e\mathbf{A})^2$ is neglected, because we assume that $\mathbf{A} \cdot \mathbf{p} \gg$

$e/c\mathbf{A}^2$.

For two electrons, the equation is similar to the situation when we consider no electron-electron interaction

$$\mathcal{H} = \underbrace{\frac{1}{2m}(\mathbf{p}_1^2 + \mathbf{p}_2^2) + V_1(\mathbf{r}_1) + V_2(\mathbf{r}_2)}_{\mathcal{H}_{01} + \mathcal{H}_{02}} - \underbrace{\frac{e}{2mc}((\mathbf{p}_1 \cdot \mathbf{A} + \mathbf{A} \cdot \mathbf{p}_1) + (\mathbf{p}_2 \cdot \mathbf{A} + \mathbf{A} \cdot \mathbf{p}_2))}_{\mathcal{H}_{w1} + \mathcal{H}_{w2}}.$$

To calculate the electron transition probability $\omega_{i \rightarrow f}$ from initial state Ψ_i to final state Ψ_f , we apply Fermi's golden rule

$$\omega_{i \rightarrow f} = \frac{2\pi}{\hbar} |\langle \Psi_f | \mathcal{H}_{ww} | \Psi_i \rangle|^2 \rho(E - E_f - E_i - \hbar\omega). \quad (2.44)$$

Dealing with two electrons refers to a many body problem. Furthermore, the electrons are identical particles. The wave function is determined by the Slater determinate; implement this to the initial state

$$\begin{aligned} \Psi_i &= \begin{vmatrix} \Psi_{i1}(x_1) & \Psi_{i1}(x_2) \\ \Psi_{i2}(x_1) & \Psi_{i2}(x_2) \end{vmatrix} \\ &= \Psi_{i1}(x_1)\Psi_{i2}(x_2) - \Psi_{i1}(x_2)\Psi_{i2}(x_1). \end{aligned} \quad (2.45)$$

Accordingly, the final state is described as $\Psi_f = \Psi_{f1}(x_1)\Psi_{f2}(x_2) - \Psi_{f1}(x_2)\Psi_{f2}(x_1)$. Operating Fermi's golden rule to each perturbation operator \mathcal{H}_{ww} separately results for \mathcal{H}_{w1} in

$$\omega_{i \rightarrow f} \propto \langle \Psi_{f1}(x_1)\Psi_{f2}(x_2) - \Psi_{f1}(x_2)\Psi_{f2}(x_1) | \mathcal{H}_{w1} | \Psi_{i1}(x_1)\Psi_{i2}(x_2) - \Psi_{i1}(x_2)\Psi_{i2}(x_1) \rangle.$$

The equation is a sum, so each term is analyzed separately. Now, we consider wave function $\Psi_{i/f1}$, which is perturbed only by \mathcal{H}_{w1}

$$\omega_{i \rightarrow f} \propto \langle \Psi_{f2}(x_2) | \Psi_{i2}(x_2) \rangle \langle \Psi_{f1}(x_1) | \mathcal{H}_{w1} | \Psi_{i1}(x_1) \rangle. \quad (2.46)$$

The second state is not changed, so the final state is equal to the initial state $\Psi_{f2}(x_2) = \Psi_{i2}(x_2)$ and $\langle \Psi_{f2}(x_2) | \Psi_{i2}(x_2) \rangle = 1$.

Hence no DPE intensity exists in the absence of a finite electron interaction. Since the DPE signal is detected experimentally, the existence of a finite electron correlation is confirmed. This suggests that the signal strength is a measure of the interaction strength. Napitu and Berakdar [13] demonstrate that the DPE signal is proportional to the correlation strength, named U . In the next section, their model is discussed in more detail.

2.5.2 Double Photoemission (DPE) with Correlation

In the previous section we excluded electron correlation in DPE consciously, but now the correlation between the electrons is considered. In this case, the photon (with energy $\hbar\omega$) can be absorbed by one electron and the electron pair is emitted by means of coupling. The photon can

be also absorbed by the center-of-mass coordinate of the two electron system, due to the correlation in the initial and/or final state of the electrons. The theoretical analysis of the DPE shows that the two-electron coincident signal is a signature of inter-electronic interactions [78, 79]. Coulomb potential and Pauli principle are responsible for the correlation between the electrons. To calculate the transition from the initial state to the final state with first order perturbation theory Fermi's golden rule serves

$$W_{i \rightarrow f} = \sum_j |\langle \Psi | \Delta | \Phi_j \rangle|^2 \delta(E - \omega - E_j). \quad (2.47)$$

The final state $\langle \Psi \rangle$ or (34) is reduced to an antisymmetric direct product of two independent $\langle 3 \rangle$ and $\langle 4 \rangle$ so-called "time reversed LEED states". The initial state Φ_j is a summation of all possible two-particle states over the index j with energy E_j . The states have to fulfill energy conservation and dipole selection rules. The dipole operator Δ is a sum of two single-dipole operators. Here the initial state includes correlation and is described by a two-particle function. In contrast to DPE without correlation, where the initial state is the product of two single-particle functions.

DPE with correlation was studied by Napitu and Berakdar [13]. The two particle wave function was constructed within the Hubbard model. Emission of the electron pair is a result of intersite ground state correlation ($R_i \neq R_j$) or on-site correlation ($R_i = R_j$). The latter is more probable and is considered here. The so-called sudden approximation was applied, assuming the excited photo electron pair has no further interaction with the other electrons and the remaining holes. To calculate the two electron wave function Ψ the electrons scatter via a potential with strength U . The detailed calculation is found in Ref. [13].

The key point is that the transition amplitude increases with increasing U . If $U \rightarrow 0$ the intensity vanishes. In other words, for large U value an enhanced DPE signal is expected. We could go so far to postulate that the measured DPE intensity may be an indicator for the strength of U .

In theoretical calculations one can easily change the U parameter. Experimentally variation of the Coulomb repulsion U is more challenging. In our experimental set-up we compare a highly correlated system as NiO, with a weakly correlated as Ag. Furthermore, we investigated a range of metals as Fe, Co, Ni, Cu and Pd.

We should mention, that the experimental results presented in this thesis are based on double excitation via an electron, instead of a photon. This method is called (e,2e). These electrons interact with the electrons in the solid. The theory of (e,2e) is for low energy incoming electrons much more complicated. No theoretical calculations are available at the moment to analyze the (e,2e) intensity in dependence of U .

From the experimental view point, the (e,2e) experiment has the advantage that it is performed in-house lab. In contrast to the (γ ,2e) experiment, where synchrotron radiation is required and the experimental time at the synchrotron source is limited.

Nevertheless, it is reasonable to discuss DPE theory and investigate materials based on DPE calculations. One reason is the similarity between (e,2e) and (γ ,2e) in the sense, that the emission of an electron pair is only possible when electron correlation is switched on.

2.6 Double Electron Emission (e,2e)

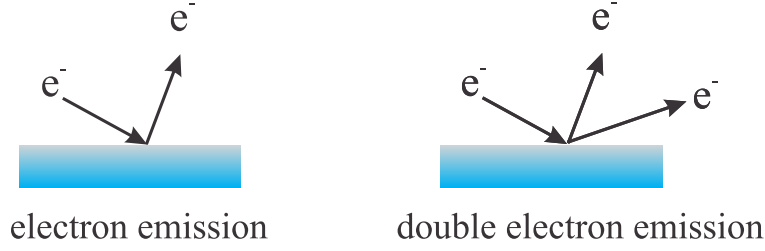


Figure 2.22 Interaction of an electron with a surface; on the left side one electron is emitted, on the right side the possibility of two emitted electrons is depicted.

The current (e,2e) theory of solids is discussed for energies below 100 eV (as used in this work), based on Feder *et al.* [29], Feder and Gollisch [80], Berakdar *et al.* [81]. At low energies, the primary electron and the outgoing electron states involve strong elastic multiple scattering by the ion cores, as known from LEED. This makes the theoretical approach of the (e,2e) cross section difficult and consequently the interpretation of the experimental data is difficult, too.

The primary electron collides with an energy E_1 and a momentum k_1 with a valence electron with energy E_2 , whereby $E_2 < E_F$. What is the probability, that one electron is emitted with energy and momentum E_3, k_3 and a second electron with E_4, k_4 by a single collision event? Besides elastic multiple scattering, no other losses are considered. The time-independent initial state is labeled $|12\rangle$ and the final state $|34\rangle$. The electron-electron interaction Hamiltonian is \mathcal{H}_{ee} .

The transition probability from the initial to the final state is then calculated via first order perturbation theory Fermi's golden rule

$$W_{34,12} = |\langle 34 | \mathcal{H}_{ee} | 12 \rangle|^2 \delta(E_1 + E_2 - E_3 - E_4). \quad (2.48)$$

The transmission probability $W_{34,12}$ is proportional to the observable coincidence rate $I(E_3, E_4)$. The one-electron states $|i, j\rangle$ are expressed in an antisymmetric products of the wave functions $\Psi_{i,j}$

$$|i, j\rangle = [\Psi_i(x)\Psi_j(x') - \Psi_j(x)\Psi_i(x')]/\sqrt{2} \quad \text{with } (i, j) = (1, 2) \text{ or } (3, 4). \quad (2.49)$$

One electron states are obtained as follows: the interaction of each of the four electrons with the nuclei and the ground-state electrons are described by an optical potential. The optical potential describes the elastic scattering and takes into account the virtual and real excitations of non-elastic channels. In the low energy range, relativistic effects due to spin-orbit coupling play an important role. This is known from LEED, valence band structure calculations and photoemission. The wave function $\Psi_i(\mathbf{x})$ consists of four spinors containing the electron spin $\sigma_i = \pm(1, 2, 3, 4)$. In our experiment, neither the primary beam nor the detected electrons are spin analyzed. Theory needs to calculate the cross section for all possible polarization possibilities and to sum them up.

The lattice periodicity is parallel to the surface, this implies that surface-parallel momenta $k_i^{\parallel} = 1, 2, 3, 4$ are good quantum numbers characterizing the one-electron state. Equation (2.48) is nonzero, if the parallel momentum is conserved, $k_1^{\parallel} + k_2^{\parallel} = k_3^{\parallel} + k_4^{\parallel}$. In this notation, the primary electron wave function is $\Psi_1^{\sigma_1}(x)$, representing a relativistic LEED state and the outgoing electrons are $\Psi_{3,4}^{\sigma_{3,4}}(x)$ time reversed LEED states. The valence electrons $\Psi_2^{\sigma_2}(x)$ are obtained with the Bloch wave matching treatment.

The interaction Hamiltonian \mathcal{H}_{ee} of the incident electron with a particular valence electron is written as

$$\mathcal{H}_{ee} = V(\mathbf{x}, \mathbf{x}') = \frac{\exp(-|\mathbf{x} - \mathbf{x}'|/\lambda)}{|\mathbf{x} - \mathbf{x}'|}. \quad (2.50)$$

Magnetic and retarding effects are discarded because the primary energy is small. Only the Coulomb interaction, which is screened by the electrons of the metal are considered with a static potential. The interaction Hamiltonian Eq. (2.50) is used in the transmission probability (Eq. (2.48)).

The next step is to extract electron scattering dynamics from (e,2e) data. In the case of high primary energies, the incident and the ejected wave are described by plane waves. The three dimensional momentum is conserved, hence the observed cross section reflects the momentum density of the target electrons. With low energy electrons the situation is different, because multiple elastic scattering is very important in primary and in ejected electron states. Only two dimensional momentum is conserved, therefore no direct information on the electronic structure is obtained. An important point is, that (e,2e) intensity occurs in regions with high so-called k -DOS, indicating the k resolved DOS. That is visible, when we compare k -DOS at the Γ point and $I(E_3, E_4)$ contour plots for W(100) (Fig. 2.23a,b,c). Furthermore, when the k -DOS vanishes, no (e,2e) intensity is visible. As stated by Feder *et al.* [29] there is no detailed correspondence between k -DOS and $I(E_3, E_4)$. To observe (e,2e) events, it is necessary to have available states, but this is not a sufficient condition. Theoretical plot (Fig. 2.23b) is modified into Fig. 2.23c to get closer to the experimental results. Modifications are due to: energy dependent finite life time of the hole, experimental energy distribution of the primary beam energy E_1 and reduction of the emission cone. Theoretical intensity features are smear out and resemble the experimental obtained data (Fig. 2.23d). In general, a good agreement between theory and experiment is observed for normal incidence primary energy $E_1 = 17.2$ eV. The main contribution at $E_3 = E_4 = 6$ eV is reproduced well. The good agreement between theory and experiment implies that direct collision of incident particle and target are the dominant origin of the two electrons observed experimentally. The valence electrons of W(100) are predominantly d character and for the d states the spin orbit coupling is much stronger than for the sp states. The excited sp states can couple to the vacuum and can form LEED states. This will be later important when we discuss diffraction effects of Ag.

In the work of Berakdar *et al.* [81] the total potential V_{tot} is complemented with a dynamical potential U , describing the interaction between the two electrons. Dynamic means that the interaction of both electrons is strong, when they are close together. When they are fare apart, then the potential diminishes. Total potential V_{tot} is the sum of the two one particle optical potentials

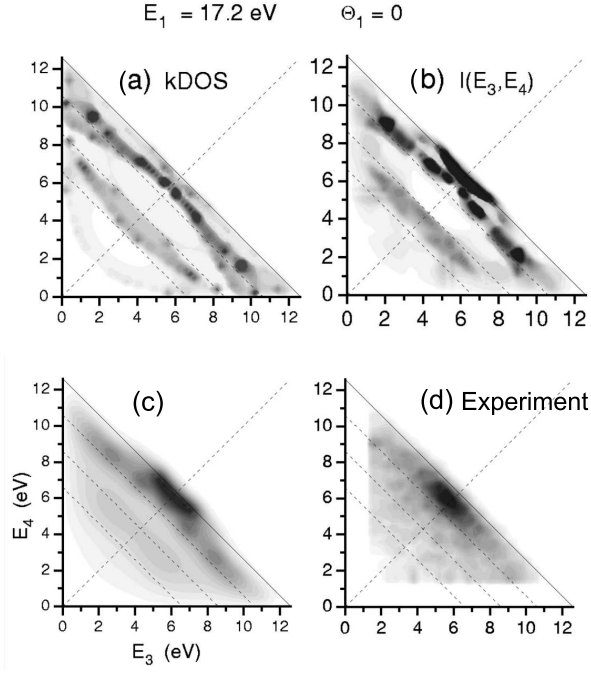


Figure 2.23 Contour plots in the (E_3, E_4) plane of a W(100) surface for $E_1 = 17.2 \text{ eV}$, $\theta_1 = 0^\circ$ and $\theta_{3,4} = 40^\circ$: (a) DOS at the Γ point; (b) calculated $I(E_3, E_4)$; (c) $I(E_3, E_4)$ adapted to experimental conditions; (d) experimental data. Taken from Ref. [29]. Copyright (1998) by the American Physical Society.

(V_3, V_4) and the dynamic potential U . It is identified as Coulomb potential. More precisely the dielectric function $\epsilon(r, r')$ has to be calculated. However, for inhomogeneous electron gas this is a very difficult task. Instead, the Thomas-Fermi screening potential is used (Eq. (2.40)). The distance between the electrons is $r_{34} = r_3 - r_4$.

The total potential is rewritten as

$$V_{tot} = V_3 + \frac{Z_3}{r_3} + V_4 + \frac{Z_4}{r_4}. \quad (2.51)$$

The strength of the screening is determined by Z_i . Single particle potentials are augmented by the term Z_i/r_i . Inter-electronic correlation is subsumed into a dynamic non-local screening of the electron core interaction. Calculation predict a strong influence of U on the pair correlation. The theory was applied to the same experimental conditions as in Ref. [29] for $E_1 = 17.2 \text{ eV}$ and comes to the same result. The contour plot remains practically unchanged, concluding pair correlation effects are rather small. However, when the primary energy is lowered to 10.6 eV drastic changes occur. When the Coulomb interaction is switched off, the intensity is reduced at the Fermi edge for equal energies $E_3 = E_4$. In contrast, when the Coulomb interaction is switched on the intensity has a maximum at this point. This is in agreement with the experimental data, Fig. 2.24. Coulomb interaction can transfer energy from one escaping electron to the other. That is the reason why equal energy sharing is preferred, so $E_3 = E_4$ gives high intensity.

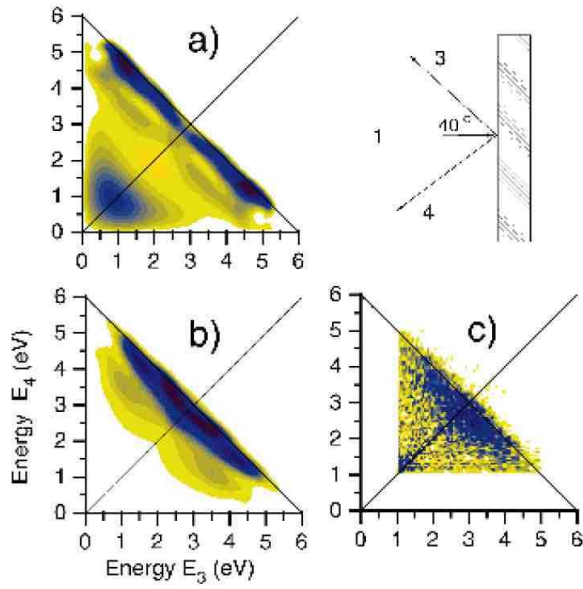


Figure 2.24 Spin-average intensity for the two-electron emission from a W(100) surface following the impact of a 10.6 eV electron along the surface normal. Contour plots in the (E_3, E_4) plane show calculated results without Coulomb pair correlation (a), with pair correlation (b) and the experimental data (c). Taken from Ref. [81].

3 Experimental Background

The experiment is performed in an Ultra High Vacuum (UHV) chamber at a pressure of 7×10^{-11} mbar. The sample is excited with an electron gun from Kimball. The emitted electron pair is analyzed by two hemispherical analyzers from Scienta and detected with multichannel plate (MCP) - resistive anode. The detectors are connected via a coincidence logic. The primary electron flux is measured with a MCP. The components and the sample preparation will be explained in more detail in this chapter.

UHV conditions are required to have as long as possible a defined surface without residual adsorbates like H, CO. Data acquisition time is long, around 3 counts/s are collected. The experiment is highly surface sensitive (the information comes mainly from the first 3 monolayers (ML)). To reach and maintain the UHV a turbo pump, an ion getter pump, a titan sublimation pump (TSP) at the chamber and two TSP at the analyzers are installed.

To understand the experimental set-up, the demands on a coincidence experiment needs to be discussed.

3.1 Coincidence Demands - General Statements

The most fundamental question in coincidence measurements is: How can we identify a correlated pair of two electrons emerge from one scattering event? The problem is discussed in Ref. [14, 82, 83, 84, 85].

The scattering event happens at time t_0 and the two emitted electrons will arrive at times $t_0 + t_1$ and $t_0 + t_2$ at the detectors. The characteristic traveling time difference is $t = |t_1 - t_2|$. This is a common method to identify particles emerging from the same process. In practice one has to allow a time spread of $t \pm \delta t$, which consist of all possible sums of the time variations of the traveling times of particle 1 and 2, δt_1 and δt_2 . The flight time consist of passing trough the analyzer, the detector and the electronics. We assume that the electrons are emitted simultaneously. A typical arrival time histogram is shown in Fig. 3.1. Our set-up is symmetrical with respect to the sample, so the traveling times t_1 and t_2 are equal. A clear peak at $t = 0$ ns is observed. Electrons are considered to arise from the same event, when they lay in-between the peak, which is limited by two vertical dashed lines. For our set-up and energies $\delta t \approx \pm 10$ ns. The width of the peak depends on the energy difference of the pair and the time resolution of the instrument. The time resolution is limited by the geometry of the hemispheres, the lenses, the flight time to the channel plate detectors and the electronics.

Two coincidence events has to be distinguished - true and random events. True events result from one scattering process (blue area in Fig. 3.1). Random or also called accidental events

are due to two independent scattering processes. The reason is that more than one electron is emitted from the electron gun in the time interval $t + \delta t$. The distribution of random electron pairs is homogeneous, in contrast to true events, where a clear preference for equal times can be recognized. The yellow and orange area in Fig. 3.1 consists of purely random events. In the experiment, blue and orange events are measured together.

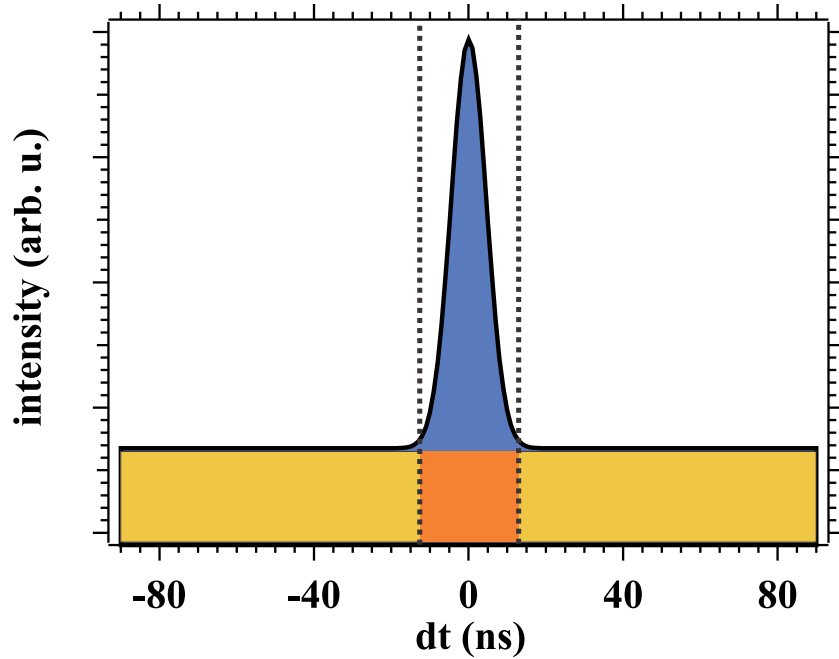


Figure 3.1 Typical arrival time histogram of two emitted electrons. Electrons are considered to arrive at the same time, when their difference is $0 \text{ ns} \pm 10 \text{ ns}$. True (blue) and random (orange) events in this interval cannot be separated. The homogeneous random background is yellow.

The quality of the experiment is judged by the ratio between true and random events. Without considering the shape of the arrival-time histogram, here some general statement to the coincidence technique, which is special in comparison with single electron detection. In a single spectroscopy experiment high counting rates are desirable to maximize the signal-to-noise ratio for a given measuring time. High rates can be achieved with high incoming flux, probing a large sample area and high transmission of the analyzer. In a coincidence experiment this is not anymore valid for improving the experimental performance, because one cannot distinguish between true and random coincidence events. For example increasing the incoming flux raises the true count rate, but reduces the true-to-random-ratio. Hence the signal-to-noise ratio declines, too.

The true signal T is calculated

$$T = \alpha_1 \alpha_2 R V_c t \quad (3.1)$$

$$= B \cdot I \cdot t, \quad (3.2)$$

α_i is the efficiencies of the detectors, depending on the experimental parameters such as energy

and angular resolution. R is the electron creation rate per unit time and per unit volume, which is direct proportional to the incoming flux. The common shared volume of both detectors is V_c and t is the counting time. The parameters of Eq. 3.1 are rearranged with $\alpha_1\alpha_2RV_c = B \cdot I$ and Eq. 3.2 is formed. Obviously, T depends linearly on the incoming flux I .

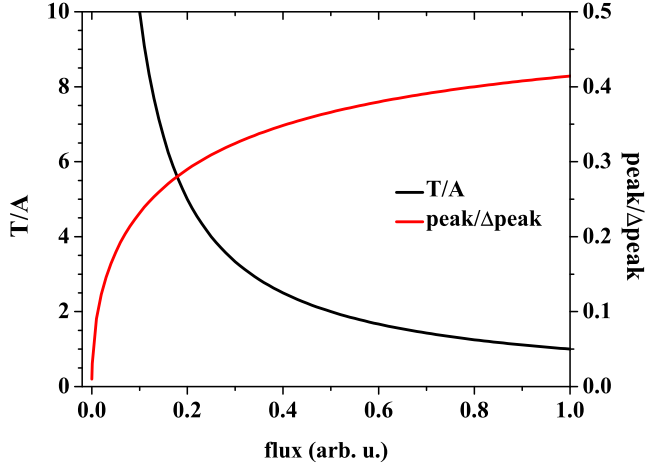


Figure 3.2 True-to-accidental ratio T/A (left scale) and the true signal-to-noise ratio $\text{peak}/\Delta\text{peak}$ (right scale) in dependence of the incoming flux in arbitrary units.

The accidental signal A is the linear product of two single rates (S_i) and the finite probability of two unrelated events occurring within time τ

$$A = S_1 S_2 \tau t \quad (3.3)$$

$$= \alpha_1 \alpha_2 V_1 V_2 R^2 \tau t \quad (3.4)$$

$$= C \cdot I^2 \cdot t. \quad (3.5)$$

Here we recognize an important point: The true rate is proportional to the incoming flux I or R and the accidental rate is proportional to R^2 or rather I^2 , when the parameters are substituted as $\alpha_1 \alpha_2 V_1 V_2 R^2 \tau = C \cdot I^2$.

We set all parameters to 1 and the ratio T/A simplifies to

$$\frac{T}{A} \propto \frac{1}{I}. \quad (3.6)$$

The ratio T/A increases by lowering the flux and the contribution of the accidental counts becomes negligible, but also probability is reduced to detect a true event at all. At high flux T/A goes to 0.

The arrival-time-histogram (Fig. 3.1) includes true and random events. We are only interested in the true events T , so the random events A need to be subtracted. In formulas it is written as $\text{peak} = (T + A) - A$. The error Δpeak is the sum of $\sqrt{T + A}$ and \sqrt{A} .

The signal-to-noise ratio (SNR) is obtained as

$$\frac{\text{peak}}{\Delta\text{peak}} = \frac{(T + A) - A}{\sqrt{T + A} + \sqrt{A}} = \frac{B \cdot I \cdot t}{\sqrt{B \cdot I \cdot t + C \cdot I^2 \cdot t} + \sqrt{C \cdot I^2 \cdot t}} \quad (3.7)$$

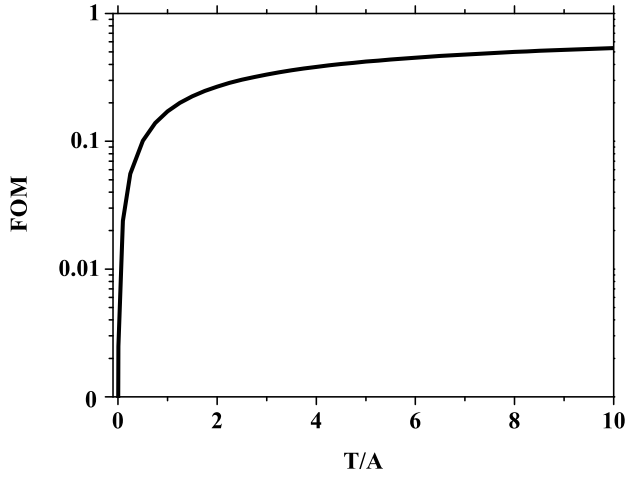


Figure 3.3 Figure of merit (FOM) of the signal-to-noise ratio between true T and random A events. Maximum signal-to-noise ratio is reached at 1.

The SNR increases, when the flux is increased. T and A contribute in statistical noise, while only T contains information of interest. Both equations (Eq. 3.6 and Eq. 3.7) are plotted in Fig. 3.2 in dependence of the primary flux in arbitrary units. We notice, increasing the flux, increases the probability of a true event and increases the signal-to-noise ratio. On the other hand, the ratio T/A is decreased. A compromise has to be found.

A good value of T/A is 4 at a flux of 0.25 arb.u. and the SNR is 0.3. When the flux is halved, the ratio T/A is increased to 8, but the SNR is decreased by one order of magnitude.

When the extreme case of infinite flux ($I \rightarrow \infty$) is considered, Eq. 3.7 simplifies to

$$\left(\frac{\text{peak}}{\Delta\text{peak}} \right)_{I \rightarrow \infty} \approx \frac{T}{2\sqrt{A}}. \quad (3.8)$$

We obtain the figure of merit (FOM)

$$\text{FOM} = 1 - \frac{\frac{\text{peak}}{\Delta\text{peak}}}{\left(\frac{\text{peak}}{\Delta\text{peak}} \right)_{I \rightarrow \infty}} = 1 - \frac{2}{\sqrt{\frac{T}{A} + 1} + 1}. \quad (3.9)$$

If the ratio T/A converges to 0, the FOM approaches 0, too. Hence the signal-to-noise ratio is the poorest. If FOM is equal to 1 the best signal-to-noise ratio would be reached. Equation 3.9 is plotted in Fig. 3.3 in dependence of T/A . The graph increases steeply from 0 to 2 and then saturates slowly at a FOM of 1. A trade off value is around 4 – 5. A further increase of the ratio, increases the FOM not significantly. A significantly decreased flux would result in an extension of the data acquisition time. Nevertheless, to have an acceptable ratio between true and random counts, we operate the experiment under low primary flux.

To estimate how many electrons are emitted from the electron gun and hit the surface in a defined period of time, the Poisson distribution is a reasonable choice. The distribution is valid

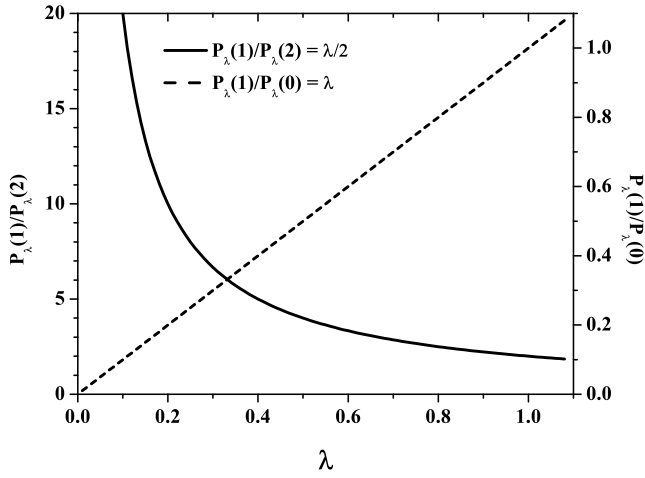


Figure 3.4 Probability ratios $P(1)/(2)$ (straight line) and $P(1)/P(0)$ (dashed line) as function of the average number of electrons hitting the surface λ .

to calculate the probability $P_\lambda(n)$ of a discrete event n happening in a fixed period of time. λ represents the average number of electrons hitting the surface in the time interval.

The Poisson distribution $P_\lambda(n)$ is

$$P_\lambda(n) = e^{-\lambda} \frac{\lambda^n}{n!}. \quad (3.10)$$

We work at low electron flux, therefore the Poisson distributions for up to two electrons are of interest

$$P_\lambda(0) = e^{-\lambda}, \quad P_\lambda(1) = e^{-\lambda}\lambda, \quad P_\lambda(2) = e^{-\lambda} \frac{\lambda^2}{2}. \quad (3.11)$$

The parameter λ can be adjusted with the electron flux. To obtain a high true coincidence count rate, the probability of two emitted electrons should be low.

The probability ratio of one to two is $\frac{P(1)}{P(2)} = \frac{2}{\lambda}$. It is plotted as function of the average number λ in Fig. 3.4. If λ is equal to 1, the probability of finding one electron to two electrons is 2. When λ is decreased by 10, the ratio $P(1)/P(2)$ is increased by 20.

On the other hand when the flux is too low, no electron at all might be emitted from the filament. The ratio $\frac{P(1)}{P(0)}$ is equal to λ , represented by the dashed line in Fig. 3.4. When λ is 0.1, the probability of one emitted electron is close to zero. This underlines the difficulties of the coincidence experiment.

3.2 Experimental Set-up

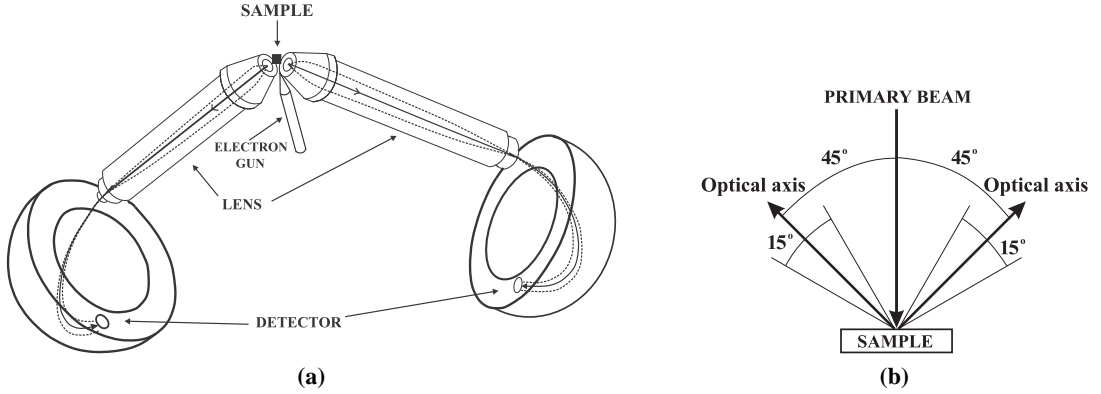


Figure 3.5 (a) Experimental (e,2e) set-up. The electrons are emitted from the electron gun and focused on the sample. The incoming electrons excite an electron from sample. The electrons travel through the energy selective elements, the lenses and the electrostatic hemispherical analyzers. At the end they reach the detectors. (b) Geometrical set-up. The primary beam hits the surface perpendicular. The electron pairs are detected under an angle of $45 \pm 15^\circ$.

For the (e,2e) experiment first of all an electron gun is required (see Fig. 3.5a). The electrons are accelerated up to 68.6 eV here. The low energy electrons are focused on the sample and hit the surface perpendicular. As discussed in Sec. 2.6, there is a probability, that the reflected electron excites an electron from the valence band. The electron pair is emitted from the sample and detected in an angle of $45 \pm 15^\circ$ (see Fig. 3.5b).

The electrons are transferred through electrostatic lenses to the electrostatic hemispherical deflection analyzers (HDA). When the electrons enter the HDA, they pass through a slit of 1 mm width. The experiment is performed under symmetrical conditions, which implies symmetrical geometry, lens and analyzer voltages.

The HDA serves as energy dispersive element. It consists of two concentric hemispherical electrodes with radii $R_1 = 160$ mm and $R_2 = 240$ mm, which are at different potentials

$$V_1 = \frac{E_{\text{pass}}}{e} \left[3 - 2 \left(\frac{R_0}{R_1} \right) \right] \quad (3.12)$$

$$V_2 = \frac{E_{\text{pass}}}{e} \left[3 - 2 \left(\frac{R_0}{R_2} \right) \right]. \quad (3.13)$$

The mean radius R_0 of the hemispheres is 200 mm. The pass energy E_{pass} is defined as the energy where the trajectories of the electrons describe a circle. If the electron energy is lower or higher than E_{pass} the motion of the electrons are described as elliptical Kepler trajectories. If the energy is sufficiently lower or higher, the electrons will hit the wall of the electrodes.

Finally, the electrons are detected by two micro channel plates (MCP) connected to a resistive anode. The diameter of each MCP is 40 mm. The electron pair is recognized by a coincidence logic. Electrons that arrive at the “same” time are of interest. The “same” time is defined as a time slot of 20 ns.

We are dealing with a low incoming flux and it is expected that few electrons are emitted from the sample surface. Hence, a device with high detection efficiency is needed. For this purpose the MCP is used. It is an array of small tubes or channels filled with lead and embedded in a glass mesh. The channels are tilted about 8° to increase the efficiency. The primary electron is multiplied by a factor of 10^6 due to the production of secondary electrons. For the coincidence experiment, we use a stack of two MCP to improve the performance.

To measure the position of the electron additionally a resistive anode is included [86]. The position is transformed to energy with help of the specular electron beam. The position signal, which corresponds to the energy, for right and left detector goes directly to a digitizer. Time and energy information are triggered when the four signals, two MCP and two anode signals, are in coincidence. Then the information of the pair is stored in a computer. During the measurement the spatial information (the MCP screen) is monitored in real time with an oscilloscope.

If the start and stop pulse is coming from the same detector, the time resolution of the electronics is obtained. The obtained time jitter of the electronics is 0.7 ns.

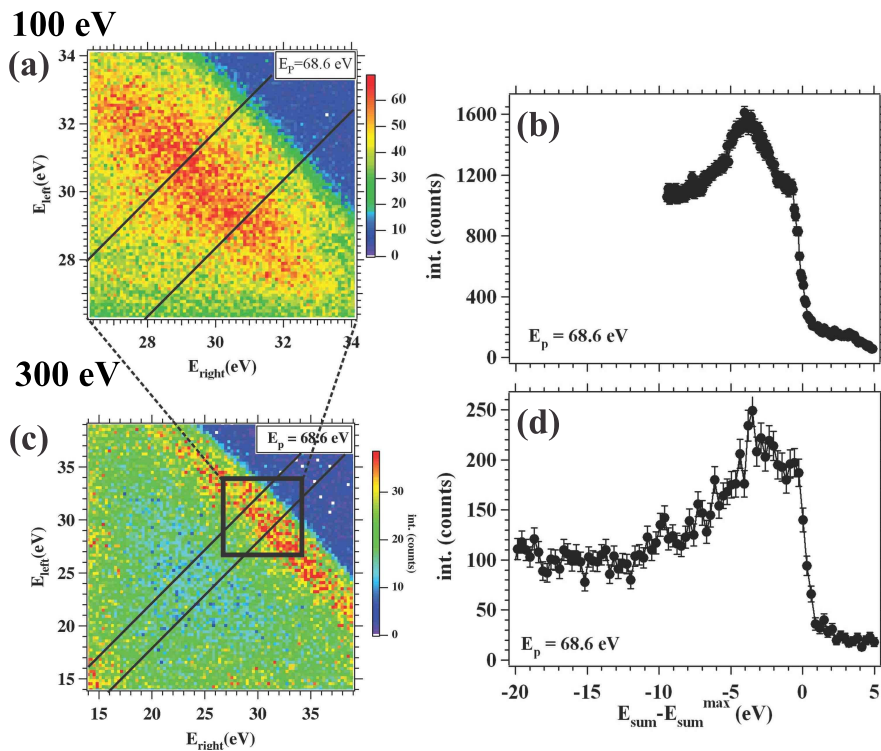


Figure 3.6 2D (a, c) and sum energy spectra (b, d) of NiO for $E_p = 68.6$ eV. The spectra (a, b) presents the results for $E_{\text{pass}} = 100$ eV. The energy window is $8 \text{ eV} \times 8 \text{ eV}$. The spectra (c, d) show the results for $E_{\text{pass}} = 300$ eV (energy window of $24 \text{ eV} \times 24 \text{ eV}$). With both settings the same features are seen, but the energy resolution of the $E_{\text{pass}} = 100$ eV is better. The $E_{\text{pass}} = 100$ eV plot is a close up of the $E_{\text{pass}} = 300$ eV data.

The experiment was operated with pass energies of 100 and 300 eV. The energy window is 8 % of the pass energy. It is possible to accumulate data in an energy window of $8 \text{ eV} \times 8 \text{ eV}$ and $24 \text{ eV} \times 24 \text{ eV}$, accordingly.

The energy information of the electron pairs is combined in a 2D energy spectrum as is seen for NiO ($E_p = 68.6$ eV) for $E_{\text{pass}} = 100$ eV (Fig. 3.6a) and for $E_{\text{pass}} = 300$ eV (Fig. 3.6c). The bottom scale refers to the energy of the electron arrived at the right detector. The left scale represents the energy of the electron which arrived at the same time at the left detector. Coincidence intensity is reproduced by a color scale. Red stands for high intensity and blue for few counts.

Energy conversation of the pair holds

$$E_p + E_{\text{vb}} = E_{\text{left}} + E_{\text{right}} + \phi_{\text{sample}} = E_{\text{pair}} + \phi_{\text{sample}}. \quad (3.14)$$

The sample work function is labeled with ϕ_{sample} and the valence band energy is E_{vb} . The spectrum is analyzed in detail in the result section (Sec. 4.2). Obviously, the 300 eV 2D plot is a zoom of the 100 eV plot. The main signal is in the energy region of $E_{\text{vb}} \approx 0$. No further information is obtained from the 300 eV plot, besides a homogeneous background in the lower energy region. To analyze the spectra qualitatively, the sum of the pair is plotted in the interval $|E_{\text{left}} - E_{\text{right}}| \leq 2$ eV. (In this respect, errors due to the geometry of the plot are excluded. For example, the total diagonal line $E_{\text{left}} = E_{\text{right}} = 34$ eV contains more pixel than $E_{\text{left}} = E_{\text{right}} = 28$ eV.) The sum energy spectrum of $E_{\text{pass}} = 300$ eV (Fig. 3.6d) covers a wider energy window than the sum energy spectrum of $E_{\text{pass}} = 100$ eV (Fig. 3.6b). But the energy resolution for a wider window is worse than for the smaller window.

The energy resolution is estimated with help of the Fermi edge of Ag sum energy spectra. The energy resolution are for $E_{\text{pass}}(100$ eV) ≈ 1.1 eV and $E_{\text{pass}}(300$ eV) ≈ 1.75 eV. The energy resolution includes the energy spread of the electron gun (0.3 eV) and aberration errors of the lenses. Spherical and chromatic aberration can be distinguished. The origin of spherical aberration is that peripheral rays are bent stronger than rays closer to the optical axis. Chromatic aberration is a result of a never perfectly mono energetic electron beam. The energy resolution depends furthermore on the transmission of the hemispherical analyzers and the accuracy in the impact position on the MCP. Nevertheless, the resolution is mainly depending on the spectrometer, in particular on E_{pass} . Consequently, we obtained all data throughout the experiment with $E_{\text{pass}} = 100$ eV in favour of the energy resolution.

The flight time T of the electron inside the sphere is calculated accordingly to Ref. [87, 88]

$$T = \frac{2mA}{l} = \frac{l^3}{mk^2} \int_0^\pi \frac{d\theta}{(1 + \epsilon \cos(\theta - \theta_0))^2}. \quad (3.15)$$

where A is the area enclosed by the orbit within the analyzer and l is the angular momentum. The parameter k reflects the relationship of the voltages to the dimensions of the spectrometer. In the case, when the orbitals describe a circle is $k = 2ZeE_{\text{pass}}R_0$. ϵ is the so-called eccentricity of the electron trajectories and depends among others on E_{pass} . Radius of the trajectory depends on the angle θ .

For one cycle the electron needs for $E_{\text{pass}} = 100$ eV a time of 105.9 ns and for $E_{\text{pass}} = 300$ eV

a time of 61.1 ns. Taking into account the covered energy window, the time difference of the slowest and fastest electron is obtained. For $E_{\text{pass}} = 100 \text{ eV}$ the time difference is 5 ns and for $E_{\text{pass}} = 300 \text{ eV}$ the value is 9 ns. This results in a time spread for the electron pair of 7.1 and 12.7 ns, respectively. Experimentally, the FWHM of the arrival time histogram for $E_{\text{pass}} = 100 \text{ eV}$ is 11.4 ns and for $E_{\text{pass}} = 300 \text{ eV}$ the FWHM is 17.5 ns. Experimental and calculated value are consistent.

An important component of the experimental set-up was a detector to measure the primary flux, so the number of pairs produced by one incoming electron was determined quantitatively. For this purpose a small MCP was mounted on a manipulator, which could be brought into the sample position. The active area had a diameter of 5 mm. To save the life-time of the microtron the flux f_{single} of the electron gun was set to 200000 counts/s. The grid voltage of electron gun was increased accordingly. After “calibrating” the gun, the sample was set in experimental position and the “single” count rate s_{single} was determined in coincidence set-up. The single count rate in this configuration is for Ag in the range of 50 counts/s to 450 counts/s, and no measurable coincidence events happen. (It is very important to make sure, that the dark counts, produced by ion gauge and ion getter pump, are below 1 % of the single counts. During primary flux measuring the dark count sources, as ion gauge and ion getter pump, were switched off.) To measure the pair emission we had to increase the flux significantly by decreasing the grid voltage. When around 2.5 counts/s pairs could be detected on the rate meter (random and true coincidences), the single counts s_{coin} in this configuration were around 1800 counts/s to 3500 counts/s.

The electron flux f_{coin} during the coincidence experiment is calculated as follows

$$f_{\text{coin}} = \frac{f_{\text{single}}}{s_{\text{single}}} \cdot s_{\text{coin}} \quad (3.16)$$

After inserting the according values, the calculated flux f_{coin} during the experiment varies from $1.5 - 7.5 \times 10^6$ counts/s depending on the primary energy. Proceeding in this way is allowed, because the relationship between the single HDA counts and the single flux meter counts are linear, as is demonstrated in Fig. 3.7. Furthermore, the validity of linear regression is manifested by the 0 origin.

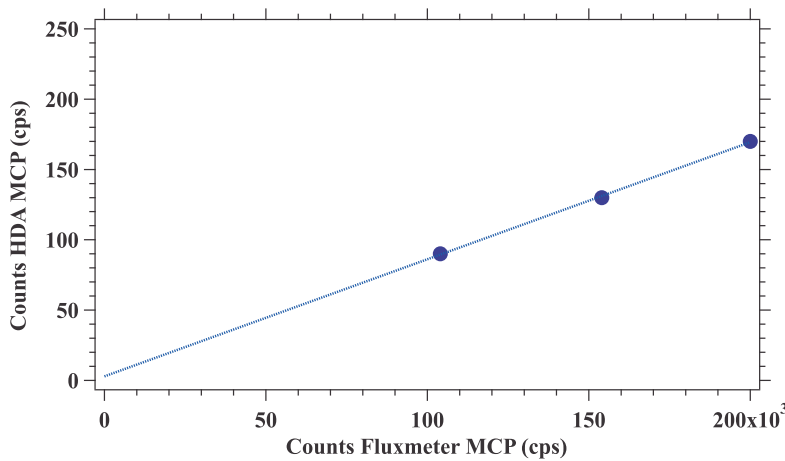


Figure 3.7 The relationship between single HDA counts and flux meter counts is linear.

3.3 Sample Preparation

To prepare the Ag(100) crystal and grow NiO, CoO film and transition metals Fe, Co, Ni, Cu and Pd the preparation chamber was equipped with an Argon sputter gun, Auger electron spectroscopy, LEED optics, the needed evaporator as Fe, Co, Ni, Cu, Pd and an oxygen inlet, Fig. 3.8. Besides pressure controlling with an ion gauge, the gas concentration could be monitored with a mass spectrometer.

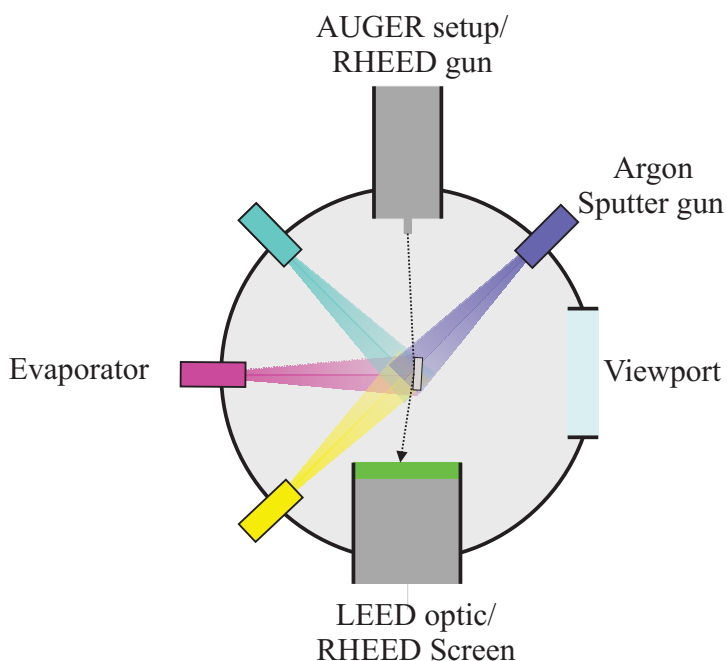


Figure 3.8 The preparation chamber is equipped with a LEED (low energy electron diffraction) optics, Auger system, various evaporators (Fe, Co, Ni, Cu, Co, Pd), an Argon sputter gun and an oxygen inlet (not shown here).

The Ag crystal was cleaned by standard procedure, which involves Ar^+ sputtering and annealing cycles. Sputtering energy was 3 keV and the pressure 1.5×10^{-7} mbar. The annealing temperature was 400 °C [89]. Mounting the sample after transportation yields to sputtering for 24 h. The cleanliness was controlled by Auger electron spectroscopy. The structure quality and the alignment was checked with LEED. In Fig. 3.9a the diffraction pattern for $E_p = 55$ eV is displayed. Sharp black spots are visible, which is the indication for a clean and well structured cubic surface.

NiO was grown on clean Ag(100) substrate as a non reactive material with molecular beam epitaxy (MBE). The lattice constant of bulk Ag at room temperature is 4.09 Å and the one of NiO is 4.17 Å. This corresponds of a lattice mismatch of 2%. Ag crystal has a face centered cubic structure and NiO a rock salt structure. This growth of NiO on Ag is well established in the literature [90, 91, 92].

Ni is evaporated in a O_2 atmosphere via molecular beam epitaxy. The quality of the films were analyzed with LEED. Cubic arranged sharp spots diffraction are monitored (Fig. 3.9b). The chemical composition of the films was checked by detecting the Auger electrons with a cylindrical mirror analyzer (CMA). The incident electron beam has an energy of 3 keV.

The optimized growth parameters are: oxygen pressure $p(\text{O}_2) = 10^{-6}$ mbar and substrate tem-

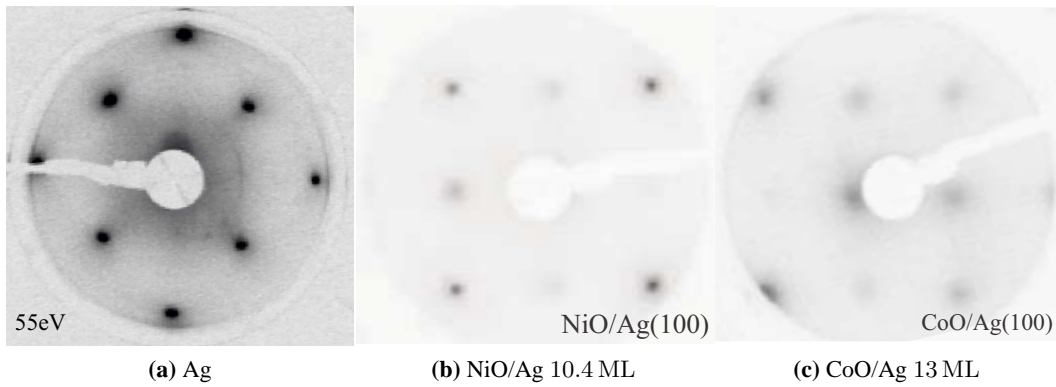


Figure 3.9 LEED pattern of (a) a Ag(100) crystal ($E_p = 55$ eV), (b) NiO film ($E_p = 90$ eV) and (c) CoO film ($E_p = 90$ eV).

perature of $T = 200$ °C.

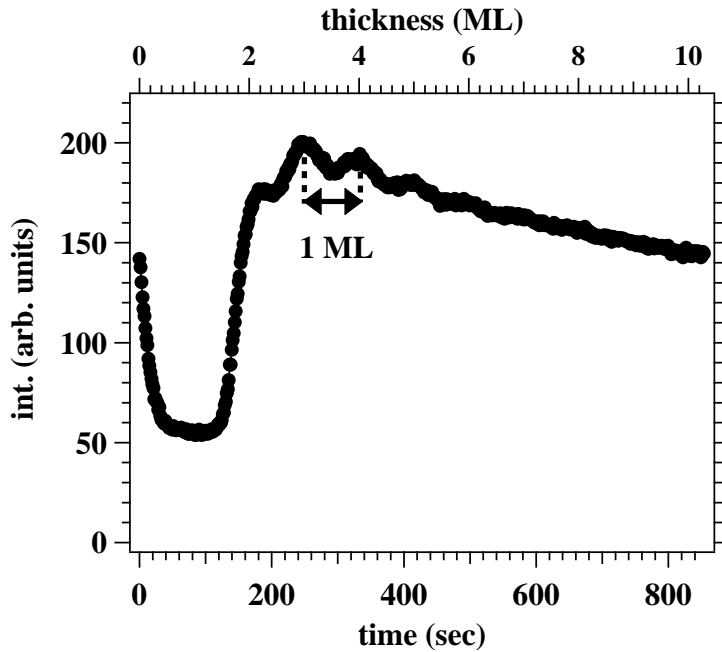


Figure 3.10 NiO film growth of 10.4 ML on Ag(100) measured with MEED (medium electron energy diffraction). The indicated growth rate is 1 ML/84 s. This curve was obtained with a primary energy of 1.5 keV. Taken from Ref. [93]. ©IOP Publishing. Reproduced by permission of IOP Publishing. All rights reserved.

As far as thickness control is concerned we observed the medium energy electron diffraction (MEED) intensity variation during growth. In such an experiment a primary electron beam hits the target under a grazing incidence and the diffracted beams are detected on a phosphorous screen, as sketched in Fig. 3.8. Layer-by-layer growth is manifested by the emergence of intensity oscillations as a function of time. Assuming that a period corresponds to 1 ML, a thickness calibration is possible. A typical MEED plot is shown in Fig. 3.10 for a 10.4 ML film. This curve was obtained with a primary energy of 1.5 keV and we measured the intensity of the specular reflected beam. The deposition starts at time $t = 0$ and we note that at the beginning of the growth the intensity drops markedly, only at approximately $t = 170$ s the initial intensity is recovered. After this we observe the onset of weak oscillations. We identify this interval as

the time required to deposit 1 ML of NiO. The evaluation yields to a growth rate of 84 s/ML. With this calibration we can convert growth time in ML and the result is given as the upper x-axis in Fig. 3.10. Our MEED intensity curve is qualitatively in agreement with a recent work although our oscillation amplitude is smaller [6]. Previous STM/STS¹ studies found that in the early stages of the growth a complex behavior exists [94]. Only at coverages above 2 ML was a band gap observed. These growth complications manifest themselves also in stress and structural measurements [6]. We conclude that starting at coverage of 2 ML NiO we are to expect properties related to a “highly correlated” material.

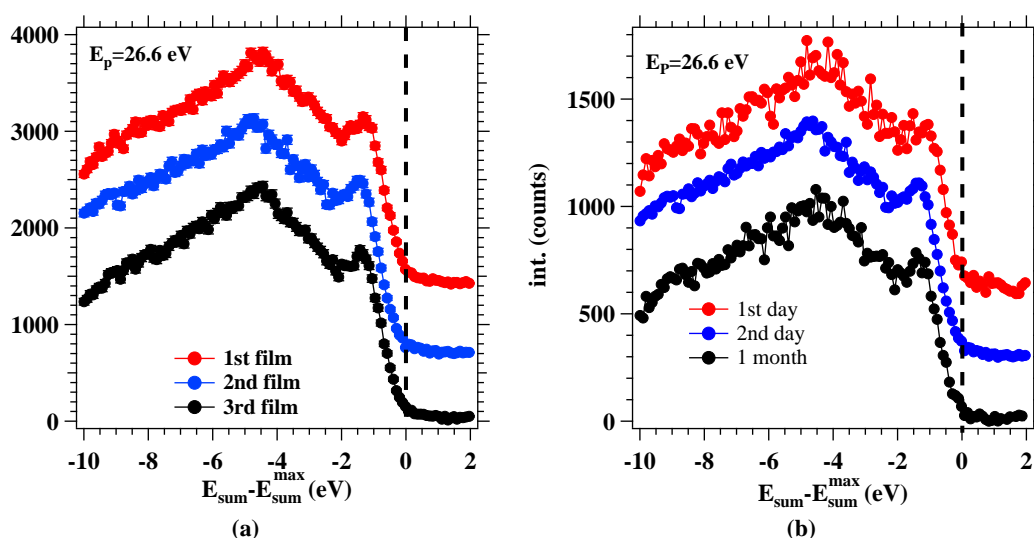


Figure 3.11 (a) Reproducibility of NiO film. Growth of three films under the same conditions show no change in sum energy spectra. (b) Stability of NiO film. After one month the spectra do not change. The spectra are obtained with $E_p = 26.6$ eV.

The easy preparation of NiO allows us to reproduce, under the same conditions, the same NiO film. This is manifested in Fig. 3.11a. The sum energy spectra for three different films are shown in red (1st), blue (2nd) and black (3rd) for a primary energy of 26.6 eV. The spectra are identical, so we can conclude the film quality is the same.

Another advantage of NiO film is, that the surface stays clean for a long time. To obtain a (e,2e) spectrum with good statistics takes up to one week, it is a benefit to measure the hole time the same sample. Residual gases as CO are not deposited at the surface during one month, confirmed with Auger measurements. (e,2e) technique is even more surface sensitive than Auger measurements. Sum energy spectra obtained after one day (red), the second day (blue) and after one month (black) are presented in Fig. 3.11b for a primary energy of 26.6 eV. No difference in the spectra are observed. We conclude that the film structure and morphology has not changed.

¹scanning tunneling spectroscopy

4 Experimental Results

4.1 (e,2e) on Ag(100)

A recent (e,2e) study on a Cu(100) surface revealed the importance of pair diffraction [31]. A kinematic pair diffraction model described the results reasonably well. The approach is justified by current (e,2e) theory, which characterizes the incoming and outgoing electrons by LEED and time reversed LEED states, respectively. In order to explore the validity of the kinematic model, the experiment was repeated with a metal having similar electronic properties like the Ag(100) crystal. A difference between Cu and Ag is the lattice constant a , which has a value $a(\text{Cu}) = 3.06 \text{ \AA}$ and $a(\text{Ag}) = 4.09 \text{ \AA}$. This results in a shift of the kinematic diffraction peaks to lower energies with a larger lattice constant. We have systematically studied the electron pair emission from the Ag(100) surface as a function of the primary energy. An improvement to the previous experiment is the ability to measure the primary electron flux. This allows to determine the single and coincidence count rate per incoming electron.

4.1.1 Energy Spectra

During the measurement, the Ag(100) surface was in the [001] scattering plane. The (e,2e) spectra are obtained for different primary energies in the range from 30 to 67 eV. The detection window is for all energies the same. The voltage of lenses and analyzers were adjusted according to the primary energy E_p . Some 2D net spectra are displayed in Fig. 4.1. Net spectra means that the random background events are already subtracted.

To calculate the maximum sum energy $E_{\text{sum}}^{\text{max}}$ of the electron pair, the work function has to be subtracted only once, because the primary electron gains the work function when entering the sample. It is expressed as $E_{\text{sum}}^{\text{max}} = E_p - \phi_{\text{sample}}$, with $\phi_{\text{sample}} = 4.6 \text{ eV}$. A primary energy of $E_p = 37 \text{ eV}$ gives $E_{\text{sum}}^{\text{max}} = 32.4 \text{ eV}$ (see Fig. 4.1a). When the energy is shared equally, the energy of the left and right electron is $E_{\text{left}} = E_{\text{right}} = 16.2 \text{ eV}$. The $E_{\text{sum}}^{\text{max}}$ line is indicated by a grey diagonal line. The energy levels can be seen in Fig. 4.2. To calculate the primary energy of the electrons, the work function of the filament ϕ_{fila} (2.6 eV) has to be considered as well. The emitted electrons originate from the highest occupied state, the Fermi energy.

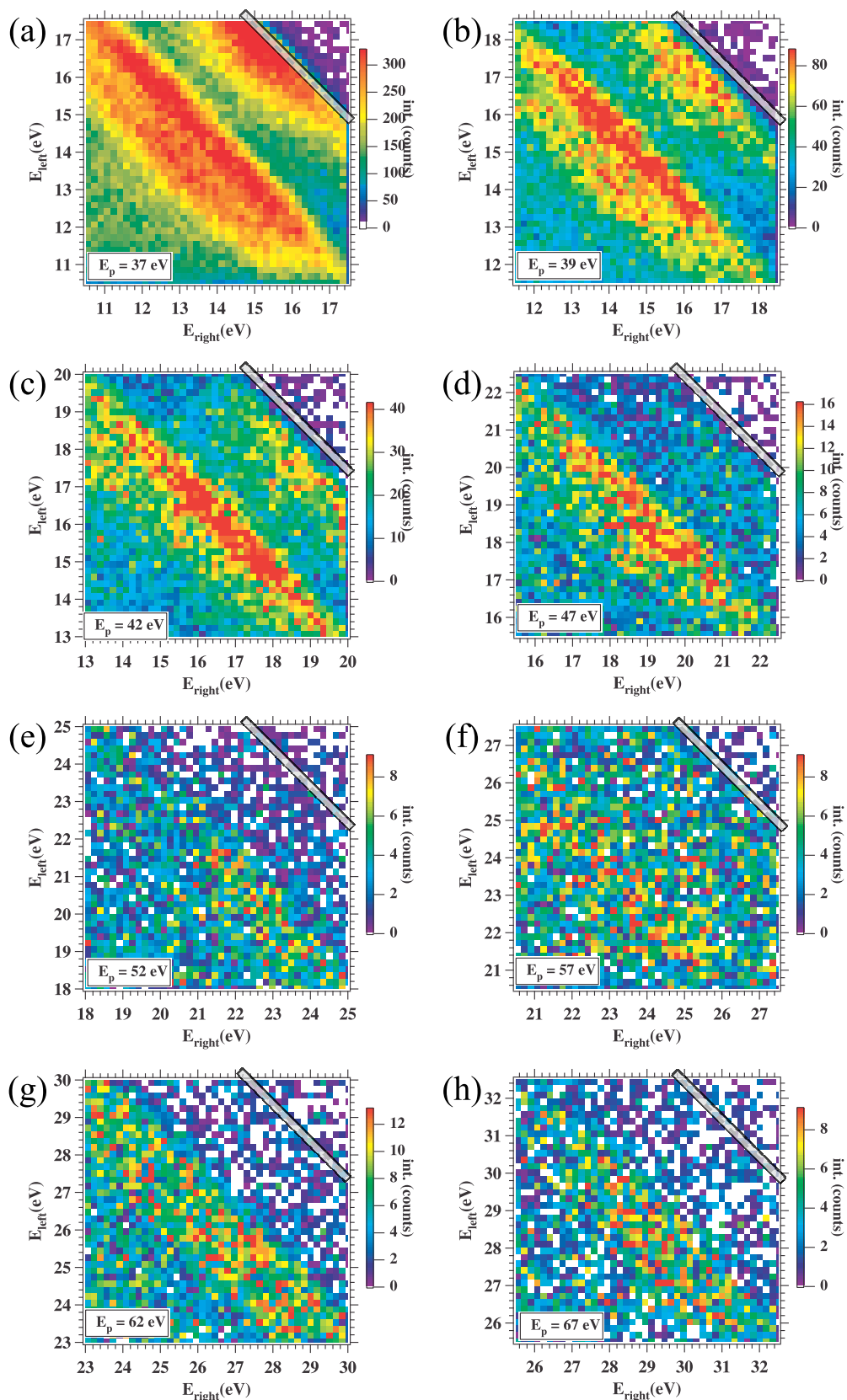


Figure 4.1 2D-energy spectra for different value of E_p . The primary energy increases from (a) to (h). The grey diagonal line marks the position of $E_{\text{sum}}^{\text{max}}$. The [001] direction of the Ag(100) sample was in the scattering plane. High-intensity regions parallel to the $E_{\text{sum}}^{\text{max}}$ -line are visible.

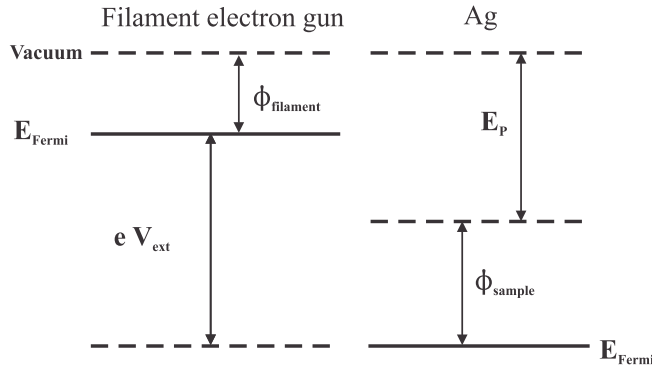


Figure 4.2 Energy levels of the electron gun filament and Ag.

In our experimental conditions, symmetrical alignment and normal incidence, the process that the incoming energy transfers the half of its energy to the valence electron is most favorable. The scattering process is mainly due to binary scattering, in which the total momentum is conserved. Furthermore, if the emission angles are equal and opposite to each other, the sum momentum $k_{\text{sum}}^{\parallel}$ is zero. The symmetric sharing distribution of the electron pair indicates that the pair creation is a single-step process. The incident electron beam undergoes specular reflections and the scattered electrons can generate electron pairs, as discussed in Ref. [95, 96]. Although a symmetric distribution is expected, the measured spectra look asymmetric due to the difficulty to orientate the primary beam and the lenses with each other.

Besides, the band parallel to the $E_{\text{sum}}^{\text{max}}$ line and close to the Fermi level, we observe a strong intensity band from 3 to 5 eV below $E_{\text{sum}}^{\text{max}}$. To interpret the sum energy spectrum serves the DOS of Ag(100) as first approximation. We do not expect to mimic the DOS, because this theory is concerned about a single state and we probe a two-electron state. However, the DOS contributes as input in the (e,2e) theory (see Sec. 2.6), where the initial state is a product of the LEED state of the primary electron and the Bloch state of the valence electron. The initial state is zero when no Bloch states are available. Consequently, the final state is also zero and no pair emission is observed.

As mentioned before (e,2e) is a surface sensitive technique. In previous comparison between theoretical and experimental (e,2e) data it was found out that the main contribution comes from the first two layers [97]. For this reason the layer resolved electronic band structure calculations are weighted as: 50 % surface, 30 % second layer and 20 % the other layers.

Electronic band structure of the 1st Brillouin zone was calculated by Jürgen Henk (MLU Halle). It was computed by state-of-the-art method [98]. The total band structure is shown in Fig. 4.3a. Furthermore, it is separated into the orbital characters d, p and s and is presented in Fig. 4.3b, 4.3c and 4.3d, respectively. The energy scale of theoretical data is not shifted according to experimental photo emission data, as done for Cu in Ref. [99]. It was not the scope of this work to calculate the shift.

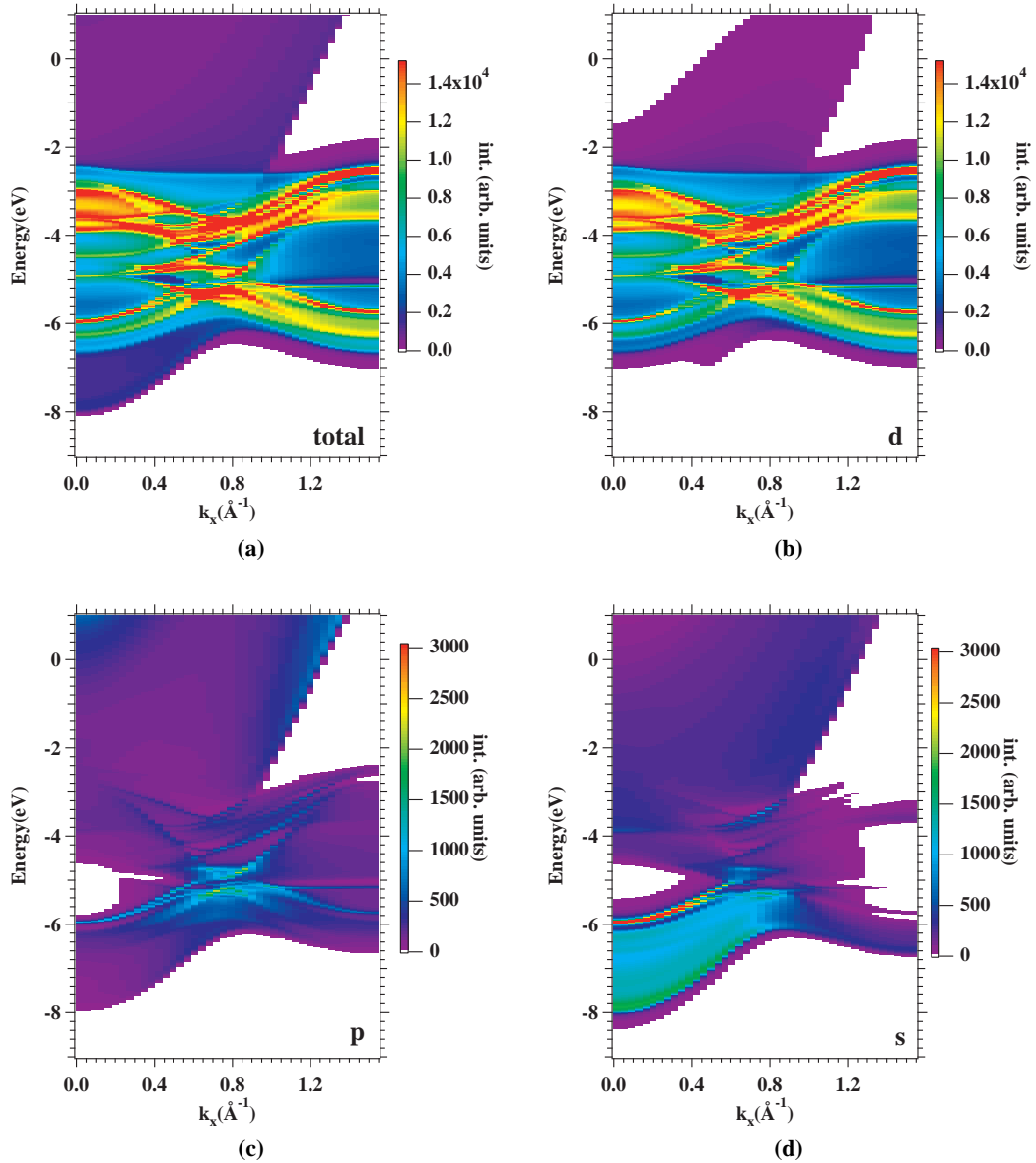


Figure 4.3 Band structure of Ag(100) using LDA theory for all orbitals (a) and resolved for d (b), p (c) and s (d) along $\Gamma - \Delta - X$ -direction. Shown is a cut through the 1st BZ. The calculations were performed by Jürgen Henk (MLU). The layers are weighted as follows: 50% surface, 30% second layer and 20% the underlying layers. Fermi energy E_F is at 0 eV.

Ag crystal has one electron in the sp state and 10 d electrons, so the main contribution comes from the d orbitals. The flat d bands contribute mainly in the energy region from 2.5 to 7 eV. In the region near the Fermi level ($E_F = 0$ eV) the intensity is below 5% of this value.

The p and s orbitals show less intensity over the hole distribution than the d electrons. The intensity scale of Fig. 4.3c and Fig. 4.3d were reduced to 20% of the total scale to see the features of the bands. Both spectra show parabolic distribution. The orbitals have constant intensity from the Fermi energy to 4 eV below it. A gap appears between 4.5 and 5.5 eV. Furthermore, we observe that the s orbital shows a strong intensity at 6 and 8 eV around the Γ point.

The band structure is integrated over the region, which is probed in the experiment ($k_x =$

0 – 0.4 Å⁻¹). It is convoluted with 0.5 eV Gaussian, appropriate for the experimental conditions. The contribution of the surface, the second layer and the weighted sum layers is shown in Fig. 4.4a, b, c. The DOS is presented for sp (dashed), d (grey) and total (black) orbitals, separately. The sp DOS is the sum of s and p orbital. Figure 4.4d shows an experimentally obtained sum energy spectrum for $E_p = 37$ eV ($E_{\text{right}} - E_{\text{left}} \leq 3$ eV).

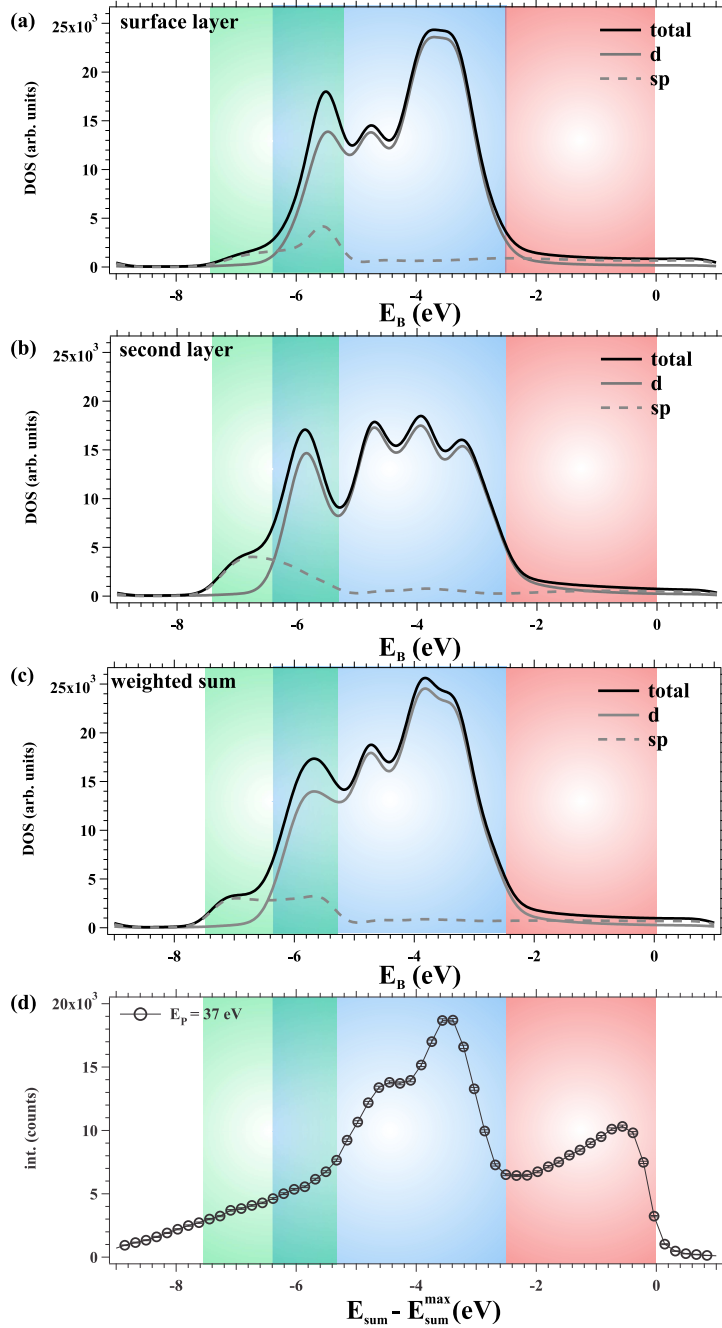


Figure 4.4 Calculated density of states (DOS) of Ag(100) is integrated over the angular acceptance of the experiment and convoluted with a 0.5 eV Gaussian. The surface layer (a), the second layer (b) and the weighted sum (c) are compared to an obtained spectrum at $E_p = 37$ eV. The DOS is orbital resolved: total orbital (black), d (grey) and sp (grey dotted). Furthermore, regions with special character are highlighted: the red area shows enhanced intensity in the experiment, in contrast to the DOS. The blue area is d dominated region. The green highlighted contribution has sp character. The turquoise area marks the overlapping of sp and d orbitals.

We label the regions with special attributes on basis of the weighted sum DOS and the sum energy spectrum. The first region from 0 to 2.5 eV is colored in red. The DOS is flat and low, including contributions from sp and d orbitals. But in the experiment a pronounced peak like structure with high intensity is observed. This supports that the DOS is far from sufficient to

explain (e,2e) results.

The next region from 2.5 to 6.4 eV is dominated by d orbitals and highlighted in blue and turquoise. DOS shows even in “experimental mode” features. However, in the experiment only one broad peak at 3.5 eV with a shoulder at 4.5 eV is recognized. This peaks could be connected to theoretical features at around 3.6 and 4.8 eV. The intensity of the experimental shoulder falls off to lower energies. The experimental decline of intensity is not smooth, but has a kink at 5.3 eV. The slope from 5.4 eV to around 8 eV decreases to 5% of the slope from 4.6 eV to 5.4 eV. The kink marks the border between the blue and turquoise region. When we look at the weighted sum DOS (Fig. 4.4c), it appears that the sp orbitals getting more pronounced at an energy of 5.3 eV, due to the strong contribution of the sp electrons in the surface layer (Fig. 4.4 a). Furthermore, at 5.8 eV appears a peak in the DOS which is completely missing in the experiment. This underlies again the need of (e,2e) theory to understand the spectra.

Continuing labeling the spectra, the contribution from the sp states increases at 5.2 eV to a plateau and decreases at 7.5 eV. This is highlighted in green. The overlapping area of green and blue region appears turquoise. Coincidentally, the overlapping border and the kink in the slope are at the same energy. In the surface layer the contribution of the isotropic sp orbital is 20 % of the total DOS at 5.5 eV.

To have a deeper understanding of the allowed transitions, we look at the symmetry resolved DOS in the [001] direction of the Ag(100) crystal along the Γ point as well. The data is presented for different layers and symmetries in Fig. 4.5. The spectra are convoluted with a 0.5 eV Gaussian. In Fig. 4.5a the same experimental data as in in Fig. 4.4d is shown for comparison. Four symmetries are separated; Δ_1 (Fig. 4.5f), Δ_2 (e), $\Delta_{2'}$ (d) and Δ_5 (c). In Fig. 4.5b the sum of all symmetries is depicted.

The main differences between the symmetries are the following: The Δ_1 representation is divided in two regions, one peak at 4 eV and one peak around 6 eV. The Δ_2 symmetry ranges from 2.2 to 5.2 eV. $\Delta_{2'}$ is spanned from 4.4 eV to 6.6 eV. The Δ_5 is located around 3.3 eV.

The same selection rules for the (e,2e) process have to be applied as reported in Ref. [100]. They showed that the $\Delta_{2'}$ transition is forbidden. In this case, the wave function of the valence electron is antisymmetric when it is mirrored at the reaction plane. So the resulting integral is zero. In contrast to the other wave functions, which are symmetric to the reaction plane.

Comparing the experimental data to the symmetry resolved DOS, we see that below 5.4 eV the $\Delta_{2'}$ and Δ_1 symmetries contribute to a theoretical peak. However, there is no peak in the experimental data. Due to the (e,2e) selection rules we expect no intensity from $\Delta_{2'}$ symmetry. The contribution in the region from 2.4 eV to 5.4 eV is formed by the Δ_2 and Δ_5 states. In this range in the experiment a peak and a shoulder show up.

Besides selection rules, so-called matrix element effects has to be considered. For example the primary energy of the incident electron influences the transition probability. In the presented data this effect is not included, because it is difficult to estimate.

We conclude, that the DOS does not resemble the coincidence spectra. The experimentally observed peak in the energy region from 0 eV to 2.4 eV is completely missing in the DOS. On the other hand is a peak calculated at 5.8 eV, which is not observed in the (e,e2) spectrum.

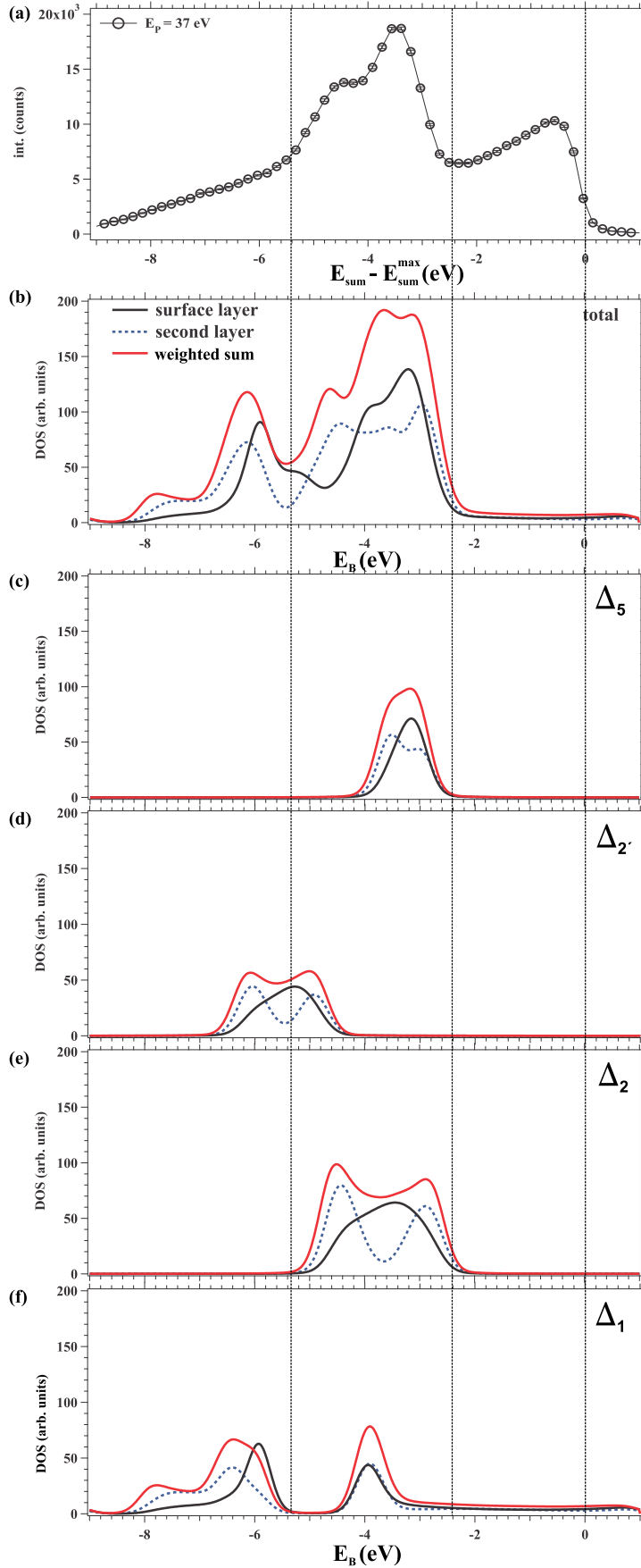


Figure 4.5 Calculated density of states (DOS) for Ag(100) at the Γ -point ($k_{\parallel} = 0$) and convoluted with a 0.5 eV wide Gaussian compared with the experimentally obtained sum energy spectrum (a). The symmetry points are layer resolved: surface layer (black), second layer (blue dotted) and weighted bulk layer (red). In (b) we see the total symmetry, (c) Δ_5 , (d) $\Delta_{2'}$, (e) Δ_2 and (f) Δ_1 . Selection rules prohibit $\Delta_{2'}$ transition in (e,2e).

4.1.2 Absolute Pair Emission

As we have the possibility to measure the primary flux, we can quantitatively analyze the intensity distribution of the pair emission as function of the primary energy E_p and analyze the absolute pair emission. In the (e,2e) experiment multiple scattering plays an important role, as for example in LEED-IV measurements. It is well known, that the LEED-IV intensity changes with primary energy. Therefore, we also expect variation in dependence of E_p .

We measure the integral coincidence intensity or rather sum up over all pairs emitted in the energy window. The energy window was adjusted to the primary energy (see Fig. 4.1). The maximum sum energy (indicated by the grey line) stays at the same position. The constant detection window makes it possible to directly compare the integral spectra, which is identical to the arrival time histograms. As examples arrival time histogram for $E_p = 37$ eV and $E_p = 52$ eV are presented (see Fig. 4.6a and Fig. 4.6b, respectively). From this data the true counts per second are calculated. The data was obtained in approximately 2 hours.

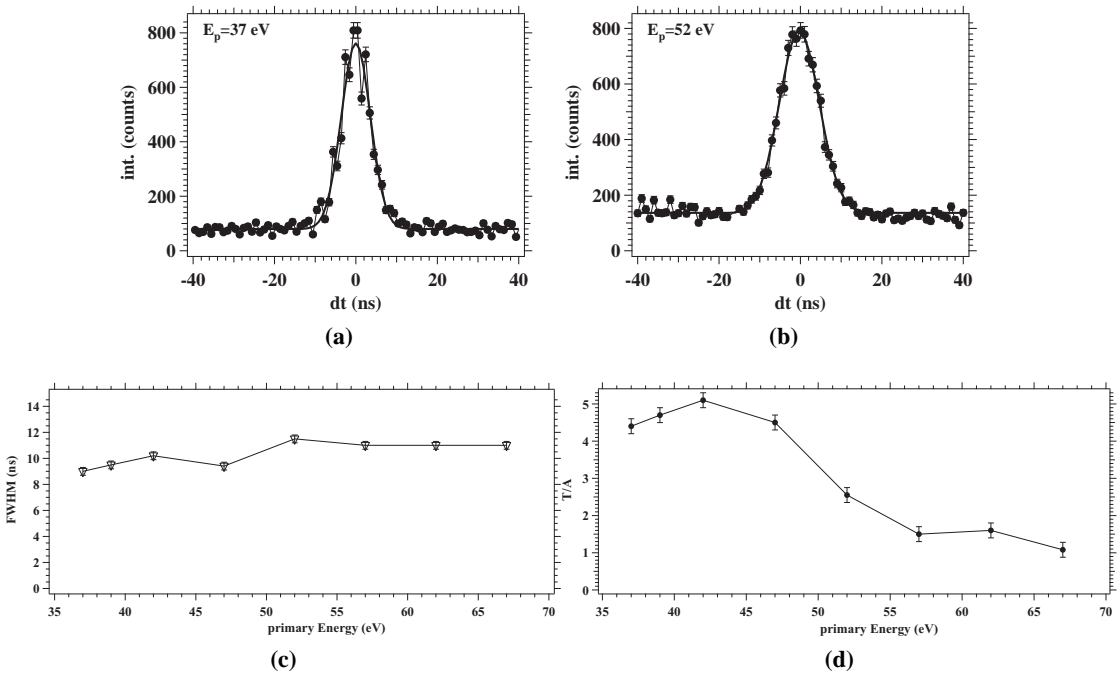


Figure 4.6 Arrival time histograms (a) at $E_p = 37$ eV and (b) $E_p = 52$ eV. For different primary energies FWHM of the peak ± 0.3 ns (c) is summarized and the ratio of the true and accidental counts $T/A \pm 0.2$ (d) is shown.

Besides the true counts the histogram was analyzed regarding the full width at half maximum (FWHM), counts on the rate meter, true counts, the ratio of true and accidental counts (T/A). The result is summarized in Fig. 4.6. The FWHM lies in the region between 9 and 11 ns, whereby the error of the width is calculated with 0.3 ns. The width determined by the flight time dispersion of the electrons in the hemispheres, as also theoretically calculated in p. 46.

The ratio T/A of the true and the accidental counts has a value about $4 - 5 \pm 0.2$ from $E_p = 37$

to 47 eV. Increasing the primary energy the ratio decreases. At 57 eV the ratio is 2. Increasing the energy further reduces the ratio to 1. It was not possible to keep the T/A ratio at 4 and acquire the spectrum in an appropriate time, because the true count rate decreases. That is understood mainly by simple geometric arguments. With higher primary energy, more possibilities of energy sharing between the pairs exist, but still the same energy region near E_F is probed. Consequently, less pairs are detected. Another factor influencing the true count rate, is the cross section. The reason might be that for higher primary energy the electrons are faster, which means that the interaction time with the environment decreases. Furthermore, the reflectivity of the elastically scattered electrons decreases (see Fig. 2.4a). Hence the pair emission decreases.

By measuring the integral spectra and the primary electron flux with the flux meter, the coincidence counts per primary electron is calculated by dividing the true counts by the primary electron flux. On average 1×10^8 primary electrons are necessary to detect one true pair. The results are plotted as function of the primary energy in Fig. 4.7, represented by black dots. First we notice, that the coincidence rate is not monotonic as function of the primary energy. At 30 eV primary energy 4.3×10^{-7} coin/e⁻ are detected. At 37 and 39 eV the pairs are decreased to around 3×10^{-7} coin/e⁻. At 42 eV the coincidence rate increased up to 6×10^{-7} coin/e⁻. Then at 47 eV the rate decrease to 1.5×10^{-7} coin/e⁻, which is 25% of the 42 eV value. The next point 52 eV increases to 3×10^{-7} coin/e⁻ comparable to the 37/39 eV point. The energies 57, 62 and 67 eV show very low values around 0.3×10^{-7} coin/e⁻.

Now, we combine the absolute count rate and the energy resolved spectra. First, all counts of the 2D spectrum are summed up; the result is divided over each point in the 2D spectrum. Each point is then multiplied with the total absolute coincidence rate per primary electron (we assume that all regions are modulated equally by the primary flux). Finally, the absolute sum energy spectra are obtained for each primary energy (see Fig. 4.8). The intensity from spectra 57, 62 and 67 eV are multiplied by a factor of 10. The trend of the intensity variations of the spectra reflects the graph Fig. 4.7.

Besides, that the absolute intensity changes, also the different partial distributions vary. For example, for $E_p = 37$ eV the sp peak intensity from 0 to 2 eV is the half of the d contribution. Going to 42 eV we see that the sp-intensity increases only slightly, in contrast to d, where the peak height is almost 3 times the sp height. The absolute integral intensity for sp from 0 to 2 eV and the purely d electrons from 2 to 5.4 eV is splitted according to Fig. 4.4. The result is summarized in Fig. 4.7. The sp (red) and the d (blue) partial intensities follow the trend of the total counts in general. For the d contribution this is more prominent, because more counts are covered. A difference between sp and d is that at $E_p = 52$ eV for the total coincidences a peak appears as well as for d alone, but the peak is missing for sp. But both orbital contribution change with primary energy.

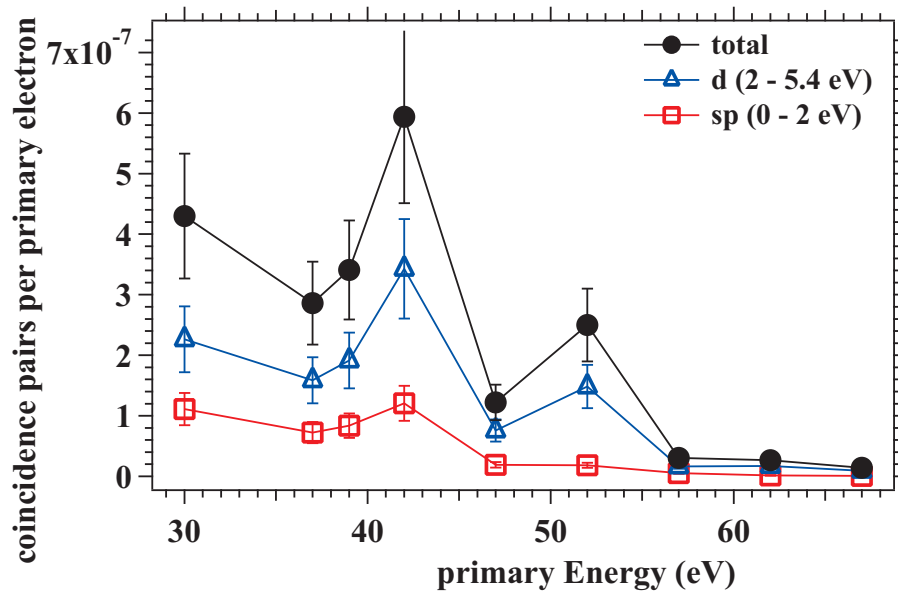


Figure 4.7 Absolute coincidence pair intensity in dependence of the primary energy E_p for Ag (●) and split up for the different orbital regions s (□) and d (△), according to Fig. 4.4.

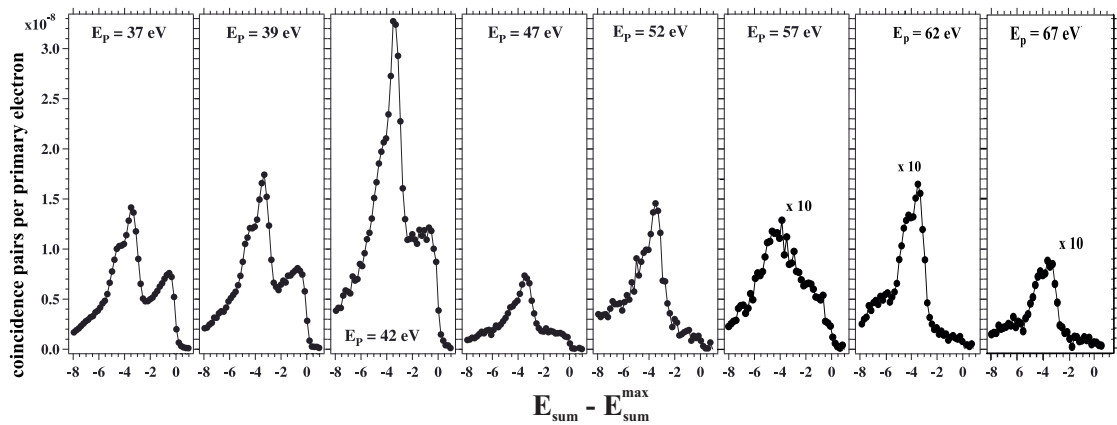


Figure 4.8 Experimental spectra normalized to coincidence counts per primary electrons for primary energies from 37 to 67 eV.

4.1.3 Diffraction Effects

We identified contributions of the sp and d orbitals in the sum energy spectra. Large intensity variations of the bands were observed with primary energy change. We want to shed light into this phenomena. (e,2e) is a multiple scattering experiment, so diffraction play a role. Wei *et al.* [31] report about similar intensity variation on Cu(100). They studied (e,2e) spectra for different primary energies in the same energy range as here. They calculated the relative intensity of the partial electron states and made relation to kinematic Bragg diffraction. The model is applied to Ag(100) and the validity will be discussed.

To quantify the intensity variations of the bands, the relative spectral contribution RSC in dependence of the primary energy E_p is introduced

$$RSC_{\text{band}}(E_p) = \frac{I_{\text{band}}}{I_{\text{total}}} . \quad (4.1)$$

As an example, the sum energy spectra for 37 eV and 52 eV are shown in Fig. 4.9, sp (d) dominated region is colored in red (blue). The y-scale represents the measured counts. The spectrum at $E_p = 37$ eV was obtained for around 3.5 eV. The peak at 3.7 eV collected 20×10^3 counts and the statistic is very good. The spectrum at 52 eV was obtained in 100 min and at 3.7 eV, 300 counts are collected. The statistic is still acceptable and trustful. The sum energy spectra are obtained in the range of $E_{\text{right}} - E_{\text{left}} \leq 3$ eV to integrate over the same area for all energies and rule out intensity variation artefacts.

The I_{band} is the integrated intensity of the sum spectrum of the interested orbital band. I_{total} refers to the intensity integration of the whole spectrum, whereby only values below 0 eV are considered ($E_{\text{sum}} - E_{\text{sum}}^{\text{max}} \leq 0$).

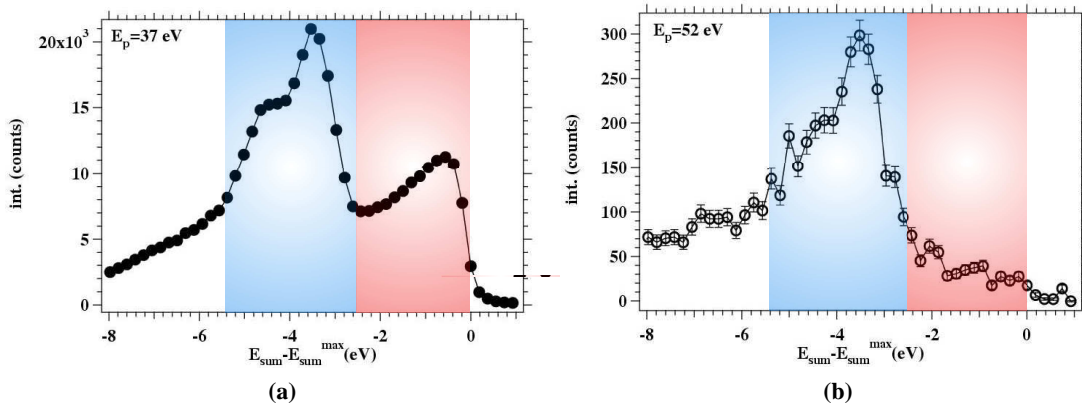


Figure 4.9 Sum energy spectra for (a) $E_p = 37$ eV and (a) $E_p = 52$ eV. The orbital characters sp and d are highlighted with red and blue boxes, respectively.

The results of the relative spectral contribution in dependence of the primary energy are presented in Fig. 4.10. The primary flux dependence cancels by calculating the intensity ratio. The red empty squares represent the sp orbitals and the empty blue triangles show the d orbitals.

Firstly one notices, that the sp part shows variations, from 6% up to 29%. In contrast to the d part where the contribution fluctuates from 30% to 40%. At the lowest energy $E_p = 30$ eV both share around the same amount of 29% (30%) for sp (d). The general trend for d is linear increasement of the contribution up to 40% at 67 eV. The only irregularity is a small intensity drop at 57 eV down to 32%.

The development of the sp can be described as follows: From 30 to 42 eV the contribution has a constant value of about 29%. Then a rapid decrease begins and ends at 8% for 52 eV. Aferwards a kink appears at 57 eV and the *RSC* raises to 22%. At 62 eV the contribution is decreased to 6% and stays around this value at 67 eV.

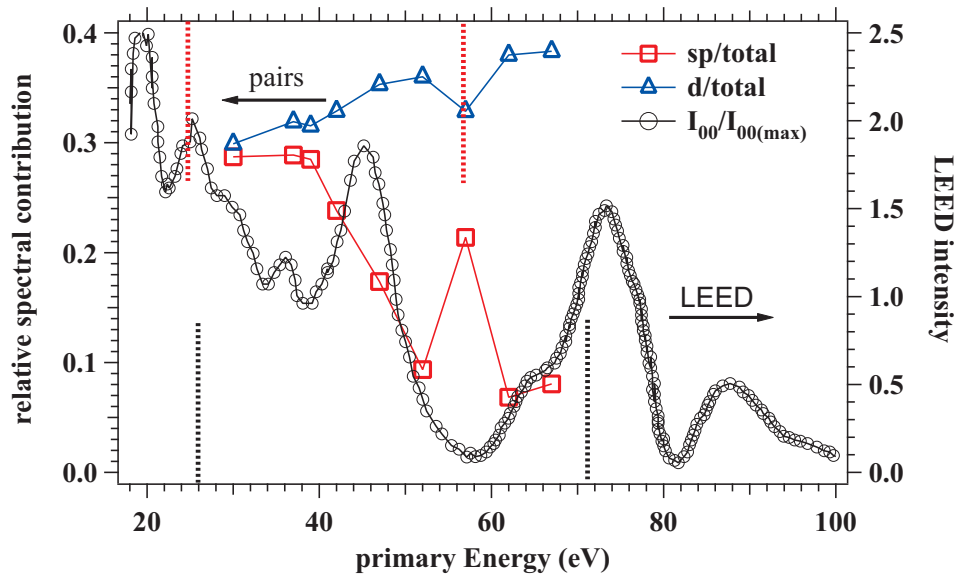


Figure 4.10 The relative spectral contribution as function of the primary energy for sp (\square) and d (\triangle) contribution. This is compared with the LEED-*IV* curve of the (0,0) beam from a Ag(100) surface [101]. The dashed lines indicate the Bragg peaks of the kinematic model for pairs (red) and single electrons (black), respectively.

The recent (e,2e) theory describes the incoming primary electrons by LEED states and the outgoing pair by a time reversed LEED state [29, 81]. This formalism emphasizes the diffraction in the (e,2e) process. The diffraction takes place in-plane to the surface.

Before handling the pair, we remind the single diffraction of energetic low electrons, which impinge normal on the surface. The simplest case is that the incoming electrons are just once weakly scattered by the ion core potential and reflected back out of the surface. This approach is called the kinematic model. If the wavelength λ of the electron is equal to twice the lattice plane distance, d , constructive interference appears.

This is known as the Bragg conditions for normal incidence

$$n\lambda = 2d \sin \theta, \quad n = 1, 2, 3 \dots \quad (4.2)$$

Destructive interference appears when $n = 1/2, 3/2, \dots$

The primary energy E_p^{00} for which the electrons interfere are then the following

$$E_p^{00} = \frac{n^2 h^2}{8md^2} - V_0, \quad n = 1, 2, 3 \dots \quad (4.3)$$

The electron gains energy from the inner potential V_0 when entering the surface. In this equation the absolute value of V_0 is considered. The inner potential of Ag is around 10 eV. The electron mass and Planck's constant are given by m and h , respectively. The lattice plane distance is d ($d_{Ag} = 2.02 \text{ \AA}$).

The kinematic model can be also applied for pairs, whereby the pair is treated as one particle with defined sum energy and sum momentum. The maximum available energy of the pair is reduced by the amount of the work function Φ . Compared to the single case, we get $E_{sum}^{max} = E_p - \Phi$. (The equation is valid, when the electrons come from valence states near E_F .) The Bragg condition for the pair needs to be found. In other words, at which wavelength interference will occur for the pair. The changeable parameters of Eq. (4.3) are the inner potential V_0 and the mass m . We assume the double values of V_0 and m as in the single case.

This leads to the following available energy for the pair

$$(E_p - \Phi) + 2V_0 = \frac{\hbar^2}{2(2m)} \mathbf{k}_{sum}^2 \quad (4.4)$$

The k_{sum} term consists of the parallel part k_p^{\parallel} and the normal part k_{\perp} . Just the last one has to be taken into account, because $k_p^{\parallel} \approx 0$. For the k_{\perp} direction the inference conditions (see Eq. 4.2) has to be applied. Consequently, we get $n\lambda_{\perp} = n\frac{2\pi}{k_{\perp}} = 2d$ and the primary energy is

$$E_p = \frac{n^2 h^2}{16md^2} - 2V_0 + \Phi, \quad n = 1, 2, 3 \dots \quad (4.5)$$

This equation can be rearranged by using Eq. (4.3) and expressed more generally for electrons from other valence band positions, which have the additional energy E_{vb} ,

$$E_p = \frac{1}{2}E_p^{00} - \frac{3}{2}V_0 + \phi + E_{vb} \quad (4.6)$$

The primary energy values for the single E_p^{00} and pair E_p case are calculated and summarized in Tab. 4.1. (The first order give negative energy values, which means that the diffraction occurs inside the solid and cannot be observed outside.) In Fig. 4.10 the Bragg peaks are inserted for single electron diffraction (black lines) and pair diffraction (red lines) for $E_{vb} = 0 \text{ eV}$. The single kinematic model was introduced to explain the LEED-IV intensity variations. The LEED-IV curve of the (0,0) beam (taken from [101]) is included in Fig. 4.10. The (0,0) beam is the one most likely comparable with the pair diffraction, because the momentum of the electrons of the pair is in opposite direction with equal amount and they add up to 0. The kinematic scattering (single Bragg) could explain the enhancement at 26 and 76 eV. The peak at 42 eV seems to be due to multiple scattering, described in a more elaborated dynamical theory, which will not be considered here. Nevertheless, it is interesting to mention, that the absolute sum energy

Table 4.1 Calculated Bragg peaks for the (0,0) beam from the Ag(100) surface in kinematic approximation ($E_{vb}=0$). Pair electron diffraction peaks are E_p and single diffraction peaks are E_p^{00} .

order	E_p (eV)	E_p^{00} (eV)
1	-10.9	-1.0
2	2.6	26.0
3	25.1	70.9
4	56.5	133.0

spectrum (Fig. 4.7) is enhanced at this energy. This means the incoming beam is reflected with a high probability and ejects another electron.

The Ag(100) LEED-*IV* curve does not resemble the $RSC(sp)$ curve as it is observed for Cu(100) [31]. In the present scenario for example the LEED-*IV* curve shows a minimum at 59 eV, while the $RSC(sp)$ curve shows a peak. This is easily understandable in the sense that a low LEED intensity means high absorption and high probability to transfer energy to valence electrons, consequently higher pair emission is expected.

One pair electron Bragg peak is calculated for $E_{vb} = 0$ for sp orbitals at an energy of 56.5 eV. At $E_p = 57$ eV a peak appears in the RSC_{sp} plot. Experiment and model match at this point. However, we have to take into account, that the peak consists of just one data point.

Another peak is expected at 25 eV. Indeed, higher intensity is observed at $E_p = 30$ eV. Unfortunately, data at lower primary energies is missing. Actually, the data situation is not strong enough to prove the validity of the diffraction model.

The RSC_d curve is almost constant, compared to the RSC_{sp} orbital. Theoretically for d the diffraction peaks would be shifted around $E_{vb} \approx 4$ eV to higher values. Accordingly a peak would be expected at 29 and 60 eV. At $E_p = 30$ eV the intensity is lowest, in contrary to the expectation. The same behaviour happens at $E_p = 59$ eV, where a small intensity drop is observed. Concluding, the d-band does not follow the prediction of the model. Obviously, the orbital character plays a role. This would support also the variations of the sp-band. The sp-band scatters isotropically and the kinematic model is constructed within the effective plane wave model.

To understand the experimental results better, support from the (e,2e) theory is needed. Calculations are very time and resource consuming. Hence no theoretical results are available. When the primary electron is diffracted before interaction, one would expect that the relative intensity variations for s and d orbital are the same. When the outgoing pair is diffracted itself different behavior of each orbital character seems reasonable to observe.

The question, which possibility is more probable was discussed in the past. The first time diffraction of the scattered “two-electron quasi particle” was observed by Berakdar *et al.* [102] on Cu(100) with a time-of-flight experiment. They fixed the incident energy E_p and analyzed the energy sharing. They observed, that the major contribution originates from the pair back reflected from the crystal potential. Samarin *et al.* [103] also study the Bragg diffraction of the electron pair. They demonstrate that it is appropriate to consider the electron as a pair rather than

as individual electrons. When the interaction of the electrons is neglected, then the diffraction is reduced to diffraction of individual electrons. In both experiments they analyzed the cross section in dependence of the the parallel momentum k_{\parallel}^x . In our experiment we observe that the sum pair $k_{\text{p}}^{\parallel} = 0$. Also in their experiment they observe at $k_{\text{p}}^{\parallel} = 0$ a finite intensity.

To conclude, strong dependence of the primary electron energy on the partial distribution of the spectra are found. Connection to diffraction effects seems to be reasonable, but is not be confirmed because of lack of experimental data and theoretical calculations.

4.2 (e,2e) on NiO/Ag(100)

A key motivation of this work is to explore the coincidence intensity as function of the model parameter U , which is a parameter for strength of the electron correlation. For this purpose we choose materials with obviously different correlation strength. In the previous chapter we studied in detail a Ag(100) crystal, U is close to 0. Hence the electronic structure can be explained within the effective potential picture. In contrast to transition metal oxides (TMO) as NiO, which need a more elaborated model to describe the electronic structure. In the model a U of 8 eV is incorporated for a proper characterization.

We compare the coincidence intensity of both materials. We can measure both materials in the same experimental run, because NiO film grow well on Ag(100). NiO and Ag have only a lattice mismatch of 2% and the growth of NiO on Ag(100) is well established (see Sec. 3.3). The acceleration voltage of the primary electron was fixed at 32 V, as was the primary flux. The primary energy changes according to the surface under study to $E_p(\text{Ag}) = 30$ eV and $E_p(\text{NiO}) = 31.6$ eV. The analyzers and lens settings were set to probe the same energy window. The integral spectrum for both materials have been obtained under essentially the same conditions for the data acquisition time of 19 h (see Fig. 4.11).

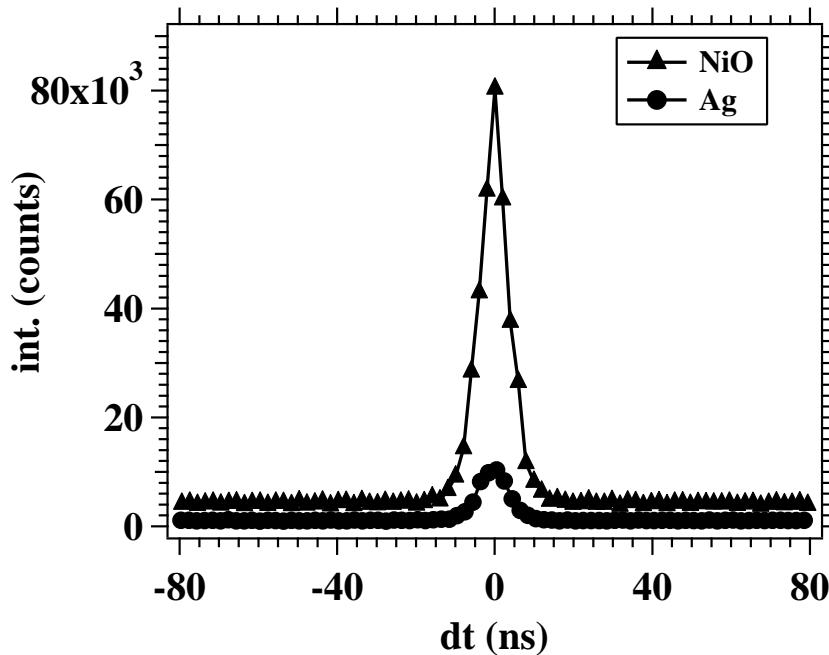


Figure 4.11 Arrival time difference spectrum obtained from a Ag(100) surface (●) and a 15 ML NiO/Ag(100) film (▲). The acceleration voltage of the primary beam was kept constant at 32 V. Due to variations of the work function and positions of the chemical potential the primary energy is $E_p = 30$ eV for Ag(100) and $E_p = 31.6$ eV for NiO/Ag(100). The data acquisition for both experiments was 19 h and the primary flux was constant. The peak in the spectrum is the signature of *true* coincidences. The width of the peak reflects the time resolution of the instrument. Taken from Ref. [68].

The graph shows the counts in dependence of the arrival time difference. Both distributions display a peak centered at $dt \approx 0$ ns. The width of the peaks is in both instances approximately 10 ns which reflects the time resolution of the experiment. The emergence of a peak is a clear proof of *true* coincidences. These events stem from the impact of one primary electron. Within the time resolution of the experiment these correlated electrons leave the sample at the same time and hence are detected at the same time. The intensity outside the peak region is due to *random* coincidences. These events are caused by the impact of two primary electrons within the time window of the coincidence circuit (100 ns in our case). Therefore the dt -spectrum gives us immediately the ratio of *true* to *random* coincidences. The key observation is a significantly higher intensity peak for NiO (\blacktriangle) compared to Ag (\bullet). For NiO the peak reach its maximum at 80×10^3 counts and for Ag the maximum is at 10×10^3 counts. NiO peak height is a factor of 8 higher compared to Ag in this example. The ratio of *true* to *random* coincidences is 8.5 for NiO compared to 4.7 for Ag.

We conclude that the pair emission from a material described with a $U = 8$ eV is significantly increased compared to a material with $U \approx 0$. This supports the view that the statements made about the DPE-intensity versus U can be at least qualitatively extended to an (e,2e) process.

An important question is whether the enhanced coincidence intensity from NiO is a genuine effect and not a consequence of the finite angular acceptance of the instrument. It is conceivable that the integrated coincidence intensity from Ag(100) and NiO(100) shows no significant variation, but that the angular distributions are different such that most of the pairs from the Ag(100) surface are not within the field of view of the apparatus, as illustrated in Fig. 4.12a. The figure shows schematically the possible emission of Ag and NiO and the angular acceptance of the Scienta set-up. NiO electrons are colored in grey and show the most probable emission in direction of the Scienta detectors. For Ag (blue) the emission angle between the pair could be smaller, consequently not all electrons would be caught by the detector, resulting in a wrong interpretation of the data. In order to rule out this aspect, a system with higher acceptance angle was employed, namely a TOF spectrometer [104, 105, 106]. The acceptance angle is indicated in Fig 4.12a by a dotted circle. Additionally, this instrument is equipped with a channel plate detector to measure the low primary flux (of the order 10^{-15} A) in absolute units. In addition to NiO, other oxides containing Fe, Cr and V were studied and compared to the pure metals. The structural order and exact chemical state requires further studies, but there is already a clear picture emerging, see Fig. 4.12b. Making use of the possibility to measure the primary flux we quote the coincidence intensity as electron pair per incoming primary electron. We consider all pairs within the angular acceptance and integrate over all energies and plot the pairs in dependence of the primary energy from 18 to 28 eV for pure Ni (filled square) and NiO (filled circle). The other metals (open square) and corresponding oxides (open circle) are measured at $E_p = 22$ eV and summarized to two data points. The fluctuations are symbolized by an error bar.

The NiO pair intensity is one order of magnitude higher compared to Ni. The coincidence intensity of the other oxides is enhanced about a factor of 5 compared to the pure metals. Reasoning the increased intensity of the oxides to the metals is an intrinsic effect and not the result of ex-

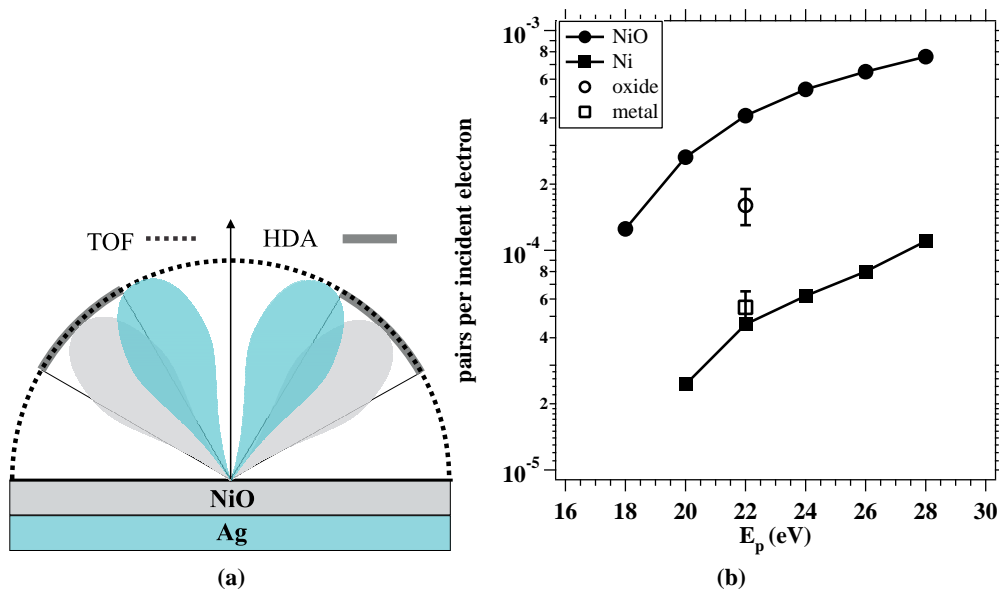


Figure 4.12 (a) Possible exaggerated emission angles of Ag (blue) and NiO (grey) electrons and experimental angle resolution of the TOF instrument (dashed line) and HDA set-up (continuous line). (b) Coincidence intensity measured as electron pair per incoming primary electron. Full circles and squares are the result for NiO and Ni, respectively. The result for Fe, Cr and V oxides and metal phase have been grouped together and are labeled with the open circles and squares. They indicate the average value while the error bars refer to the variance. The data is taken from Ref. [68].

perimental artifact.

The high count rate of NiO allows us to study the system in more detail in an appropriate time. First, we analyze the distribution of the pair in dependence of the primary energy and connected to the theoretical DOS. Furthermore the coincidence intensity of different film thicknesses and as function of the temperature is shown.

4.2.1 Energy Dependence

To study the energy dependence, a 15 ML thick NiO was grown on Ag(100). Therefore, pairs emerging from Ag can be excluded. The energy was varied from $E_p = 22.6$ to 68.6 eV.

The primary energy values are calculated as follows. In principle, it is similar to Ag. The difference is, that NiO is an insulator - the Fermi level lies in between the valence band and the conduction band. For convenience we calculate all energies with respect to the Fermi level, we set the Fermi level to 0 eV. The energy gap is $E_{\text{gap}} = 4$ eV and the work function is $\phi_{\text{sample}} = 5$ eV. Whereby the work function can be written as $\phi_{\text{sample}} = a + E_{\text{gap}}/2$ (see Fig. 4.13).

The primary energy E_p and the maximum sum energy $E_{\text{sum}}^{\text{max}}$ are therefore calculated as follows

$$\begin{aligned} E_p &= \phi_{\text{fila}} + eV_{\text{ext}} - a & (4.7) \\ E_{\text{sum}}^{\text{max}} &= E_p - \phi_{\text{sample}} \\ E_{\text{sum}}^{\text{max}} &= \phi_{\text{fila}} + eV_{\text{ext}} - a - \phi_{\text{sample}}. \end{aligned}$$

For example $V_{\text{ext}} = 32$ eV results in $E_p = 31.6$ eV. $E_{\text{sum}}^{\text{max}}$ is 26.6 eV, accordingly.

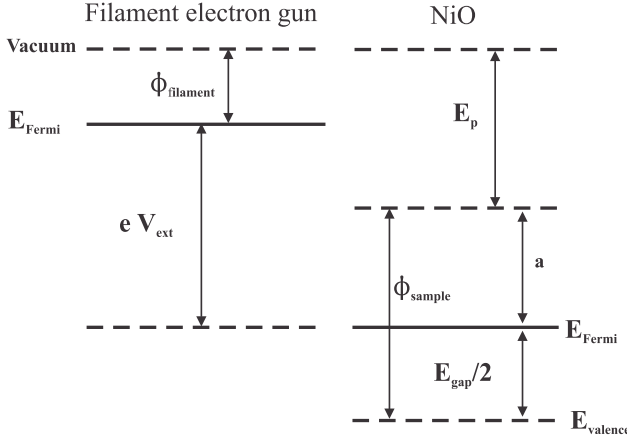


Figure 4.13 Energy levels of the electron gun and NiO.

In Fig. 4.14a a 2D energy spectrum from a 15 ML NiO/Ag(100) film for $E_p = 31.6$ eV is shown. As calculated a clear cut-off intensity is seen at $E_{\text{sum}}^{\text{max}} = 26.6$ eV and indicated with a black line. Further on below this line we see a diagonal band which suggests the relevance of valence states of particular binding energies. This band has an extension parallel to the $E_{\text{sum}}^{\text{max}}$ line of 2.8 eV and perpendicular to it of 1.4 eV (labeled as A).

However, most of the intensity is centered at around the position ($E_{\text{right}} = 12$ eV, $E_{\text{left}} = 12$ eV) and no prominent diagonal lines like in the case of Ag(100) (see Fig. 4.1a) are visible. The width of the blob parallel to $E_{\text{sum}}^{\text{max}}$ is around 8.4 eV and perpendicular to it about 2.8 eV wide (labeled as B).

To evaluate the extension of the intensity of equal energy sharing the sum energy plot is obtained for $|E_{\text{right}} - E_{\text{left}}| \leq 2$ eV as indicated by the dashed diagonal lines, Fig. 4.14b. As expected no clear peak is visible, instead two shoulder like features appear at 1 eV below E_F and around 4 eV. At lower energies a constant background tail follows with the same intensity as the peak A.

We use the band structure calculation (see Fig. 2.16b) and compute the DOS as a function of the binding energy and compare this with the E_{sum} spectrum. The geometry of the experiment and the almost equal energy of the emitted electrons set the kinematic accessible part of a region in the Brillouin zone around the Γ -point within $\pm 0.4 \text{ \AA}^{-1}$. Furthermore, we employ a Gaussian broadening of 0.5 eV to account for the energy resolution. The DOS is presented in Fig. 4.14c. Note, however, because of the weak dispersion, the influence of the kinematic restricted region for the k -point sampling in the BZ is not very strong. Upon the sampling we observe that the

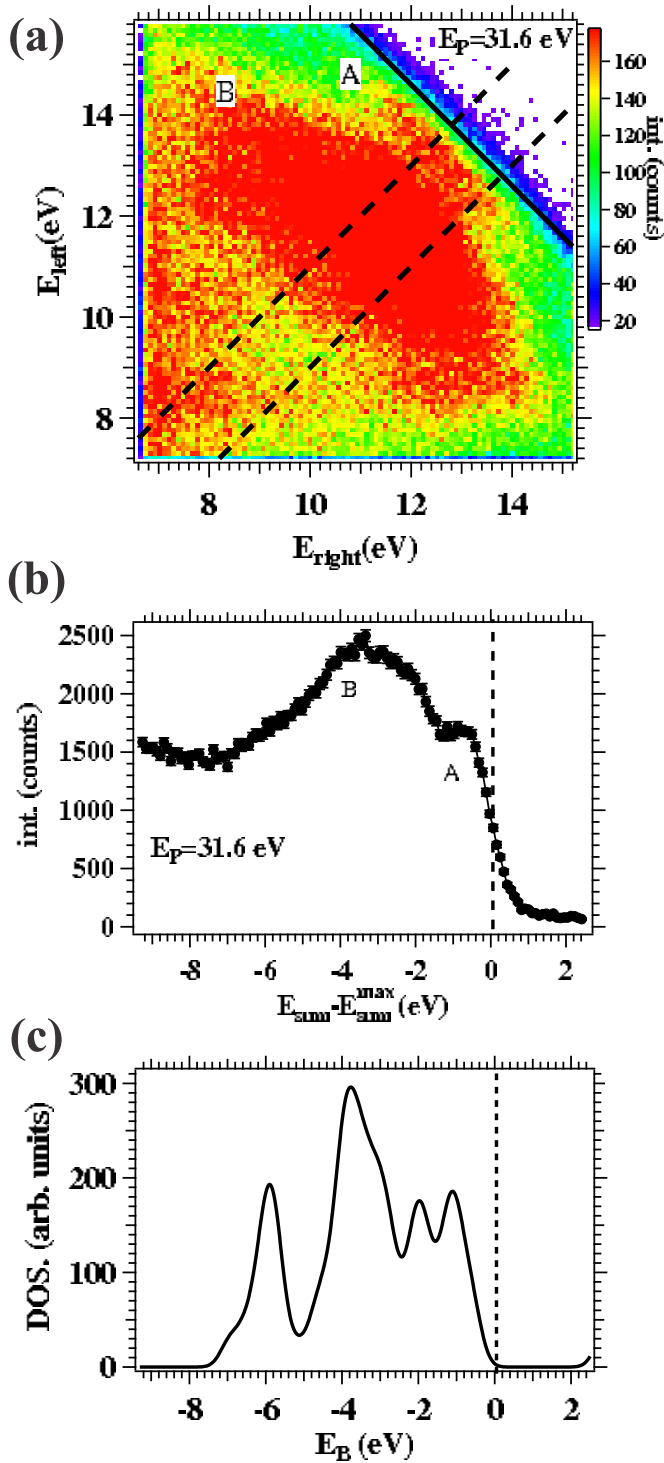


Figure 4.14 Energy spectra from a 15 ML NiO/Ag(100) film excited with $E_p = 31.6 \text{ eV}$. (a) 2D-energy spectrum, where the solid diagonal line marks the position of $E_{\text{sum}}^{\text{max}}$. The two dashed diagonal lines indicate the constraint $|E_{\text{left}} - E_{\text{right}}| \leq 2 \text{ eV}$ which has been used to compute the E_{sum} spectrum in panel (b). The energy $E_{\text{sum}}^{\text{max}}$ is indicated by a vertical dashed line. (c) For comparison we have included the calculated DOS spectrum (Fig. 2.16b) obtained after integration over the kinematical accessible part of the Brillouin zone. Further, we convoluted this with a Gaussian of 0.5 eV width to take into account the experimental energy resolution. Taken from Ref. [68].

binding energy spectrum still displays well separated peaks despite the broadening.

This is in contrast to the E_{sum} spectrum plotted in Fig. 4.14b where only two broad features (labeled A and B) are visible. The sum energy spectrum is significantly wider. The background pair emission intensity at lower energies originates from inelastic multiple scattering processes. These events are not described by band structure calculations and require separate analysis.

For different primary energies the 2D energy sharing distribution is measured and shown in Fig. 4.15. The black line indicates the maximum sum energy of the electron pair. For all energies we see elliptical intensity distribution, the long side is parallel to $E_{\text{sum}}^{\text{max}}$. In the majority cases intensities 4 eV below $E_{\text{sum}}^{\text{max}}$ dominate the spectrum. As discussed before this intensity is associated with d band electrons. However, for the lowest measured energy $E_p = 22.6$ eV (Fig. 4.15a) intensity 1 eV below $E_{\text{sum}}^{\text{max}}$ belonging to sp electrons are more prominent than the d blob. The s band has an extension of 5.6 eV parallel to $E_{\text{sum}}^{\text{max}}$, which is the double size as for $E_p = 31.6$ eV (presented here again in Fig. 4.15c). The dimension normal to $E_{\text{sum}}^{\text{max}}$ is 1.4 eV for both primary energies. Furthermore, the d blob for $E_p = 22.6$ eV has a smaller extension of 3.5 eV parallel to $E_{\text{sum}}^{\text{max}}$ compared with the 8.4 eV blob for $E_p = 31.6$ eV. Normal to $E_{\text{sum}}^{\text{max}}$ the dimension is 2.1 to 2.8 eV.

The spectrum obtained with $E_p = 26.6$ eV (Fig. 4.15b) shows a broadening of the s band parallel to $E_{\text{sum}}^{\text{max}}$ of 4.2 eV and perpendicular to it has also a value of 1.4 eV. The width of the d band is parallel 4.6 eV and perpendicular 2.1 eV.

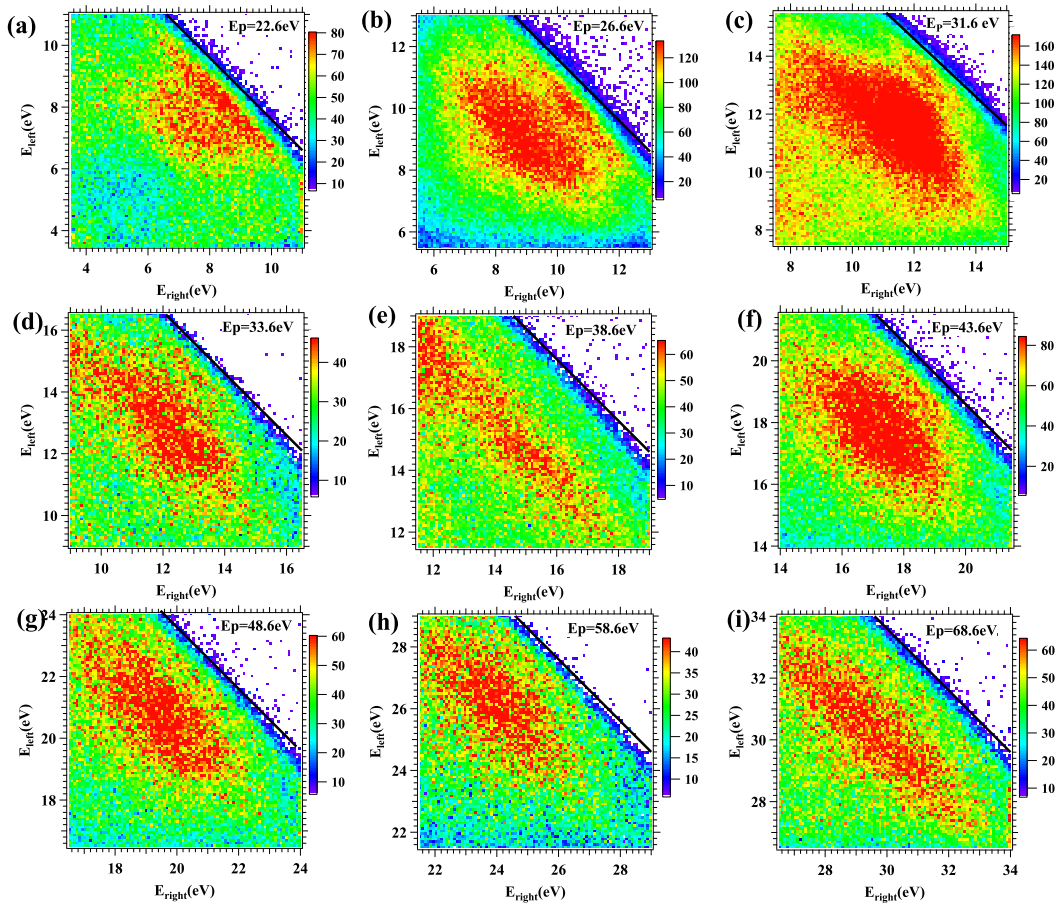


Figure 4.15 2D energy spectra of a 15 ML NiO/Ag film for primary energies from 22.6 to 68.6 eV (panel (a)-(i)). The black line indicates the maximum sum energy $E_{\text{sum}}^{\text{max}}$. The color scale indicates the intensity in counts.

The extension parallel to $E_{\text{sum}}^{\text{max}}$ gives information about the energy sharing of the electron pair.

The sum energy E_{sum} is constant. In the middle of the spectra both electrons carry the same energy and the difference between them is 0. In the 2D energy spectra (Fig. 4.15) we see that the highest intensity yields from this conditions. Coulomb interaction is the driving factor for this result. If Coulomb interaction would be neglected, an intensity minimum would appear. For $E_p = 31.6$ eV the difference between both d electrons are 8 eV and for $E_p = 22.6$ eV the energy difference is only 2 eV.

The 2D energy distributions above $E_p = 31.6$ eV vary just slightly with changing primary energy. Looking at the sum energy spectra for selected energies, obtained in the same fashion as in Fig. 4.14, the observation is confirmed. The spectra for $E_p = 22.6, 26.6, 31.6, 48.6$ and 68.6 eV are presented in Fig. 4.16. The spectra of 22.6 and 26.6 eV are colored in grey, because the “A peak” is more prominent compared to the “B peak”. The spectra above $E_p = 31.6$ eV are colored in black and show among each other no difference. This indicates, that we study the initial state of the system. Different exciting conditions give the same result.

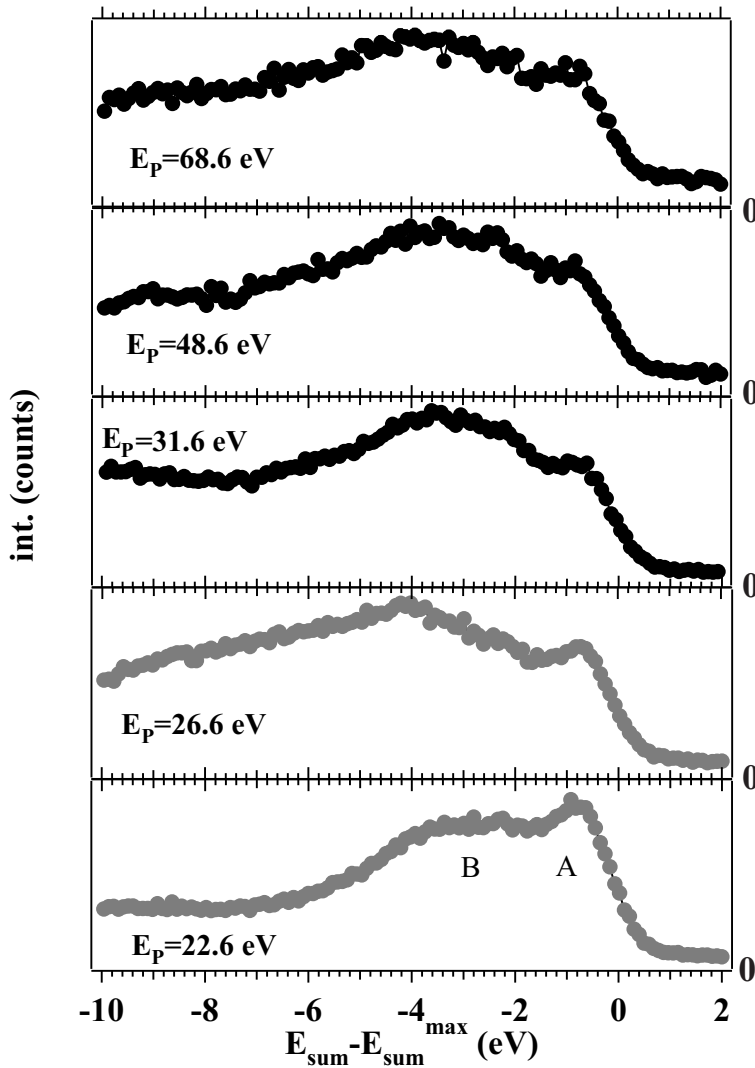


Figure 4.16 Sum energy spectra ($|E_{\text{left}} - E_{\text{right}}| \leq 2$ eV) of a 15 ML NiO/Ag film are shown for primary energies from 22.6 to 68.6 eV.

4.2.2 Thickness Dependence

In the beginning of the chapter we compared the integral coincidence intensity of NiO to Ag and we found out, that for NiO the intensity is almost one order of magnitude higher. In other words, ten times more electrons are emitted from the surface in the detection range. Different explanation are imaginable. As pointed out earlier, the effective U for NiO is higher than for Ag and theoretically a higher count rate would be expected. An other explanation could be the higher mean free path of insulators compared to metals at energies due to the energy gap ($E_{\text{gap}}(\text{NiO}) = 4.3 \text{ eV}$). The mean free path is the average traveling length of an electron in the solid before collision. A well established method to determine the mean free path is the over layer method.

We deposited NiO on Ag(100) and follow the (e,2e) intensity of NiO. All existing data points for the mean free path are summarized in an “universal curve”, where the electron energy versus escape depth is plotted [49]. The mean free path of Ag for single electrons in the energy range from 30 and 60 eV is around 5 – 6 Å, the primary electrons travel in this depth inside the surface. The “universal curve” is only an approximation of the escape depth and not a general function of all materials. It is very difficult to obtain reliable data, especially from older literature. One difficulty is to determine the exact film thickness by applying the overlayer method. In our experiment, we are sure about this aspect, because of the observed MEED oscillation (Fig. 3.10) and reported STM data [94, 107]. In particular, values for compounds are rarely to be found in the literature. Recently the inelastic mean free path of CoO was published Offi *et al.* [108]. At an energy value of 9 eV the IMFP is stated with 8 Å, which corresponds to approx. 3.8 ML (1 ML $\hat{=}$ 2.1 Å [90]). This value is in the same range as the experimental values for Au, Ag [109] and Cu [110]. To our knowledge, for electron pairs exists no data on the mean free path available.

After having demonstrated our ability to control the film thickness we prepared different samples and performed coincidence experiments. From the arrival time histograms (like Fig. 3.1) we can determine the number of *true* counts. With the known acquisition time we quote the *true* coincidence rate. Since the primary flux is known we finally obtain the coincidence intensity per incoming primary electron. In Fig. 4.17 we present the thickness dependence of this quantity at room temperature. The lowest measured film thickness is 2.5 ML, because from 2 ML on the growth take place in a layer-by-layer fashion. The highest film thickness is 14.8 ML. At this thickness the coincidence rate is saturated. The intensity of the 2.5 ML film is more than 60% of of the thickest film.

The overall thickness dependence of the coincidence intensity can be described by an exponential behavior

$$I_n = I_{\text{Substrate}} + I_{\infty}(1 - \exp(-n/\lambda_n \cos \theta)). \quad (4.8)$$

$I_{\text{Substrate}}$ indicates the intensity from the substrate, in our experiment Ag. The coincidence rate is $0.5 \times 10^{-7} \text{ coin/e}^-$ and it is included in Fig. 4.17 as ▲. I_{∞} represents the thick saturated overlayer. n defines the numbers of overlayers. I_n is the intensity of the particular overlayer and λ_n is the inelastic mean free path (IMFP) which is defined as the distance over which the

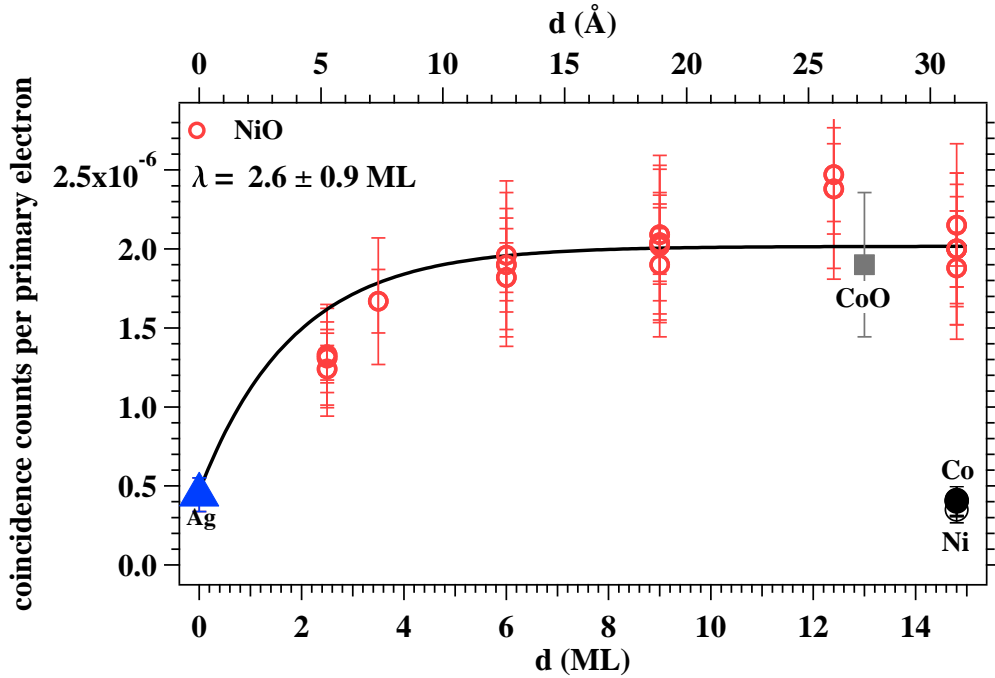


Figure 4.17 Summary of the coincidence intensity for NiO/Ag(100) (\circ) films as a function of the film thickness. At 0 ML the coincidence intensity of Ag (\blacktriangle) is used as off-set to evaluate the mean free path λ of NiO electron pair. The black line indicates the fit function according to Eq. (4.8). Coincidence intensity of CoO (\blacksquare), Ni (\circ) and Co (\bullet) are shown, but not considered in the fit. Primary electrons were accelerated to 32 V.

probability of an electron escaping without significant energy loss due to inelastic process drops to e^{-1} of its original value. θ is the detection angle (in this experiment $\theta = 45^\circ$).

Applying Eq. (4.8) to the Ag and NiO data of Fig. 4.17 results in $\lambda_n = 2.6 \pm 0.9$ ML.

In our experiment an electron pair is emitted, meaning two electrons need to travel outside the surface and overcome the surface barrier. The measured λ_n is therefore the half of the value obtained in a single electron experiment. One can corroborate this, if we consider the attenuation of the primary beam and the attenuation of the two outgoing electrons and the emission geometry. Using recently obtained values for the similar system CoO/Ag(100) in the energy regime of our studies explains our effective attenuation length [108]. Although the mean free path in metals is significantly shorter than those in CoO [42, 111, 112, 113] in the kinetic energy range of this study, this fact is not responsible for the high coincidence intensity for NiO. This can be immediately read from Fig. 4.17 where also data points for Ni and Co polycrystalline films are shown. Even the 2.5 ML NiO film has a larger intensity than the metallic films. In Fig. 4.17 we also included intensity value for a 13 ML CoO/Ag(100) films. The coincidence intensity is essentially identical to those of the NiO films.

We can clearly see that the intensity levels for NiO and CoO are significantly higher compared to the metallic samples. As discussed before NiO and CoO can be regarded as “highly correlated” materials due to the need of including an additional parameter U describing the electron correlation. As our experimental technique is in particular sensitive to the electron-electron interaction

we observe a strong coincidence intensity.

4.2.3 Temperature Dependence

NiO is an insulator and also an antiferromagnet. Below the Néel temperature T_N the spins are ordered. Above the Néel temperature the long range order vanishes. The film thickness changes the Néel temperature.

Via magnetic linear dichroism experiments the magnetic properties of NiO films were studied [114, 115, 116]. These measurements provided the thickness dependence of T_N , see Tab. 4.2. Interestingly, a coverage of 3 ML NiO/Ag(100) revealed a $T_N = 390$ K [116], but for NiO on a MgO(100) surface an ordering temperature below 40 K was measured. According to [4] for 5 ML is $T_N = 295$ K and it increases for 20 ML to $T_N = 470$ K.

Table 4.2 Thickness dependence of NiO films on a Ag(100) and MgO(100) surface [114, 115, 116].

NiO/Ag	NiO/MgO
$T_N(3 \text{ ML}) = 390 \text{ K}$	$T_N(3\text{ML}) < 40 \text{ K}$
	$T_N(5\text{ML}) = 295 \text{ K}$
	$T_N(10\text{ML}) = 430 \text{ K}$
	$T_N(20\text{ML}) = 470 \text{ K}$
$T_N(30\text{ML}) = 535 \text{ K}$	

We cooled down three samples with film thicknesses of 2.5, 6 and 14.8 ML to 110 K to be under the Néel temperature. At room temperature the 2.5 ML film is most likely above T_N . The 6.4 ML film is within the critical point and the 14.8 ML is under T_N . First of all, we observed no difference in the single count rate for both temperatures.

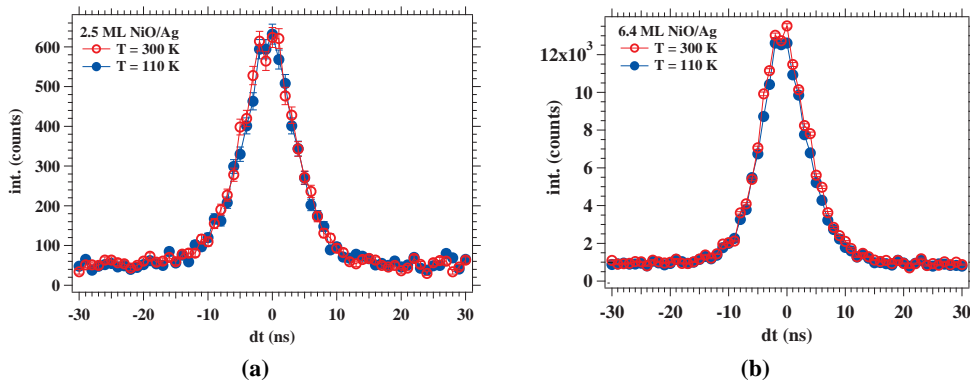


Figure 4.18 Arrival time histogram for (a) 2.4 ML and (b) 6 ML thick NiO/Ag(100) film. The measurements were performed at either 300 K (\circ) or 110 K (\bullet). The data acquisition time for each spectrum was 1 h.

Furthermore, we obtained the integral coincidence spectra for all conditions. The belonging spectra are identical, as can be seen in Fig. 4.18 for 2.4 ML (a) and 6 ML (b).

In Fig. 4.19 the coincidence signal as function of the film thickness is summarized, including data at RT (red) and 100 K (blue). We observe no difference between the data points at RT and 100 K.

An explanation of this result is that local interaction are probed in the coincidence experiment. Local interaction means electron-electron interaction between nearest neighbours. This interaction energy is for NiO in the range of 4 – 8 eV NiO (see Sec. 2.4.2). Whereas the temperature change from 300 to 110 K is associated with the mean thermal energy of 25 meV.

Besides cooling down, we increased the temperature up to 500 K, and observed no change in the count rate.

The current theoretical description of the (e,2e) and DPE process states that the observed intensity arises from the local correlation. This can be understood within on the basis of the exchange-correlation hole [55, 56]. This important concept of solid state theory states that each electron is surrounded by a reduced electronic charge density. Furthermore, the integration yields a charge deficit of exactly one elementary charge. This means that the interaction of this electron with other electrons is efficiently screened over distances which are larger than the extension of the exchange-correlation hole. It is commonly assumed that the spatial extension of it is a few Å.

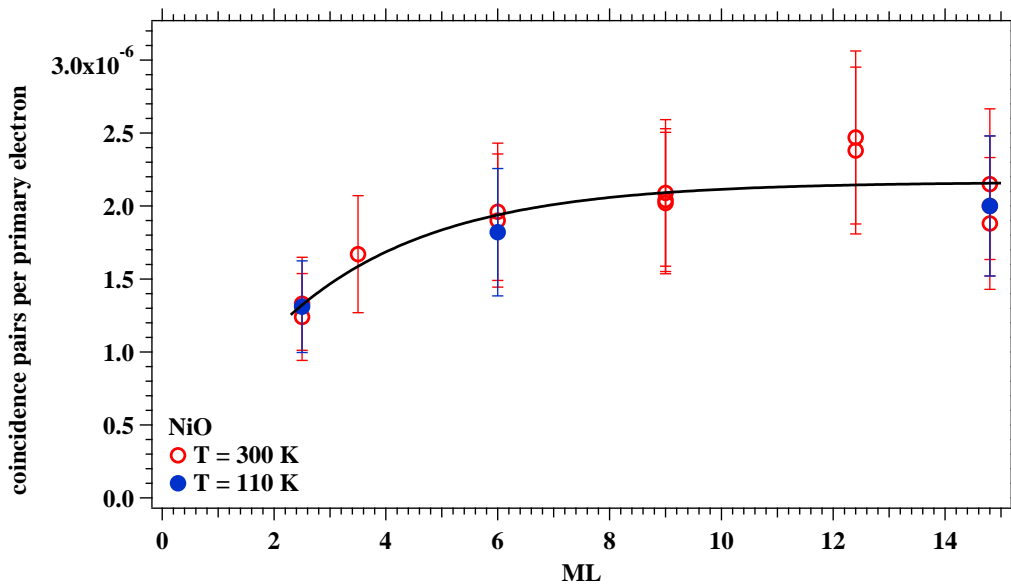


Figure 4.19 Summary of the coincidence intensity for NiO/Ag(100) films as a function of the thickness. We show the data measured at 300 K (\circ) and 110 K (\bullet). The dashed line is a guide for the eye.

In order to have a finite electron pair emission intensity it is required that the electrons interact which occurs only within close proximity of each other. This fact is implemented by the theoretical description of pair emission via a screened Coulomb interaction with a screening length

of a few Å [81, 117]. This quantity does not depend on the temperature which extends to the coincidence intensity, too. In particular, no changes are expected if the Néel temperature T_N is exceeded where the long range magnetic order disappears.

On the other hand, there is clear experimental evidence that the intensity in Auger and photoelectron coincidence studies changes at the Néel temperature for CoO [26, 118]. They studied Co Auger transition, which involves two valence electrons, in coincidence with the Co 3p photoelectron. The coincidence Auger spectra obtained for two geometries revealed a difference which vanished once the Néel temperature was crossed. This observation was ascribed to a collapse of the short range order at T_N .

From this point of view, it is important to determine whether the (e,2e) process displays a dependence on the order parameter to confirm current (e,2e) theory.

4.3 (e,2e) on Transition Metals

This section will concentrate on the coincidence intensity of transition metals. These metals are in particular interesting for coincidence experiments, because of the partial or fully filled d-valence band. The d-shell contains up to 10 electrons, the d-bands are flat, so the electrons are localized. Hence the electrons tend to interact stronger with each other than with sp electrons, which should be visible in the pair emission signal. In this work we investigated in addition to a Ag(100) crystal films of Fe, Co, Ni, Cu and Pd. The metals were evaporated onto the Ag crystal via MBE.

The film composition was measured by Auger spectroscopy to assure that no signal from the substrate influences the result. The coincidence experiment is even more surface sensitive than the Auger measurement. The films are polycrystalline, but the morphology has no effect on the signal, because we probe the local electron-electron interaction.

The conditions for the (e,2e) experiments were the same for all metals. That means equal primary energy of $E_p = 30$ eV. The ratio between the true and the accidental events T/A was kept around 3.8.

A typical (e,2e) spectrum of a polycrystalline Ni film is presented in Fig. 4.20. In Fig. 4.20a we see the 2D energy distribution of the emitted pair. The maximum sum energy edge is seen clearly. In Fig. 4.20b the sum energy of the pair is plotted ($E_{\text{sum}}^{\text{max}}$ is subtracted). At the Fermi edge we can observe enhanced intensity, also at an energy of 4.5 eV.

Although, analyzing the structure of the spectrum is out of the scope of this work, we would like to make several notes. It is reasonable, to have an enhanced intensity at the Fermi edge, because the DOS at E_F is very high. Furthermore, we can identify structure in the sum energy spectrum. The blurred structures cannot be attributed to the experimental resolution, because when we measure the Ag(100) crystal under the same conditions, we are able to see sharp features.

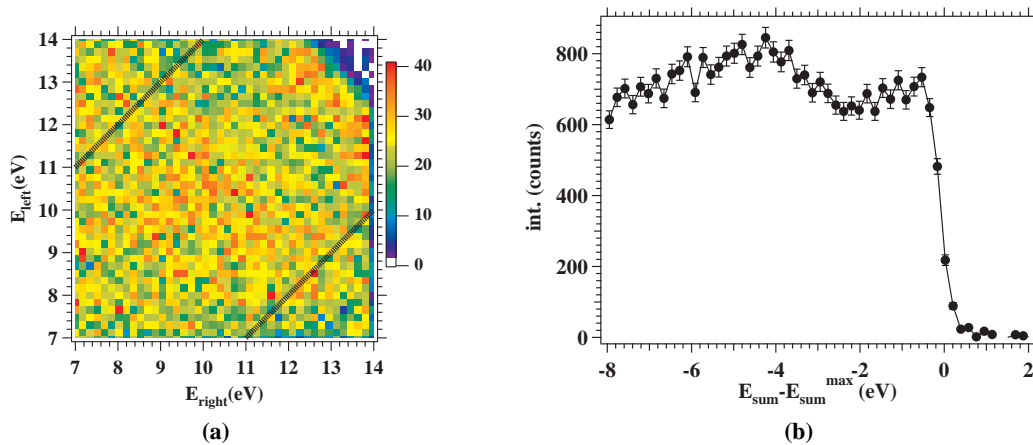


Figure 4.20 Polycrystalline Ni film ($E_p = 30$ eV) (a) 2D energy distribution, (b) sum energy spectrum ($|E_{\text{right}} - E_{\text{left}}| \leq 4$ eV).

The integral coincidence counts were measured for the mentioned materials and summarized in Fig. 4.21a. The coincidence pairs per primary electron vary from 3 to 6×10^{-7} counts. The

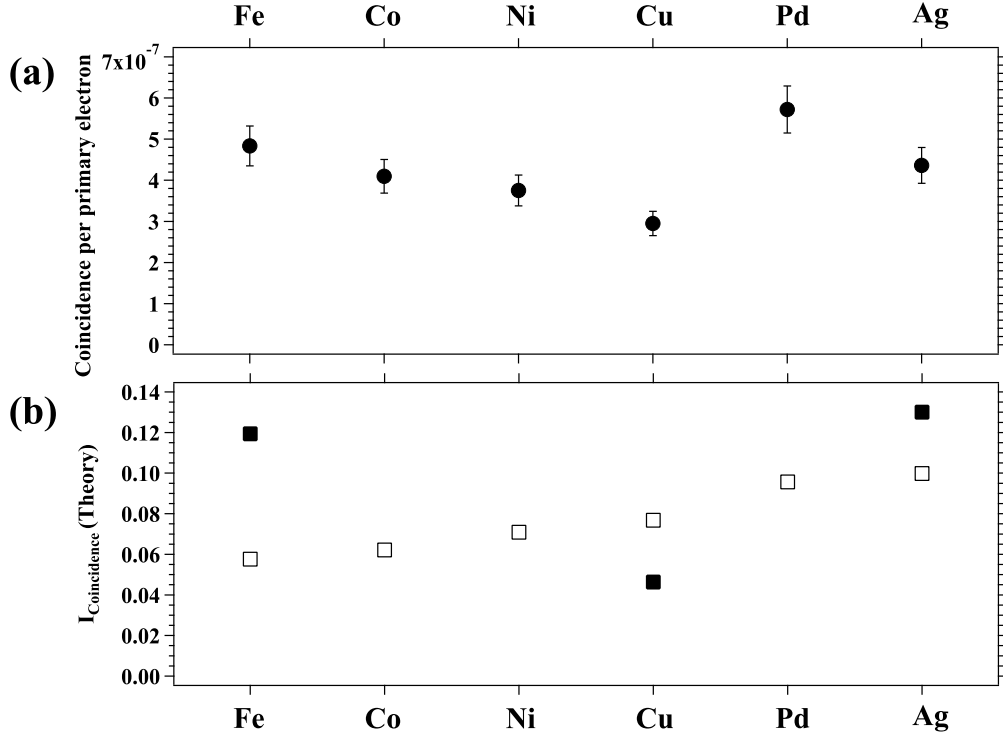


Figure 4.21 (a) Coincidence pairs per primary energy for Fe, Co, Ni, Cu, Pd and Ag. (b) Theoretical coincidence intensities. Values taken from Tab. 4.3 (□) and Tab. 4.4 (■).

highest count rate shows Pd. It is followed by Fe. Co and Ag are the next ones with almost the same value. Then Ni appears. The lowest emission is observed for Cu.

Table 4.3 Thomas-Fermi screening length λ_{TF} and strength q_{TF} and the theoretical coincidence intensity I_{coin} for the investigated metals ($\mathbf{k}_i - \mathbf{k}_j$ is set to 0). The Fermi energy E_F is taken from Ref. [63].

	E_F (eV)	$k_F(10^8/\text{cm})$	$\lambda_{TF}(\text{\AA})$	$q_{TF}(1/\text{\AA})$	$I_{coin}(1/\text{\AA}^4)$
Fe	11.33	1.73	0.49	2.04	0.058
Co	10.5	1.67	0.50	2.00	0.062
Ni	9.21	1.56	0.52	1.92	0.071
Cu	8.5	1.50	0.53	1.89	0.077
Pd	6.82	1.34	0.57	1.75	0.096
Ag	6.54	1.32	0.56	1.79	0.100

One could explain the count rate differences with the different screening length λ_{TF} . The values are calculated for the investigated metals using the Fermi energy E_F calculated by Moruzzi *et al.* [63]. E_F is converted in the wave vector k_F , assuming that the Fermi surface is a sphere. The results are used as the input of Eq. 2.39 to calculate λ_{TF} . The results are summarized in Tab. 4.3. The screening length and the electron-electron interaction are strongly related. Furthermore, we assume that the coincidence signal is strongly depended on the electron-electron interaction.

Combining this two statements results in

$$I_{\text{coincidence}} \propto \left| \frac{1}{(\mathbf{k}_i - \mathbf{k}_j)^2 + q_{\text{TF}}^2} \right|^2, \quad (4.9)$$

$\mathbf{k}_i - \mathbf{k}_j$ refers to the momentum transfer from the initial to the final state. Equation 4.9 is the Fourier transform from the so-called Yukawa potential, $V(r_{12}) = -k \exp(q_{\text{TF}} r_{12})/r_{12}$. The Fourier transform provides the amplitude of the scattering event. Assuming, that the momentum transfer is equal for all metals, because the experimental conditions are the same, the coincidence intensity $I_{\text{coincidence}}$ is higher when the screening strength q_{TF} is smaller or rather the screening length λ_{TF} is larger.

The increasing of the coincidence intensity with smaller screening parameter is illustrated in Fig. 4.22 as an example for a C-60 cluster. The cross-section is plotted as function of the impact energy. For impact energies below 100 eV, the cross section increases with smaller screening strength, which results in a higher coincidence intensity.

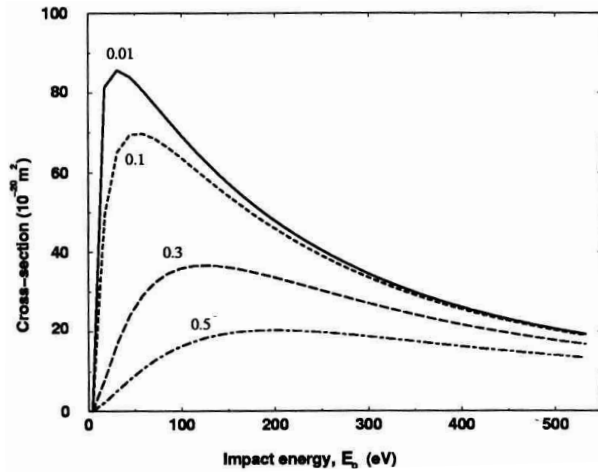


Figure 4.22 The total ionization cross-section for the electron scattering from C₆₀ as function of the impact energy. The cross section is calculated for various values of q_{TF} [61].

The comparison between experimental results and theoretical calculations (Fig. 4.21b □) shows no agreement. For example, the calculated value of I_{coin} is the lowest of all elements. But in the experiment, the value is the second highest.

Therefore, the assumption of isotropic electron distribution is too simple and cannot be used in this case. The next step is, to calculate the screening length with more realistic model.

In the literature the screening length is calculated for Fe(100) [97], Cu(111) [59] and Cu (001) [100], using a more sophisticated band structure model. The Cu values for different directions are almost the same. The screening length λ_{TF} for Fe is larger than of Cu. The coincidence intensity I_{coin} is obtained with Eq. 4.9. The resulting intensity I_{coin} of Fe is higher compared to Cu (Tab. 4.4).

Table 4.4 Thomas-Fermi screening length λ_{TF} and strength q_{TF} and the theoretical coincidence intensity I_{coin} for the investigated metals ($\mathbf{k}_i - \mathbf{k}_j$ is set to 0).

	$\lambda_{\text{TF}}(\text{\AA})$	$q_{\text{TF}}(1/\text{\AA})$	$I_{\text{coin}}(1/\text{\AA}^4)$
Fe(100) [97]	0.59	1.70	0.12
Cu(111) [59]	0.46	2.20	0.04
Cu(001) [100]	0.47	2.12	0.05
Ag(100)	0.60	1.67	0.13

To complement the evaluation, the DOS for Ag(100) at the Fermi energy is calculated by Jürgen Henk. The bulk value is 0.259 states/(eV · primitive cell). The lattice constant is 4.04 Å. The screening length is therefor $\lambda_{\text{TF}} = 0.60$ Å and the coincidence intensity $I_{\text{coin}} = 0.13$.

The three elements are added in Fig. 4.21 labeled with ■. The theoretical values of Fe and Ag are almost the same. The theoretical value of Cu is less than the half of them. The same behaviour for this elements is observed for the measured coincidence counts.

4.4 Pair vs. Single Electron Emission

After studying the coincidence intensities for different materials and primary energies the question is, how likely is the probability that two electrons are emitted by one incoming electron. To give an answer the absolute pair emission per primary electron is plotted in dependence of single counts per primary electron. All absolute data points discussed in the previous sections are summarized in Fig. 4.23. The Ag data of different primary energies is coloured in ▲. The NiO data of different film thicknesses is highlighted with a ○. The data point of the 15 ML CoO film is ■. The metal films (Fe, Co, Ni, Cu, Pd) are marked in ○.

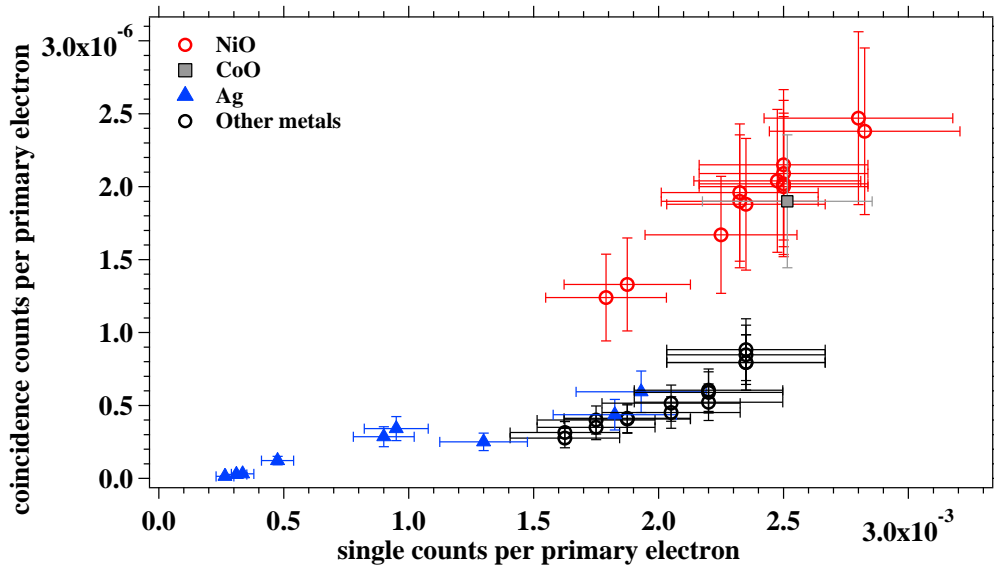


Figure 4.23 Summarized pair intensity in dependence of the single count rate for NiO in different film thicknesses (○), 15 ML CoO film (■), Ag for different primary energies (▲) and metal films of Fe, Co, Ni, Cu, Pd (○).

Single and coincidence counts are proportional to each other for all data points. For example, when the single electron emission is high, the electron pair emission is high, too.

From this fact alone it is obvious that the pair emission process must be a rather efficient process. This may not be at first glance obvious since of the order 10^6 primary electrons are required to detect a coincidence pair. However, it has to be remembered that each spectrometer captures only a fraction of the half space.

The solid angle Ω is calculated as follows

$$\Omega = 2\pi \left(1 - \cos\left(\frac{\alpha}{2}\right)\right). \quad (4.10)$$

In our experiment the acceptance angle is $\pm 15^\circ$ ($\alpha = 30^\circ$). This results in a solid angle of 0.21 sr^1 . Hence we cover with one analyzer 3.4 % of the hemisphere. This percentage is labeled with S . For the single electron emission the value is scaled directly to the intensity ($I_{\text{single}}^\pi = I_{\text{single}}/S$). For the pair emission the intensity goes with the square of the solid angle ($I_{\text{pair}}^\pi =$

¹sr stands for steradian and is the SI unit of the solid angle.

I_{pair}/S^2).

In the NiO experiment we measured around one electron pair while 1000 single counts were detected. If we could cover the whole solid angle, we would detect $I_{\text{pair}}^\pi = 865$ and $I_{\text{single}}^\pi = 29412$.

The pair emission efficiency η_{pair} is the ratio of the emitted pairs over the whole hemisphere to the single emission

$$\eta_{\text{pair}} = \frac{I_{\text{pair}}^\pi}{I_{\text{single}}^\pi} = \frac{I_{\text{pair}}}{I_{\text{single}}} \times \frac{1}{S}. \quad (4.11)$$

When we assume isotropic emission in space, this efficiency η_{pair} is for NiO 3%. In other words, three of 100 detected electrons belong to an electron pair. Actually, the solid angle is even smaller, because when the electrons enter the hemisphere, they have to pass through a slit and some electrons are cut off. The 3% is the lower boundary of the pair efficiency.

In Fig. 4.24 the pair emission efficiency η_{pair} is plotted as function of the acceptance angle $\alpha/2$ for NiO. If $\alpha/2$ is decreased about 5°, η_{pair} is increased to 6%.

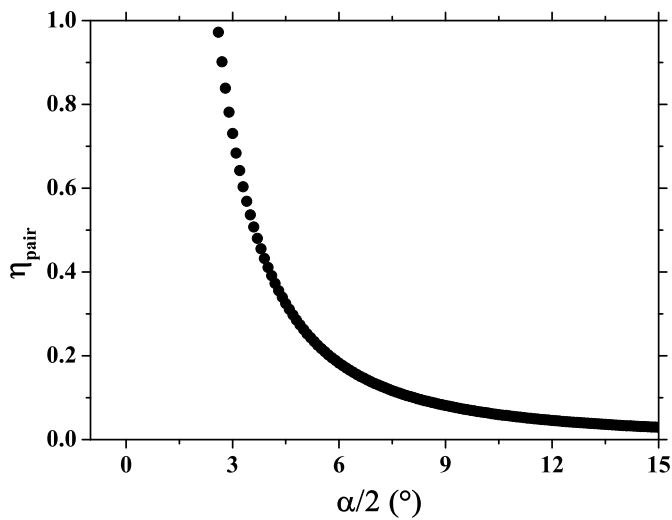


Figure 4.24 Pair emission efficiency η_{pair} as function of the acceptance angle $\alpha/2$ for NiO.

5 Conclusions and Outlook

In this work the interaction between electrons was studied by (e,2e) coincidence measurements. The surface was excited with an electron and an emitted electron pair was detected. The electron correlation strength can be described by U . Experimentally, the value of U can be changed by using different materials.

In this thesis for the first time, the transition metal oxides NiO and CoO were investigated with (e,2e) as so-called strongly correlated materials with a value of U in the range of 8 eV. Ag was chosen as a weakly correlated material with a value of $U \approx 0$.

We observed that the pair emission signal of NiO compared to Ag was enhanced by a factor of 10. This shows the first evidence, that the pair emission probability is strongly dependent on the correlation of the electrons. For the first time a connection between electron correlation and the coincidence intensity was shown. Our result was supported by theoretical pair emission calculations [13]. In addition, we systematically investigated the coincidence intensity of transition metals such as Fe, Co, Ni, Cu and Pd. We observed higher coincidence intensity for the TMOs compared to these metals.

Due to the high coincidence count rate of NiO, for the first time the pair emission intensity was measured in dependence of the film thickness and temperature. We successfully grew NiO on Ag(100) and monitored the film thickness with MEED.

It can be excluded, that the enhancement of the coincidence signal is due to a larger mean free path in the insulator NiO compared to Ag. The absolute coincidence pairs per primary electron were studied for different NiO film thickness. The signal saturated exponentially with NiO film thickness. With the so-called over-layer method, we obtained for the first time, the IMFP of an electron pair with $\lambda = 2.6 \pm 0.9$ ML.

Furthermore, NiO is an antiferromagnet. The Néel temperature changes with film thickness. For different film thicknesses we compared the coincidence signal below and above the Néel temperature. We observed, that the pair emission intensity was equal for both temperatures. This is explained by the spatial range of the energy involved.

The antiferromagnetic coupling is in the long range order. Whereas, the correlation energy U is the energy penalty two electrons have to pay to stay at one lattice site. This reveals that the local electron correlation is probed, being a key aspect of the experimental set-up.

The sum energy signal of NiO and Ag pairs were compared with the DOS. We observed, that pair emission just occurred, where electronic states were available. We were not expecting to mimic the DOS, because we probed a many particle system and we measured all electron interactions. We showed, that the DOS was not valid as interpretation of our data.

In the case of NiO the DOS showed sharp peaks, but the features in the coincidence spectra were broad. The broadening of the features reflects the strong interaction of the electrons.

The Ag spectrum has low DOS in the region near E_f . However, in the experiment high intensities were measured.

An improvement to previous experiments was the ability to measure the primary electron flux. This allowed the determination of the single/coincidence count rate per incoming electron. The spectra were divided into regions with different orbital characters with the help of a theoretical band structure calculation. We systematically studied the electron pair emission as function of the primary energy ($E_p = 30$ to 67 eV). The relative spectral contribution from the electrons near E_f were strongly affected by the primary electron energy and displayed a non-monotonic behavior.

This phenomena could be explained by pair diffraction on the Ag(100) surface, as stated for Cu(100) in Ref. [31]. A kinematic pair diffraction model described the results reasonably well. The approach is justified by current (e,2e) theory, which characterizes the in-coming and out-going electrons by LEED and time reversed LEED-states, respectively.

The ability to measure the primary electron flux enabled us to study the relation between the single and the coincidence counts for the first time. We noticed, that a high single count rate resulted in high coincidence count rate. Furthermore, we found out that the pair emission is a rather efficient process.

A natural extension of this work would be to investigate the electron pair emission of TMO compared to metals by exciting the surface with other particles, as photons or positrons. In this way, we would gain a deeper knowledge of the electron correlation.

In the future, it would be also highly interesting to study the pair emission process of other highly correlated systems. Promising materials are superconductors, which can not be explained in an independent particle picture. For example within the BCS theory electrons form a Cooper pair.

Appendix

Coincidence Logic

Technically the arrival time histogram can be obtained as follows: one electron serves as start signal (“red”) and the other one as stop (“blue”). The signals are picked up from the MCP. The time difference of the signals are converted in an amplitude via Time-To-Amplitude-Converter (TAC). If the signals reach at the same time, the difference is 0 ± 10 ns. To collect all data and the peak is shifted in the middle of the time window by delaying the "blue" signal around 100 ns. A schematic circuit can be found in Fig. .1.

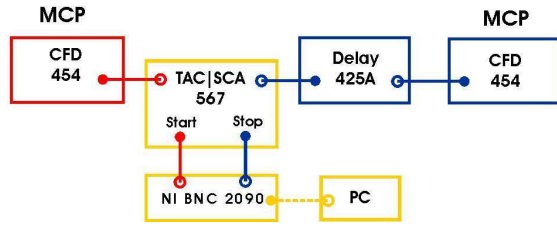


Figure .1 Schematic time to amplitude converter circuit. The MCP signal from both detectors, “red” and “blue”, is transferred to the Time-to-Amplitude-Converter-Unit. The “red” signal serves as start signal and the “blue” as stop signal. The arrival time difference of these two signals within 200 ns is considered. If the signals reach at the same time, the difference is 0 ± 10 ns. To collect all data and shift the peak in the middle of the time window, the "blue" signal is delayed around 100 ns.

Electron Trajectories inside the Hemisphere

The trajectories equation of the electrons are derived shortly. The electric potential $\phi(r)$ inside the hemisphere can be described by

$$\phi(r) = -\frac{k}{r} + C. \quad (1)$$

Whereby

$$k = e \frac{(U_1 - U_2)R_1R_2}{R_2 - R_1}. \quad (2)$$

In our set up $R_1 = 160$ mm and $R_2 = 240$ mm

$$C = -e \frac{U_2R_2 - U_1R_1}{R_2 - R_1}. \quad (3)$$

The equation of motion the electron has to full fill (written in cylindrical coordinates) is

$$\frac{m}{2}(\dot{r}^2 + r^2\dot{\varphi}^2) - \frac{k}{r} = E. \quad (4)$$

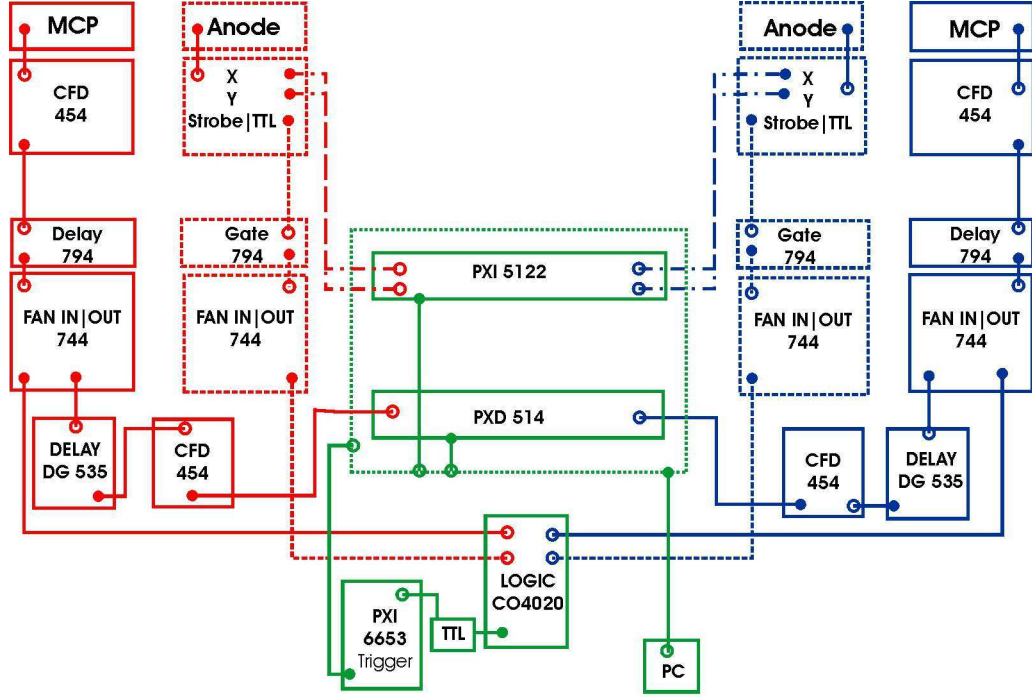


Figure .2 Schematic coincidence logic circuit is presented. The "red" and "blue" signals from MCP define the time and the signals from the anode provide the energy information of the electron pair. Via a logic unit both signals are triggered together.

The angular momentum L is

$$L = m\dot{\varphi}r^2. \quad (5)$$

The velocity of the electron on the trajectory is $dr/dt = dr/d\varphi \cdot \dot{\varphi} = dr/d\varphi \cdot L/(mr^2)$. Including this equation in Eq. (4) and some transformation results in the following differential equation and substitutions

$$\frac{dr}{d\varphi} = \underbrace{\frac{mr^2}{L}}_{\frac{dr}{du}} \sqrt{\underbrace{\frac{2E}{m} + \left(\frac{k}{L}\right)^2}_{\beta^2} - \underbrace{\left(\frac{k}{L}\right)^2 - \frac{2k}{mr} + \left(\frac{L}{mr}\right)^2}_{u^2}}. \quad (6)$$

The differential equation is reduced to and the solution is

$$d\varphi = \frac{du}{\sqrt{\beta^2 - u^2}} \hookrightarrow u = \beta \cos(\varphi - \varphi_0). \quad (7)$$

The trajectory is therefore

$$r(\varphi) = \frac{L^2/(mk)}{1 - \beta L/K \cdot \cos(\varphi - \varphi_0)} = \frac{p}{1 - \epsilon \cdot \cos(\varphi - \varphi_0)}. \quad (8)$$

The equation describes an elliptic conic section with the parameters p denoted as the semi-latus rectum of the ellipse and the eccentricity $\epsilon = \sqrt{1 + 2EL^2/(mk^2)}$. When the value $0 < \epsilon < 1$

the pathway describes an ellipse. Hence the energy E is negative, more precisely the energy has to full fill $E = E_{\text{kin}} - 2E_{\text{pass}}$. An important parameter that influence the trajectory, is the entrance angle α .

The absolute value of the angular momentum

$$L(\alpha)|_{\varphi=0} = mv_0 r_0 = r_0 \sqrt{2mE_{\text{pass}}} \cdot \cos \alpha. \quad (9)$$

Primary Flux Meter Circuit

The filterbox circuit diagram of the flux meter is presented in Fig. .3. A high voltage of +1620 V was applied at HV in. The voltage is divided in 110 V for the MCP back, 1505 V for the MCP front and 4.2 V to the Anode. Additionally a grid voltage of 10 eV was applied to repel the energetic low electrons. Furthermore it can be applied a voltage to the case to manipulate the ground potential. Pulse out is coneted to a rate meter. The pulse transformer inside the filterbox add up signal from MCP and Anode.

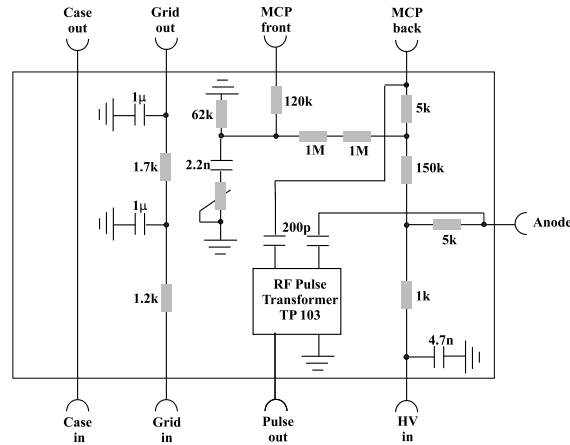


Figure .3 Circuit diagram of the flux meter.

Extraction of True Events

How the true counts are extracted from the experimental data is explained in the following. The histogram gives information about true and random events. To determine the random background level, the histogram is fitted with a Gaussian peak for convenience. It has to be emphasized that the count distribution is only approximatively Gaussian. For this analyze only the offset of the Gaussian is considered, which is the average uniform background \bar{b} .

The total random counts A_{all} in the dwell time t are

$$A_{\text{all}} = t \cdot \bar{b}. \quad (10)$$

The random counts A under the true peak are

$$A = \frac{\bar{b} \cdot w \cdot 2 \cdot t}{t_{\text{max}} - t_{\text{min}}}, \quad (11)$$

w is the width of the peak and estimated with FWHM of the Gaussian.

All true counts T in the experiment are defined as the difference between the average of all total counts \overline{all} and the average random counts \overline{b} multiplied by the dwell time t

$$T = (\overline{all} - \overline{b}) \cdot t. \quad (.12)$$

In the experiment the total coincidence rate per second C_{cps} is monitored a rate meter, including random and true events.

$$T_{cps} = \frac{T \cdot C_{cps}}{t \cdot \overline{all}}. \quad (.13)$$

Bibliography

- [1] K. Marre, H. Neddermeyer, A. Chasse, and P. Rennert, *Surf. Sci.* **357-358**, 233 (1996).
- [2] M. Portalupi, L. Duò, G. Isella, R. Bertacco, M. Marcon, and F. Ciccacci, *Phys. Rev. B* **64**, 1 (2001).
- [3] O. Tjernberg, S. Söderholm, T. Rogelet, U. O. Karlsson, M. Qvarford, I. Lindau, C. Almladh, and L. Hellbom, *Vacuum* **46**, 1215 (1995).
- [4] D. Alders, L. Tjeng, F. Voogt, T. Hibma, G. Sawatzky, C. Chen, J. Vogel, M. Sacchi, and S. Iacobucci, *Phys. Rev. B* **57**, 11623 (1998).
- [5] M. R. Thuler, R. L. Benbow, and Z. Hurych, *Phys. Rev. B* **27**, 2082 (1983).
- [6] A. Dhaka, D. Sander, H. L. Meyerheim, K. Mohseni, E. Soyka, J. Kirschner, W. A. Adeagbo, G. Fischer, A. Ernst, and W. Hergert, *Phys. Rev. B* **84**, 195441 (2011).
- [7] S. Hüfner, P. Steiner, I. Sander, M. Neumann, and S. Witzel, *Zeitschrift für Physik B Condensed Matter* **83**, 185 (1991).
- [8] F. Manghi and C. Calandra, *Phys. Rev. Lett.* **73**, 3129 (1994).
- [9] G. A. Sawatzky and J. W. Allen, *Phys. Rev. Lett.* **53**, 2339 (1984).
- [10] O. Miura and T. Fujiwara, *Phys. Rev. B* **77**, 195124 (2008).
- [11] X. Ren, I. Leonov, G. Keller, M. Kollar, I. Nekrasov, and D. Vollhardt, *Phys. Rev. B* **74**, 195114 (2006).
- [12] S. L. Dudarev, G. A. Botton, S. Y. Savrasov, Z. Szotek, W. M. Temmerman, and A. P. Sutton, *Physica Status Solidi A* **166**, 429 (1998).
- [13] B. D. Napitu and J. Berakdar, *Phys. Rev. B* **81**, 195108 (2010).
- [14] W. Bothe and H. Geiger, *ZS. f. Phys.* **26**, 44 (1924).
- [15] N. Bohr, H. A. Kramers, and J. C. Slater, *ZS. f. Phys.* **24**, 69 (1924).
- [16] E. Weigold, L. Frost, and K. J. Nygaard, *Phys. Rev. A* **21**, 1950 (1980).
- [17] T. Jahnke, A. Czasch, M. S. Schöffler, S. Schössler, A. Knapp, M. Käs, J. Titze, C. Wimmer, K. Kreidi, R. E. Grisenti, A. Staudte, O. Jagutzki, U. Hergenhahn, H. Schmidt-Böcking, and R. Dörner, *Phys. Rev. Lett.* **93**, 163401 (2004).

- [18] J. S. Briggs and V. Schmidt, *J. Phys. B: At. Mol. Opt. Phys.* **33**, R1 (2000).
- [19] J. Viefhaus, A. N. Grum-Grzhimailo, N. M. Kabachnik, and U. Becker, *J. Electron. Spectrosc. Relat. Phenom.* **141**, 121 (2004).
- [20] J. V. Dunworth, *Rev. Sci. Instrum.* **11**, 167 (1940).
- [21] E. J. Hoffman, D. M. V. Patter, D. G. Sarantites, and J. Barker, *Nuclear Instruments and Methods* **109**, 3 (1973).
- [22] H. W. Haak, G. A. Sawatzky, and T. D. Thomas, *Phys. Rev. Lett.* **41**, 1825 (1978).
- [23] M. Hattass, T. Jahnke, S. Schössler, A. Czasch, M. Schöffler, L. P. H. Schmidt, B. Ulrich, O. Jagutzki, F. O. Schumann, C. Winkler, J. Kirschner, R. Dörner, and H. Schmidt-Böcking, *Phys. Rev. B* **77**, 165432 (2008).
- [24] G. A. Riessen, F. O. Schumann, M. Birke, C. Winkler, and J. Kirschner, in *Journal of Physics: Conference Series*, Vol. 185 (IOP Publishing, 2009) p. 012051.
- [25] G. A. van Riessen, Z. Wei, R. S. Dhaka, C. Winkler, F. O. Schumann, and J. Kirschner, *J. Phys.: Condens. Matter* **22**, 92201 (2010).
- [26] M. Cini, E. Perfetto, R. Gotter, F. Offi, A. Ruocco, and G. Stefani, *Phys. Rev. Lett.* **107**, 217602 (2011).
- [27] W. S. M. Werner, W. Smekal, H. Störi, H. Winter, G. Stefani, A. Ruocco, F. Offi, R. Gotter, A. Morgante, and F. Tommasini, *Phys. Rev. Lett.* **94**, 38302 (2005).
- [28] J. Kirschner, O. M. Artamonov, and A. Terekhov, *Phys. Rev. Lett.* **69**, 1711 (1992).
- [29] R. Feder, H. Gollisch, D. Meinert, T. Scheunemann, O. M. Artamonov, S. N. Samarin, and J. Kirschner, *Phys. Rev. B* **58**, 16418 (1998).
- [30] F. O. Schumann, C. Winkler, and J. Kirschner, *physica status solidi (b)* **246**, 1483 (2009).
- [31] Z. Wei, F. O. Schumann, R. Dhaka, and J. Kirschner, *Phys. Rev. B* **85**, 195120 (2012).
- [32] F. O. Schumann, R. S. Dhaka, G. A. van Riessen, Z. Wei, and J. Kirschner, *Phys. Rev. B* **84**, 125106 (2011).
- [33] E. Rutherford, *Philosophical Magazine* **21**, 669 (1911).
- [34] W. Nolting, *Grundkurs Theoretische Physik 5/1* (Springer-Verlag Berlin Heidelberg, 2004).
- [35] H. Haken and H. C. Wolf, *The Physics of Atoms and Quanta* (Springer-Verlag Berlin Heidelberg, 2005).
- [36] R. W. Robinett, *Quantum Mechanics* (Oxford University Press, 2006).

-
- [37] N. F. Mott and H. S. W. Massey, *The Theory of Atomic Collisions Vol. 1* (Oxford University Press, 1987).
- [38] S. Flügge, *Rechenmethoden der Quantentheorie* (Springer-Verlag Berlin Heidelberg, 1999).
- [39] J. B. Pendry, *Low Energy Electron Diffraction* (Academic Press, London and New York, 1974).
- [40] M. A. V. Hove, W. H. Weinberg, and C. M. Chan, *Low Energy Electrons and Surface Chemistry* (Springer, Heidelberg, 1985).
- [41] S. Hüfner, *Photoelectron Spectroscopy* (Springer, 2003).
- [42] G. Ertl and J. Küppers, *Low Energy Electrons and Surface Chemistry* (VCH Verlag, 1985).
- [43] H. Bethe, *Naturwissenschaften* **16**, 333 (1928).
- [44] H. Gollisch, X. Yi, T. Scheunemann, and R. Feder, *J. Phys.: Condens. Matter* **11**, 9555 (1999).
- [45] D. R. Penn, *Phys. Rev. B* **35**, 482 (1987).
- [46] C. J. Powell, *J. Electron. Spectrosc. Relat. Phenom.* **47**, 197 (1988).
- [47] C. J. Powell and A. Jablonski, *J. Phys. Chem. Ref. Data* **28**, 19 (1999).
- [48] W. S. M. Werner, *Surf. Interface Anal.* **18**, 217 (1992).
- [49] M. P. Seah and W. A. Dench, *Surf. Interface Anal.* (1979).
- [50] A. Jablonski and Tougaard, *J. Vac. Sci. Technol., A* **8**, 106 (1990).
- [51] W. Demtröder, *An Introduction to Atomic-, Molecular- and Quantum Physics* (Springer-Verlag Berlin Heidelberg, 2010).
- [52] F. O. Schumann, *Studying the electron-electron correlation by pair emission from surfaces*, Habilitation, Naturwissenschaftliche Fakultät II, Martin-Luther Universität Halle-Wittenberg (2012).
- [53] H. Lebius, H. R. Koslowski, K. Wiesemann, and B. A. Huber, *Annalen der Physik* **503** (1991).
- [54] O. Schwarzkopf, B. Krässig, J. Elmiger, and V. Schmidt, *Phys. Rev. Lett.* **70**, 3008 (1993).
- [55] E. Wigner and F. Seitz, *Phys. Rev.* **43**, 804 (1933).
- [56] J. C. Slater, *Rev. Mod. Phys.* **6**, 209 (1934).

- [57] F. O. Schumann, J. Kirschner, and J. Berakdar, *Phys. Rev. Lett.* **95**, 117601 (2005).
- [58] H. Ibach and H. Lüth, *Festkörperphysik* (Springer-Verlag Berlin Heidelberg, 2002).
- [59] H. Gollisch, N. v. Schwartzberg, and R. Feder, *Phys. Rev. B* **74**, 75407 (2006).
- [60] N. Fominykh and J. Berakdar, in *Many-Particle Spectroscopy of Atoms, Molecules, Clusters, and Surfaces*, edited by J. Berakdar and J. Kirschner (Kluwer Academic/Plenum Publisher, 2001).
- [61] O. Kidun and J. Berakdar, in *Many-Particle Spectroscopy of Atoms, Molecules, Clusters, and Surfaces*, edited by J. Berakdar and J. Kirschner (Kluwer Academic/Plenum Publisher, 2001).
- [62] W. Kohn and L. J. Sham, *Phys. Rev.* **140**, 1133 (1965).
- [63] V. L. Moruzzi, J. F. Janak, and A. R. Williams, *Calculated electronic properties of metals* (Pergamon Press New York, 1978).
- [64] R. W. G. Wyckoff, *Crystal structures Vol. I.* (New York, Interscience Publ., 1963).
- [65] O. Bengone, M. Alouani, P. Blöchl, and J. Hugel, *Phys. Rev. B* **62**, 392 (2000).
- [66] A. K. Cheetham and D. Hope, *Phys. Rev. B* **27**, 6964 (1983).
- [67] N. F. Mott and R. Peierls, *Proceedings of the Physical Society* **49**, 72 (1937).
- [68] F. O. Schumann, L. Behnke, C. Li, J. Kirschner, Y. Pavlyukh, and J. Berakdar, *Phys. Rev. B* **86**, 035131 (2012).
- [69] G. Kotliar and D. Vollhardt, *Physics Today* **57**, 53 (2004).
- [70] J. Zaanen, G. A. Sawatzky, and J. W. Allen, *Phys. Rev. Lett.* **55**, 418 (1985).
- [71] M. R. Castell, P. Wincott, N. Condon, C. Muggelberg, G. Thornton, S. L. Dudarev, A. P. Sutton, and G. Briggs, *Phys. Rev. B* **55**, 7859 (1997).
- [72] J. Kuneš, V. I. Anisimov, S. Skornyakov, A. V. Lukoyanov, and D. Vollhardt, *Phys. Rev. Lett.* **99**, 156404 (2007).
- [73] V. I. Anisimov, J. Zaanen, and O. K. Andersen, *Phys. Rev. B* **44**, 943 (1991).
- [74] A. Fujimori, F. Minami, and S. Sugano, *Phys. Rev. B* **29**, 5225 (1984).
- [75] V. I. Anisimov and F. Aryasetiawan, *Journal of Physics* **9**, 767 (1997).
- [76] H. Jiang, R. I. Gomez-Abal, P. Rinke, and M. Scheffler, *Phys. Rev. B* **82**, 45108 (2010).
- [77] C. Gazier and J. R. Prescott, *Phys. Lett. A* **32**, 425 (1970).
- [78] J. Berakdar, *Phys. Rev. B* **58**, 9808 (1998).

-
- [79] N. Fominykh, J. Henk, J. Berakdar, P. Bruno, H. Gollisch, and R. Feder, *Solid State Commun.* **113**, 665 (2000).
- [80] R. Feder and H. Gollisch, *Solid-State Photoemission and Related Methods*, edited by M. V. H. W. Schattke (Wiley-WCH, Weinheim, 2003) Chap. 9, p. 269.
- [81] J. Berakdar, H. Gollisch, and R. Feder, *Solid State Commun.* **112**, 587 (1999).
- [82] M. Völkel and W. Sandner, *J. Phys. E* **16**, 456 (1983).
- [83] E. Jensen, R. A. Bartynski, S. L. Hulbert, and E. D. Johnson, *Rev. Sci. Instrum.* **63**, 3013 (1992).
- [84] G. A. Sawatzky, *Auger Electron Spectroscopy*, edited by R. P. M. C.L. Bryant (Academic Press, San Diego, 1988) Chap. 5, p. 167.
- [85] H. W. Haak, G. A. Sawatzky, L. Ungier, J. K. Gimzewski, and T. D. Thomas, *Rev. Sci. Instrum.* **55**, 696 (1984).
- [86] P. Downie, D. Litchfield, R. Parsons, D. J. Reynolds, and I. Powis, *Measurement Science and Technology* **4**, 1293 (1993).
- [87] R. E. Imhof, A. Adams, and G. C. King, *J. Phys. E* **9**, 138 (1976).
- [88] O. Kugeler, S. Marburger, and U. Hergenbahn, *Rev. Sci. Instrum.* **74**, 3955 (2003).
- [89] G. Costantini, S. Rusponi, R. Gianotti, C. Boragno, and U. Valbusa, *Surf. Sci.* **416**, 245 (1998).
- [90] M. Caffio, B. Cortigiani, G. Rovida, and A. Atrei, *Surf. Sci.* **531**, 368 (2003).
- [91] A. Rota, S. Altieri, and S. Valeri, *Phys. Rev. B* **79**, 161401 (2009).
- [92] J. Wollschlager, D. Erdos, H. Goldbach, R. Hopken, and K. Schroder (Elsevier, [Lausanne, Switzerland, etc.], 2001) pp. 1–8.
- [93] F. O. Schumann, L. Behnke, C. H. Li, and J. Kirschner, *J. Phys.: Condens. Matter* **25**, 094002 (2013).
- [94] S. Großer, C. Hagendorf, H. Neddermeyer, and W. Widdra, *Surf. Interface Anal.* **40**, 1741 (2008).
- [95] S. N. Samarin, O. M. Artamonov, H. Schwabe, and J. Kirschner, in *Coincidence Studies of Electron and Photon Impact Ionization*, edited by C. Whelan and H. R. J. Walters (Plenum Press, New York, 1997).
- [96] M. Muñoz-Navia, C. Winkler, R. Patel, M. Birke, F. O. Schumann, and J. Kirschner, *J. Phys.: Condens. Matter* **21**, 355003 (2009).

- [97] F. Giebels, H. Gollisch, R. Feder, F. Schumann, C. Winkler, and J. Kirschner, *Phys. Rev. B* **84**, 165421 (2011).
- [98] K. Saha, J. Henk, A. Ernst, and P. Bruno, *Phys. Rev. B* **77**, 85427 (2008).
- [99] R. Courths, M. Lau, T. Scheunemann, H. Gollisch, and R. Feder, *Phys. Rev. B* **63**, 195110 (2001).
- [100] U. Rücker, H. Gollisch, and R. Feder, *Phys. Rev. B* **72**, 214424 (2005).
- [101] E. W. Hu, R. M. Goodman, and F. Jona, *Phys. Rev. B* **8**, 5519 (1973).
- [102] J. Berakdar, S. N. Samarin, R. Herrmann, and J. Kirschner, *Phys. Rev. Lett.* **81**, 3535 (1998).
- [103] S. Samarin, J. Berakdar, O. M. Artamonov, H. Schwabe, and J. Kirschner, *Surf. Sci.* **470**, 141 (2000).
- [104] F. O. Schumann, C. Winkler, and J. Kirschner, *Phys. Rev. Lett.* **98**, 257604 (2007).
- [105] F. O. Schumann, N. Fominykh, C. Winkler, J. Kirschner, and J. Berakdar, *Phys. Rev. B* **77**, 235434 (2008).
- [106] F. O. Schumann, C. Winkler, and J. Kirschner, *New J. Phys.* **9**, 372 (2007).
- [107] C. Giovanardi, A. di Bona, S. Altieri, P. Luches, M. Liberati, F. Rossi, and S. Valeri, *Thin Solid Films* **428**, 195 (2003).
- [108] F. Offi, S. Iacobucci, P. Vilmercati, A. Rizzo, A. Goldoni, M. Sacchi, and G. Panaccione, *Phys. Rev. B* **77**, 201101 (2008).
- [109] H. Kanter, *Phys. Rev. B* **1**, 522 (1970).
- [110] J. A. Knapp, F. J. Himpsel, and D. E. Eastman, *Phys. Rev. B* **19**, 4952 (1979).
- [111] D. P. Pappas, K. P. Kämper, B. P. Miller, H. Hopster, D. E. Fowler, C. R. Brundle, A. Luntz, and Z. Shen, *Phys. Rev. Lett.* **66**, 504 (1991).
- [112] F. Passek, M. Donath, and K. Ertl, *J. Magn. Magn. Mater.* **159**, 103 (1996).
- [113] M. Getzlaff, J. Bansmann, and G. Schönhense, *Solid State Commun.* **87**, 467 (1993).
- [114] D. Alders, J. Vogel, C. Levelut, S. D. Peacor, T. Hibma, M. Sacchi, L. H. Tjeng, C. T. Chen, G. van der Laan, B. T. Thole, and G. A. Sawatzky, *Europhys. Lett.* **32**, 259 (1995).
- [115] D. Alders, L. H. Tjeng, F. C. Voogt, T. Hibma, G. A. Sawatzky, C. T. Chen, J. Vogel, M. Sacchi, and S. Iacobucci, *Phys. Rev. B* **57**, 11623 (1998).
- [116] S. Altieri, M. Finazzi, H. H. Hsieh, H. J. Lin, C. Chen, T. Hibma, S. Valeri, and G. A. Sawatzky, *Phys. Rev. Lett.* **91**, 137201 (2003).

- [117] N. Fominykh, J. Berakdar, J. Henk, and P. Bruno, *Phys. Rev. Lett.* **89**, 086402 (2002).
- [118] R. Gotter, F. Offi, A. Ruocco, F. D. Pieve, R. Bartynski, M. Cini, and G. Stefani, *Europhys. Lett.* **94**, 37008 (2011).

Publications

- F. O. Schumann, L. Behnke, C.-H. Li, and J. Kirschner, *Exploring highly correlated materials via electron pair emission: the case of NiO/Ag(100)*, J. Phys.: Condens. Matter **25**, 094002 (2013)
- F. O. Schumann, L. Behnke, C.-H. Li, J. Kirschner, Y. Pavlyukh, and J. Berakdar, *Electron pair emission from a highly correlated material*, Phys. Rev. B **86**, 035131 (2012)

Posters/Talks

- L. Behnke, F. O. Schumann, and J. Kirschner, *Electron pair emission from Ag(100)*, Frühjahrstagung der Sektion Kondensierte Materie der Deutschen Physikalischen Gesellschaft, Regensburg, Germany. 10.-15.03.2013, Talk
- Z. Wei, F. O. Schumann, C.-H. Li, L. Behnke, G. Di Filippo, G. Stefani, and J. Kirschner, *One-step or two-step core-resonant double photoemission from a Ag(100) surface*, Frühjahrstagung der Sektion Kondensierte Materie der Deutschen Physikalischen Gesellschaft, Regensburg, Germany. 10.-15.03.2013, Poster
- G. Di Filippo, M. I. Trioni, G. Fratesi, F. O. Schumann, Z. Wei, C.-H. Li, L. Behnke, S. Patil, J. Kirschner, and G. Stefani, *The L 23 VV Auger spectrum of Cu(001)p(2,2)-S studied by Auger Photoelectron Coincidence Spectroscopy*, VUVX-2013: 38th International Conference on Vacuum Ultraviolet and X-ray Physics, Hefei, PR China. 12.-19.07.2013, Talk.
- F. O. Schumann, L. Behnke, C.-H. Li, J. Kirschner, Y. Pavlyukh, and J. Berakdar, *Electron pair emission from a highly correlated material*, 8th International Symposium on Metallic Multilayers, Kyoto, Japan. 19.-24.05.2013, Poster
- F. O. Schumann, L. Behnke, C.-H. Li, and J. Kirschner, *Electron pair emission: Insights on the electron correlation strength*, International Workshop on Strong Correlations and Angle-Resolved Photoemission Spectroscopy (CORPES 13), Hamburg, Germany. 29.07.-02.08.2013, Talk
- L. Behnke, F. O. Schumann, C.-H. Li, and J. Kirschner, *Exploring highly correlated materials via electron pair emission*, Frühjahrstagung der Sektion Kondensierte Materie der Deutschen Physikalischen Gesellschaft, Berlin, Germany. 25.-30.03.2012, Talk

- C.-H. Li, S. Patil, Z. Wei, L. Behnke, F. O. Schumann, G. Di Filippo, G. Stefani, and J. Kirschner, *Electron coincidence studies from S-overlayers on Cu(100) and Ni(100)*, Frühjahrstagung der Sektion Kondensierte Materie der Deutschen Physikalischen Gesellschaft, Berlin, Germany. 25.-30.03.2012, Talk
- L. Behnke, F. O. Schumann, and J. Kirschner, *Electron pair emission from Ag(100)*, International Conference on Many Particle Spectroscopy of Atoms, Molecules, Clusters and Surfaces (MPS 2012), Berlin, Germany. 27.08.-01.09.2012, Poster
- C.-H. Li, C. Tusche, L. Behnke, F. O. Schumann, and J. Kirschner, *Electron pair emission from surfaces upon He²⁺ impact*, International Conference on Many Particle Spectroscopy of Atoms, Molecules, Clusters and Surfaces (MPS 2012), Berlin, Germany. 27.08.-01.09.2012, Poster
- F. O. Schumann, L. Behnke, C.-H. Li, J. Kirschner, Y. Pavlyukh, and J. Berakdar, *Electron pair emission from a highly correlated material*, International Conference on Many Particle Spectroscopy of Atoms, Molecules, Clusters and Surfaces (MPS 2012), Berlin, Germany. 27.08.-01.09.2012, Poster
- F. O. Schumann, L. Behnke, C.-H. Li, J. Kirschner, Y. Pavlyukh, and J. Berakdar, *Electron pair emission from a highly correlated material*, International Workshop on Correlated Electrons at Surfaces and Interfaces, Würzburg, Germany. 01.-04.10.2012, Talk
- L. Behnke, C.-H. Li, F. O. Schumann, and J. Kirschner, *Electron pair emission from NiO(100)*, Frühjahrstagung der Sektion Kondensierte Materie der Deutschen Physikalischen Gesellschaft, Dresden, Germany. 13.-18.03.2011, Poster
- L. Behnke, C.-H. Li, F. O. Schumann, and J. Kirschner, *Electron pair emission from NiO(100)*, International Symposium on (e,2e), Double-ionization and Related Topics, Dublin, Ireland. 04.-06.08.2011, Poster
- F. O. Schumann, L. Behnke, C.-H. Li, and J. Kirschner, *The role of diffraction in (e,2e) experiments*, 28th European Conference on Surface Science (ECOSS 28), Wroclaw, Poland. 28.08.-02.09.2011, Talk

Acknowledgements

First, I like to thank Prof. Jürgen Kirschner for giving me the opportunity and support to learn more from solid state physics, especially about electron interactions, in a highly motivating and stimulating atmosphere. It is a pleasure for me to be part of the coincidence group and to work on this fascinating experimental set-up. I am grateful to discuss the results with him and to learn about science. I am also grateful for his support under special circumstances.

I thank Frank O. Schumann for his continuous guidance throughout this work and the introduction to coincidence physics. I learned a lot from his experimental experience and about scientific interpretation.

I thank my lab colleagues Chang-Hui Li, Zheng Wei, Michael Huth, Rhejenda Dhaka, Iuri Brandt and Dmitry Vasilyev. It was a pleasure to work with them becoming a good international team. I enjoyed discussing physics and learning from different cultures.

I thank Carsten Winkler for cordially helping me at the beginning of my stay and during his visits at the institute.

I thank Khalil Zakeri Lori for the wonderful discussions about physics, and among other things, football. Thanks also for reading and commenting this thesis.

I thank Aimo Winkelmann for the great discussions.

I thank Yaroslav Pavlyukh and Prof. Jamal Berakdar from MLU for the theoretical collaboration and stimulating discussions.

I thank Franz Giebels and Prof. Roland Feder from the University of Duisburg-Essen for enlightening discussions about $(e,2e)$ theory.

I thank PhD Jürgen Henk from MLU for the band structure calculation of Ag.

I thank Prof. Sergey Samarin from University of Western Australia for the fruitful discussions. Technical support from René Neumann, Herbert Engelhard, Frank Helbig and Detlef Hartung is gratefully appreciated. I thank the colleagues from the mechanical workshop in behalf of Jürgen Wille. Many thanks to the colleagues of the electronic lab Klaus Haenecke, Michael Oppelt and Detlef Proske. High quality crystals were provided by Heike Menge.

I thank the computer support group. Many thanks to the colleagues from the library Julia Ducke and Jochen Barthel. Thanks also to Frau Andrea Amm from the graphic shop. I thank the colleagues from the administration and our secretary Doreen Röder.

I thank the coordinators of the International Max Planck Research School (IMPRS) Xenia Boldyreva, Maria Santos and Arthur Ernst for their assistance during my study. Thanks to all lectures from IMPRS seminar giving me the ability to learn more about Nanophysics.

Many thanks to all colleagues from the institute from near by and around the world making the stay a fantastic experience. Special thanks to Safa Golrokh Bahoosh for her friendship, motiva-

tion and reading this thesis.

Big thanks to my “Stammtisch” friends and old school friends for their support. Many thanks to my parents and brother for their love and their interest in physics. I am grateful to my grandparents for being with me on this way, at my side and from above. Thanks to my husband for making me happy and thanks to our son, boxing my ribs, when I had a great idea.

Curriculum vitae

Name, Vorname: Behnke, Lucie
Geburtstag: 12. Februar 1984
Geburtsort: Berlin
Staatsangehörigkeit: Deutsch
Familienstand: Verheiratet
Wohnsitz: Sternstr. 13, 06108 Halle (Saale)
Email: lbehnke@mpi-halle.de

Wissenschaftlicher Werdegang

11/2009 - jetzt Doktorandin am Max-Planck-Institut
für Mikrostrukturphysik, Halle
Betreuer: Prof. Kirschner

10/2006 - 10/2009 Physikstudium an der Universität Leipzig
Vertiefungsrichtung: Halbleiterphysik bei Prof. Grundmann
Diplomarbeit: Eigenschaften von ZnO und MgZnO
MSM Photodetektoren
Abschluss: Diplom Physikerin

10/2005 - 09/2006 Physikstudium an der Universidad de Granada, Spanien

10/2003 - 09/2005 Physikstudium an der Universität Leipzig
Abschluss: Physik Vordiplom

09/1998 - 07/2003 Internatsgymnasium, Naturwissenschaftlicher Zweig,
Landesschule Pforta, Sachsen-Anhalt
Abschluss: Abitur

Halle, 26. August 2014

Lucie Behnke

Eidesstattliche Erklärung

Ich erkläre hiermit an Eides statt, gemäß §5 der Promotionsordnung der Naturwissenschaftlichen Fakultäten I, II, III und des Zentrums für Ingenieurwissenschaften der Martin-Luther-Universität Halle-Wittenberg vom 13.06.2012, dass ich die vorliegende Arbeit selbständig und ohne fremde Hilfe verfasst, sowie keine als die von mir angegebenen Quellen und Hilfsmittel benutzt und die den benutzten Werken wörtlich oder inhaltlich entnommenen Stellen als solche kenntlich gemacht habe.

Weiterhin erkläre ich, dass ich bisher keine vergeblichen Promotionsversuche unternommen habe und die Dissertation in der gegenwärtigen bzw.in einer anderen Fassung an keiner einer anderen Fakultät vorgelegen habe.

Halle, 26. August 2014

Lucie Behnke